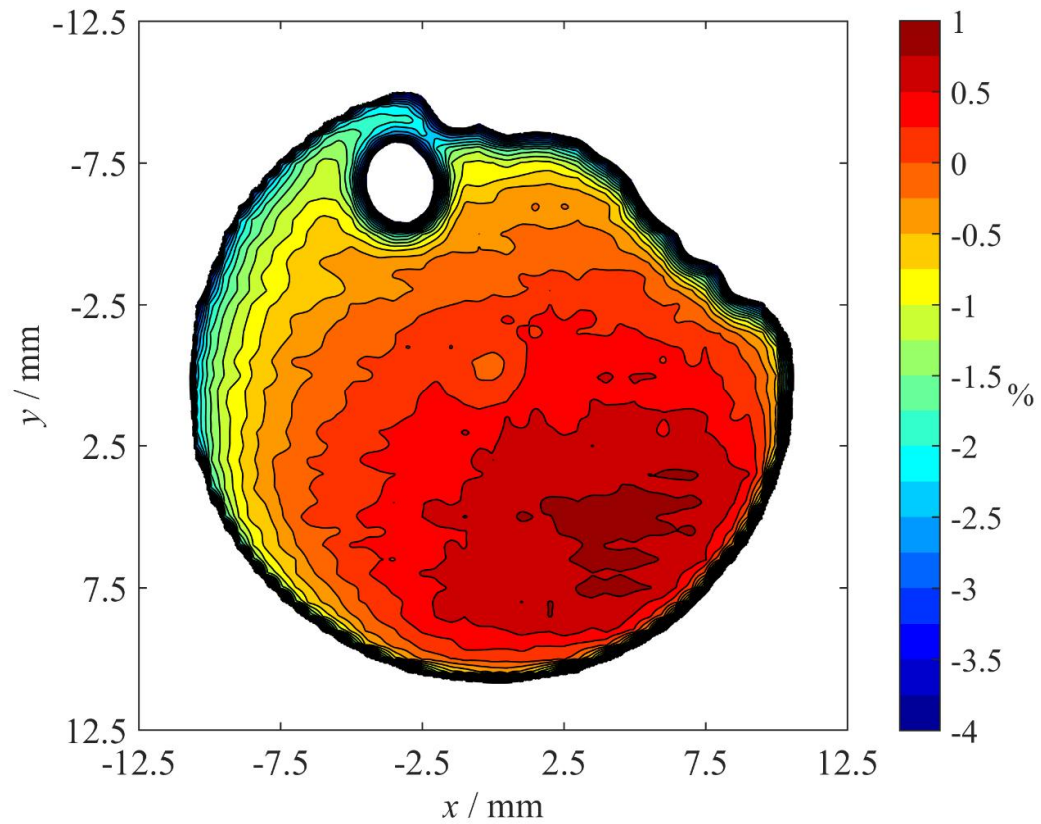

UV NEWS

The official newsletter of the Thematic Network for Ultraviolet Measurements



Issue 11 / March 2016

Contents

Editorial	3
EMRP ENV59 Traceability for atmospheric total column ozone	4
Characterisation of Dobson spectrophotometers at PTB	4
Analysis of Brewer instrumental temperature dependence	8
Out-of-range stray light characterization of single-monochromator Brewer spectrophotometer	20
A UV/Vis solar spectroradiometer for the remote sensing of the Atmosphere (PSR-ATMOZ)	24
UV-LED based source for tracking radiometric stability of array spectroradiometers	27
Adaptation of a Fourier Transform Spectroradiometer for outdoor measurements of the direct solar spectral irradiance	30
Improvements in DOAS-derived total ozone from Phaethon	32
A simulation-tool to model ozone retrieval uncertainties of Brewer and Dobsons instruments	36
A birefringence-based wavelength ruler for on-site wavelength scale calibration of spectroradiometers in the UV	42
Regular articles	46
Application of stray light corrected array spectroradiometers for UV measurements	46
News	49
UV Index and UV-B solar recorded measurements at Valladolid University, Spain	49
The LED-J1019 Transfer standard	50

ISSN 1456-2537

Unigrafia, Espoo 2016

UVNews is the official newsletter of the Thematic Network for Ultraviolet Measurements. The Network was originally funded by the Standards, Measurements and Testing programme of the Commission of the European Communities, as project number SMT4-CT97-7510. During 2014 – 2017, the Network receives financing from the Euramet through project EMRP ENV59 “Traceability for atmospheric total column ozone.” *UVNews* is published at irregular intervals. It is aimed to exchange knowledge between the participants of the Network and to disseminate information on the forthcoming and past activities of the Network. The newsletter also contains scientific and technical articles on UV measurements and a news-section about activities in the field of UV measurements. The newsletter welcomes all announcements and articles that might be of importance for the readers. The editor of the Newsletter may be reached by:

Aalto University
Metrology Research Institute
Petri Kärhä
P. O. Box 13000
FI-00076 Aalto, Finland
<http://metrology.hut.fi/uvnet/>
E-mail: petri.karha@aalto.fi

In case of all material to publish, submission by E-mail is preferred. The next issue will be published in March 2017.

Photographs: Cover: Spatial uniformity (Picture by A. Vaskuri). Page 3: Participants of the ATMOZ kick-off meeting (Photo by PMOD/WRC).

Editorial

Petri Kärhä

Aalto University, Espoo, Finland

The last *UVNews* reported on the final outcome of the EMRP project ENV03 “Traceability for surface spectral solar ultraviolet radiation.” Since then we have started a continuation project ENV59 ATMOZ “Traceability for atmospheric total column ozone” which among other activities funds the Thematic Network for Ultraviolet Measurement for three years to publish two issues of *UVNews*. Further information on the ATMOZ project can be found in <http://projects.pmodwrc.ch/atmoz/>

The ATMOZ project is now at its mid-point. This *UVNews* thus reports progress of the activities so far. The project addresses and improves various methods to derive stratospheric ozone such as Brewer spectroradiometers, Dobson-instruments and multispectral measurements. New techniques for calibration and characterization of the measurements are being developed and uncertainties are estimated.

The techniques developed will be demonstrated in various activities during the second half of the project, starting at the Brewer Ozone Spectrophotometer/Metrology Open Workshop in Ponta Delgada, Azores, on May 17 to 20, 2016. A Total Ozone Measurements Intercomparison will be arranged at Izaña, Tenerife, on September 12 – 30, 2016.

UVNews 12 will be published around March 2017. The project EMRP ENV59 ATMOZ will then be almost complete, and the final outcome of the project will be reviewed. This newsletter will be collected early 2017. To receive the call for articles, please register to the *UVNet* mailing list (<http://metrology.tkk.fi/uvnet/lists.htm>) if you do not receive our E-mails already. The same page can be used to unsubscribe from the mailing list.

Finally, I would like to wish you all a nice spring and summer, and hope to see you in the coming UV activities!



EMRP ENV59 Traceability for atmospheric total column ozone

Characterisation of Dobson spectrophotometers at PTB

Saulius Nevas¹, Ulf Köhler², Fritz Schönenborn², Glen McConville³, and R. Evans³

1. Physikalisch-Technische Bundesanstalt (PTB), Braunschweig, Germany

2. Deutsche Wetterdienst (DWD), Hohenpeißenberg, Germany

3. NOAA ESRL, Boulder, USA

Introduction

The first measurements of the total column ozone (TOC) were started in the 1920s with the development of the Dobson spectrophotometer and a respective algorithm. A global network for ground-based TOC observations based on the Dobson instruments has been established and is in operation since decades. The algorithm used to derive the TOC from the measurement data requires the bandwidths and the centre wavelengths of the bandpass functions of the Dobson spectrophotometers. These parameters, though, are not known for each instrument but are assumed to be equal to those of the world reference Dobson [1]. The consistency among the instruments is maintained based on well-defined assembly and operating procedures as well as on side-to-side field comparisons against the reference instruments arranged on a regular basis. Results of the TOC measurements using the Dobson and the Brewer instruments, which were introduced in the early 1980s as the second instrument type for the TOC observation, have shown discrepancies, which have been partly traced back to uncharacterised instrumental features. Hence, a direct optical characterisation of the bandpass functions of the instruments shall help to understand the discrepancies and offer a metrological basis for the TOC measurements.

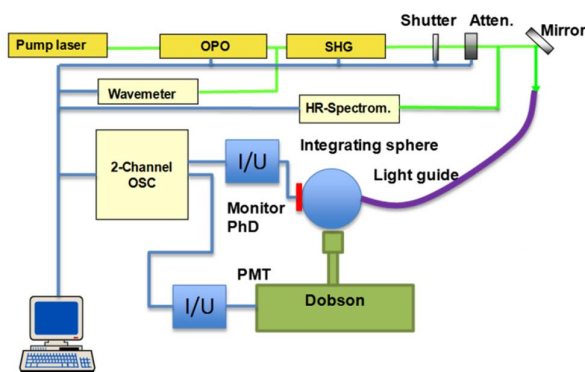


Figure 1. Schematic representation of bandpass function and wavelength measurements of Dobson spectrophotometers at the PLACOS setup of PTB.

The first direct optical characterisation of the world reference Dobson instrument Nr. 083, operated by NOAA/ESRL in Boulder, USA, was done using a setup based on a lamp and a double monochromator [2]. The same Dobson spectrophotometer was later also characterised using a procedure, where the PMT detector of the instrument was replaced by the entrance optics of a compact array spectroradiometer, and the transmission

function of the instrument was recorded under the solar irradiation [3]. In both cases, bandpass functions different from the nominal ones were observed. The European regional reference Dobson Nr. 064, operated by DWD in Hohenpeißenberg, Germany, had not been characterised by such methods so far at all. Within the project EMRP ENV59 “Traceability for the total column ozone” both the world reference Dobson Nr. 083 and the European reference Dobson Nr. 064 were characterised in 2015 at PTB in Braunschweig. The applied procedures and the obtained results are summarised in this report.

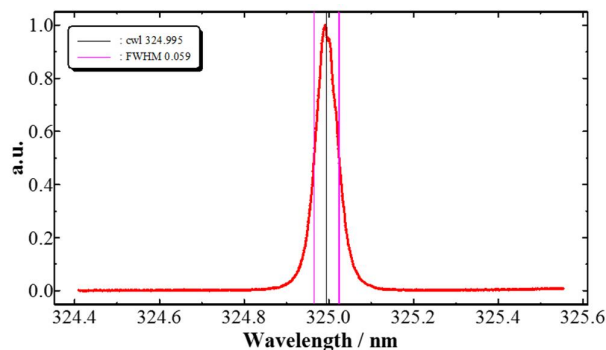


Figure 2. Spectral power distribution of the laser radiation provided by the PLACOS setup at 325 nm wavelength.

Measurement procedures

The bandpass and wavelength characterization of the Dobson instruments was carried out at the PLACOS setup of PTB providing a narrowband spectrally tuneable radiation [4]. The measurement scheme is shown in Figure 1. The OPO system operates at 20 Hz repetition rate, 6-7 ns pulse duration, and spectral bandpass of 5 cm^{-1} . Figure 2 shows exemplary the spectral power distribution of the OPO system output at 325 nm wavelength. The data were obtained by an Echelle spectrograph. The OPO wavelengths during the bandpass measurements were monitored by a wavemeter and a high resolution Avantes spectrometer with a FWHM of 0.1 nm.

The wavelength scale of the spectrometer was calibrated with a standard uncertainty of 0.01 nm against atomic emission lines. The output radiation was coupled via a liquid light guide into a 5 cm diameter integrating sphere. One output port of the sphere was irradiating the entrance diffusers of the Dobson instruments. The anode current of the Dobson PMT detector was fed via a current-to-voltage converter into a channel of a fast-sampling oscilloscope. Another oscilloscope channel was used to measure the signal of a monitor photodiode attached to another port of

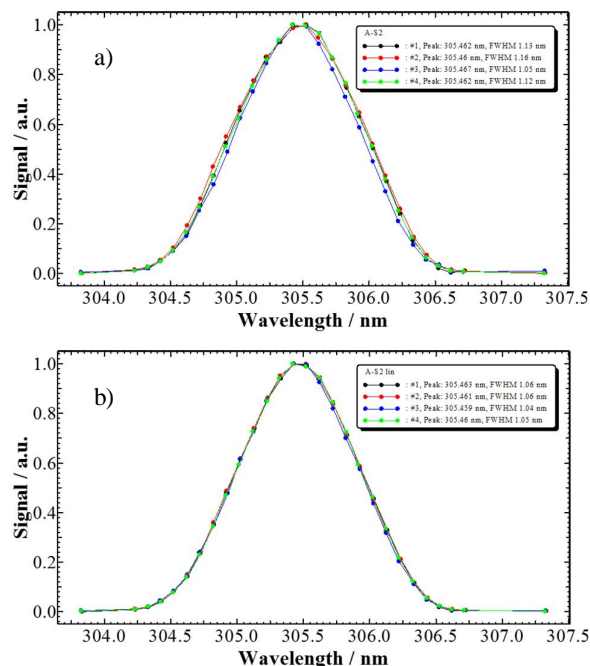


Figure 5. Bandpass functions for slit A-S2 of Dobson No. 083 measured at different PMT voltages and laser power levels a) without nonlinearity corrections, b) after nonlinearity corrections.

Results

Figures 6 to 11 (next page) show the bandpass functions measured for the DWD Dobson No. 64 and the NOAA/ESRL Dobson No. 83. In addition, the figures show also data for the Dobson No. 83 published in [2] and the tabulated nominal values [1]. Table 3 summarizes respective parameters for the measured bandpass functions.

Table 3. Parameters of bandpass functions for the European regional reference Dobson No. 064 and the world reference Dobson No. 083 measured in 2015 at PTB in Braunschweig.

Slit	Dobson No. 064 (DWD)		Dobson No. 083 (NOAA/ESRL)	
	Peak (nm)	FWHM (nm)	Peak (nm)	FWHM (nm)
A-S2 (305.5)	305.51	1.03	305.46	1.05
C-S2 (311.5)	311.50	1.08	311.47	1.09
D-S2 (317.5)	317.62	1.27	317.58	1.24
A-S3 (325.0)	325.08	3.56	325.10	3.56
C-S3 (332.4)	332.44	3.81	332.47	3.81
D-S3 (339.9)	339.97	4.06	334.00	4.12

Conclusions and outlook

Both the world reference Dobson spectrophotometer No. 083 and the European reference Dobson instrument No. 064 were characterized for their bandpass functions and centre wavelengths at PTB in Braunschweig. The two reference instruments showed very similar characteristics. The bandpass functions of the Dobson spectrophotometers, though, do have quite different shapes as compared to the nominal tabulated ones [1]. The results of the characterizations confirm also a good agreement and

Table 1. Parameters of the bandpass function (A-S2) of Dobson No. 083 measured at different PMT voltages and laser power levels proportional to monitor detector signal (MON) without and after the nonlinearity corrections. The signal values (Sig) indicate peak values at the peak wavelength of the bandpass function.

Without nonlinearity correction					
Measurement #	Peak (nm)	FWHM (nm)	PMT (V)	Sig (V)	Mon (V)
1	305.462	1.13	182	0.50	1.07
2	305.460	1.16	209	1.04	0.98
3	305.467	1.05	166	0.22	0.86
4	305.462	1.12	166	0.47	2.02
After nonlinearity correction					
Measurement #	Peak (nm)	FWHM (nm)	PMT (V)	Sig (V)	Mon (V)
1	305.463	1.06	182	0.50	1.07
2	305.461	1.06	209	1.04	0.98
3	305.459	1.04	166	0.22	0.86
4	305.460	1.05	166	0.47	2.02

consistency observed between the two instruments in the regular TOC measurement comparisons.

A radiometric characterization of several other Dobson network instruments is planned in the next stage of the EMRP project. Also a reference Brewer instrument from the European Brewer Reference Centre (RBCC-E) was characterized in January 2016 at PTB in Braunschweig. The analysis of the obtained data and its effect on the TOC derivation algorithm is in progress.

Acknowledgement This work has been supported by the European Metrology Research Programme (EMRP) within the joint research project EMRP ENV59 “Traceability for atmospheric total column ozone.” The EMRP is jointly funded by the EMRP participating countries within EURAMET and the European Union.

References

- G.M.B. Dobson, “Observer’s handbook for the ozone spectrophotometers,” *Ann. IGY* **5**, 90–114, Pergamon (1957).
- W. D. Komhyr, C. L. Mateer, and R.D. Hudson, “Effective Bass-Paur 1985 Ozone absorption coefficients for use with Dobson ozone spectrophotometer,” *J. Geophys. Res.* **98**, 20451–20465 (1993).
- R. Evans, G. Mcconville, S. Oltmans, I. Petropavlovskikh, D. Quincy, and G. Labow, “Determination of Dobson instrument spectral characteristics, a new method,” in *Proc. Quadrennial Ozone Symposium (QOS)*, Toronto, Canada, 27–31 August 2012.
- S. Nevas, M. Lindemann, A. Sperling, A. Teuber, and R. Maass, “Colorimetry of LEDs with array spectroradiometers,” *MAPAN—J. Metrol. Soc. India* **24**, 153–162 (2009).

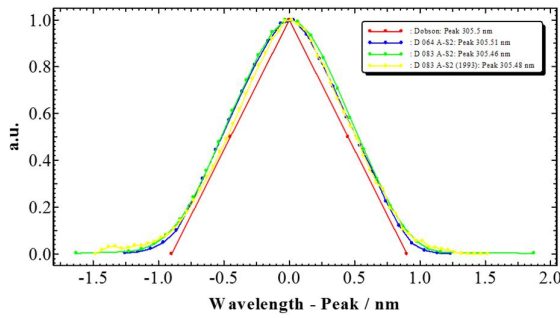


Figure 6. Bandpass functions for slit A-S2: nominal values (red curve), measured at PTB for Dobson No. 064 (blue curve) and Dobson No. 083 (green curve) as well as the data for Dobson No. 083 published in [2] (yellow curve).

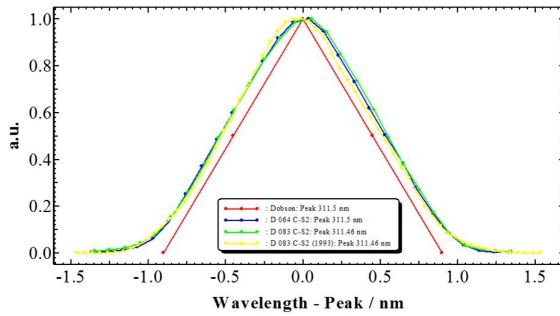


Figure 7. Bandpass functions for slit C-S2: nominal values (red curve), measured at PTB for Dobson No. 064 (blue curve) and Dobson No. 083 (green curve) as well as the data for Dobson No. 083 published in [2] (yellow curve).

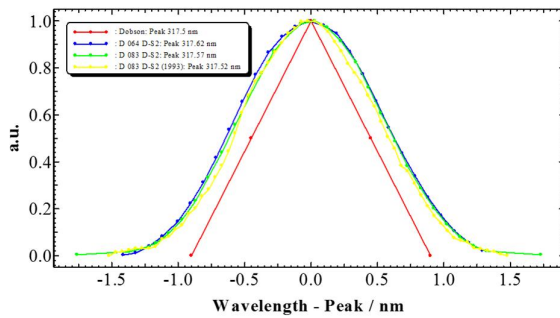


Figure 8. Bandpass functions for slit D-S2: nominal values (red curve), measured at PTB for Dobson No. 064 (blue curve) and Dobson No. 083 (green curve) as well as the data for Dobson No. 083 published in [2] (yellow curve).

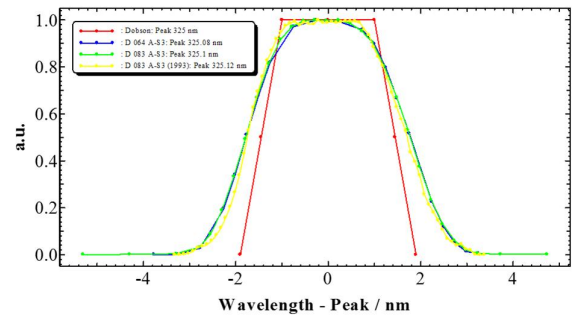


Figure 9. Bandpass functions for slit A-S3: nominal values (red curve), measured at PTB for Dobson No. 064 (blue curve) and Dobson No. 083 (green curve) as well as the data for Dobson No. 083 published in [2] (yellow curve).

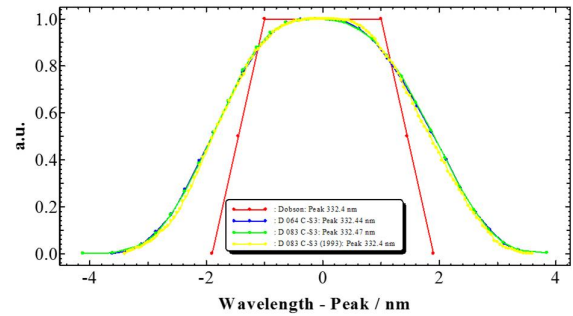


Figure 10. Bandpass functions for slit C-S3: nominal values (red curve), measured at PTB for Dobson No. 064 (blue curve) and Dobson No. 083 (green curve) as well as the data for Dobson No. 083 published in [2] (yellow curve).

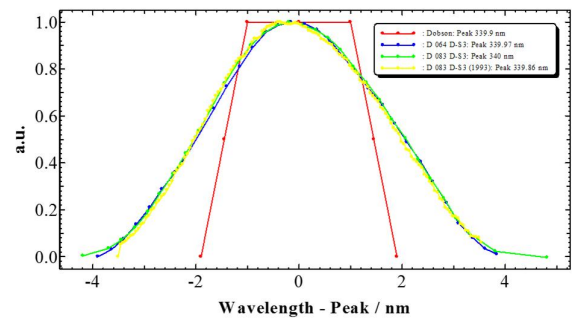


Figure 11. Bandpass functions for slit D-S3: nominal values (red curve), measured at PTB for Dobson No. 064 (blue curve) and Dobson No. 083 (green curve) as well as the data for Dobson No. 083 published in [2] (yellow curve).

Analysis of Brewer instrumental temperature dependence

Alberto Redondas¹, Alberto Berjón², Meelis-Mait Sildoja³, Saulius Nevas³, and Manuel Rodríguez²

1. Izaña Atmospheric Research Center, AEMET, Tenerife, Canary Islands, Spain

2. University of La Laguna, Tenerife, Canary Islands, Spain

3. Physikalisch-Technische Bundesanstalt, 38116, Braunschweig, Germany

INTRODUCTION

The Dobson [1] and the Brewer [2] spectrophotometers are the primary ground-based instruments used to report total column ozone (TOC) which is obtained from the differential absorption of select wavelengths in the UVB portion of the spectrum.

Ozone measurements from Dobson and Brewer instruments network have shown systematic discrepancies of up to 3% [3], which is significantly larger than can be achieved within Brewer and Dobson instruments. These discrepancies have been partly traced back to uncharacterized instrumental features, and Brewer temperature dependence has been established as one of the features that require further study.

In this letter, we present preliminary results of the temperature dependence characterization of RBCC-E Brewer spectrometer #185, performed from 23 to 26 of January, using a dedicated climate chamber at Physikalisch-Technische Bundesanstalt (PTB), Braunschweig.

Data and Method

1. Brewer Instrument

A comprehensive description of the instrument can be found at [4], but essentially it contains a modified Ebert monochromator (single or double monochromator, depending on models) with six exit slits graved in a cylindrical mask, positioned by a stepper motor, which exposes only one wavelength slit at a time. A UV sensitive photomultiplier tube operating in photon counting mode is used as detector. A prism in the foreoptics is rotated to select light from either global port, direct sun, or one of the two calibration lamps (a mercury lamp and a quartz-halogen lamp). Other elements in the foreoptics assembly are the iris diaphragm and two filter wheels, with neutral density filters and polarizers.

In the standard operating mode (ozone mode), the Brewer measures the desired wavelengths (306.3 nm, 310.1 nm, 313.5 nm, 316.8 nm and 320.1 nm) by selecting different slits on the mask, while the monochromator remains in the same position. In addition, the Brewer instrument can operate in other two different modes. A mode to obtain spectral intensity scan of UV radiation in the 286.5 nm to 363 nm range by rotation of the monochromator grating and fixing the slit mask (UV mode), and a combined mode where specific wavelengths in the whole range (311.0, 314.0, 317.6, 321.0, 324.2, 325.6, 327.3, 328.5, 332.0, 335.2, 338.2, 339.3, 341.1, 342.0, 345.3, 348.4, 348.9, 351.2, 354.0, 351.5, 354.7, 357.7, 360.4, and 363.1 nm) are selected by moving both the grating and the slit mask (Aerosol optical depth (AOD) mode).

Equation 1 is used to calculate TOC from the Brewer measurements [3],

$$TOC = \frac{N-B-ETC}{A\mu} \quad (1)$$

$$N = \sum_{i=1}^n w_i \log(I_i) \quad (2)$$

where A is the ozone absorption coefficient or differential cross section, μ is the ozone air mass, B is the Rayleigh molecular scattering, ETC is the extraterrestrial calibration constant, and N , also known as $R6$, is a linear combination of the logarithm of the measured spectral direct irradiances at ground level (I_i) at the selected wavelengths (Equation 2). The irradiances are corrected for the detector dead time, dark current and temperature dependence.

The Brewer instrument is not temperature stabilized, but it is equipped with a heater which is automatically switched on when the instrument temperature drops below 10°C or 20°C depending on the configuration. Data from EUBREWNET database, the European Network of Brewer Spectrophotometer (www.eubrewnet.org), shows that typical Brewer operating temperatures stay between -5 °C and 50 °C (Figure 1).

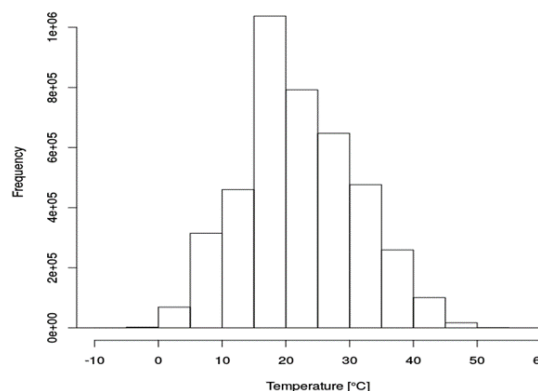


Figure 1. Frequency distribution of instrument temperature obtained from EUBREWNET database. A total of 4,177,306 Direct Sun measurements of 70 Brewer instruments have been analyzed.

2. Brewer temperature dependence

Since the properties of the instrument change with time, the internal halogen lamp is used to track these changes. The long-term variation is associated to the extraterrestrial calibration constant of the instrument [5]. An additionally short-term variation associated with the temperature is generally observed in the internal halogen lamp measurements. The instrument's sensitivity to the temperature is calculated as the negative slope of the linear correlation between the logarithm of the measurements to

the internal halogen lamp and the instrument temperatures for each wavelength in ozone mode. The coefficients thus determined, C_t , are then used to correct the ozone measurements (Equation 3).

$$\log(I_i) = \log(I'_i) + T * C_t C_t \quad (3)$$

To make a correct determination of the temperature dependence of the instrument, it is necessary to select the measurements within a period of time in which the lamp emission and the instrument remains stable, but also offers the widest possible temperature range. The coefficients obtained are verified by calculating the N (or $R6$) parameter (Equation 2) for the measurements of internal halogen lamp which should not present temperature dependence after applying the correction.

3. Climate chamber

The reference RBCC-E Brewer spectrometer was characterized for the temperature dependencies in a temperature controlled environment at PTB, Braunschweig. A dedicated climate chamber was used to provide necessary conditions. The schematic of the measurement system is described in Figure 2. The temperature and humidity of the chamber was monitored using the built-in sensors of the chamber and also with user inserted sensors (one PT-100 thermometer and one Almemo humidity and temperature sensor).

A Hamamatsu model LC8 UV source with a built-in Xe lamp and equipped with a quartz fiber bundle as a light guide was used to illuminate simultaneously both global and direct input ports of the Brewer. The light guide was terminated with a light-shaping-diffuser (LSD) to provide uniform illumination. To monitor the output stability of the UV source, a set of monitor detectors were placed close to the Brewer input ports. Those included two SiC photodiodes and a calibrated spectroradiometer. One of the SiC photodiodes was located inside the chamber and the other one outside. To direct the UV-radiation onto the external SiC diode a similar light guide was used as for the Xe lamp system. For optimal irradiation conditions the internal SiC photodiode and the entrance optics of the spectroradiometer included special quartz based diffusers (Primusil). For the external SiC photodiode no diffuser was used to compare the readings with the diffuser-covered detectors and register any possible change of the diffuser transmittance due to the change of temperature or relative humidity in the chamber during the experiment.

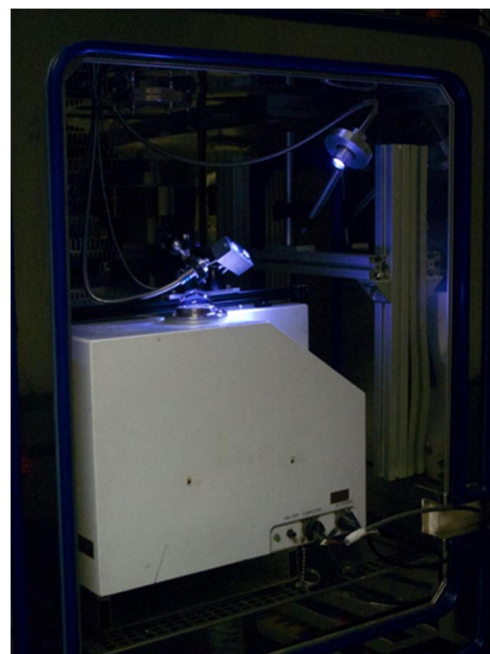
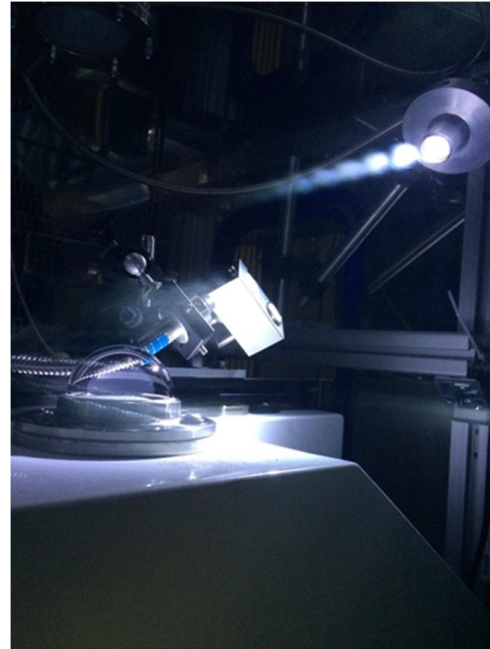
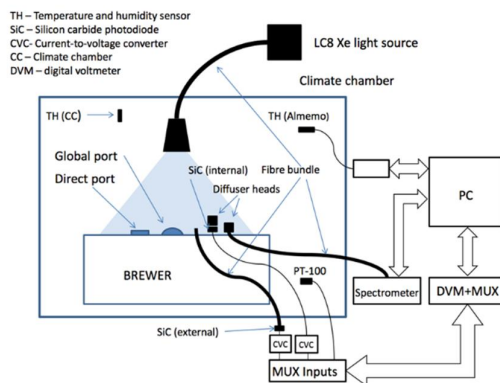


Figure 2. Measurement setup for Brewer characterization at controlled environment.



The spectral irradiance of the UV source system as measured by the spectroradiometer is shown in Figure 3.

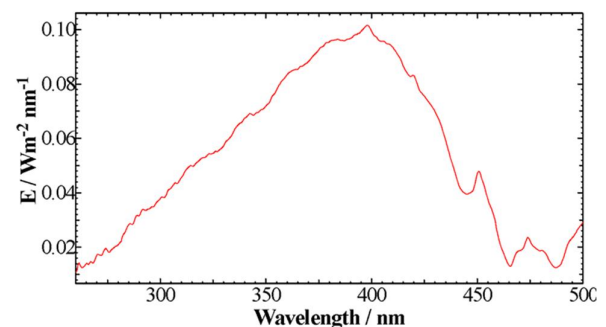


Figure 3. Spectral irradiance of the UV source as measured by the spectroradiometer.

Thematic Network for Ultraviolet Measurements

The temperature of the climate chamber was varied between -5 °C to +40 °C over a ~70 h period. Separate cycles were used at above and below 0 °C to achieve better control over temperature and humidity. Figure 4 shows the ramp signals of the temperature.

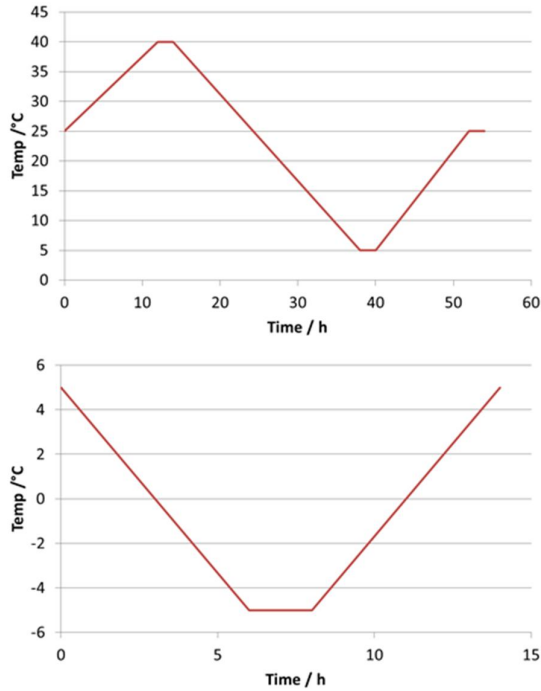


Figure 4. Temperature ramp signal of the climate chamber.

4. Description of Brewer measurements

The temperature inside the Brewer is measured in three different positions: the PMT, the base of monochromator and the fan. The internal heater has been switched off to allow operation down to 10 °C during the measurements in the chamber. In Figure 5.a we can see both the temperatures measured inside the Brewer and the chamber temperature. The average difference between the temperatures inside the brewer is 0.7 °C, and the difference between the chamber temperatures is 0.3 °C. The average difference between the temperature inside the Brewer and the chamber is 5°C. This difference is mainly due to the heat generated by the electronics and internal lamps.

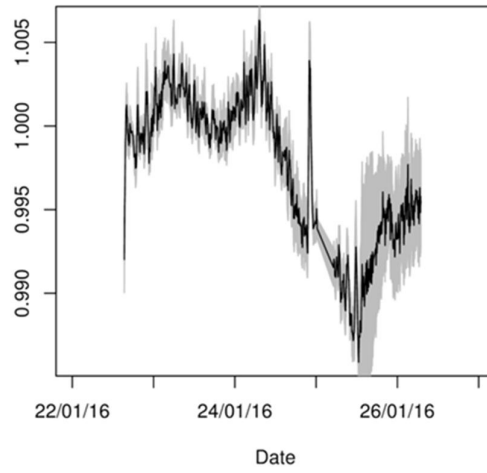
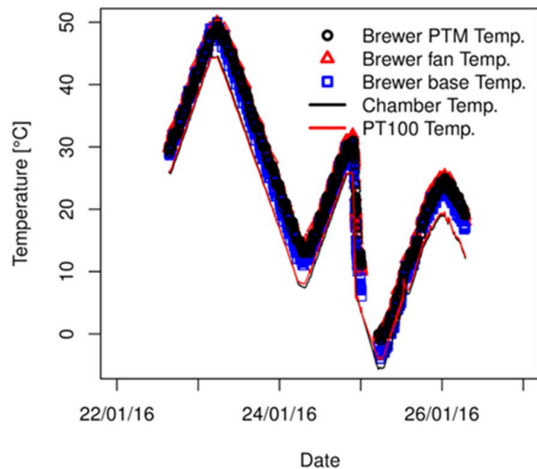


Figure 5. (a) Brewer and chamber temperatures. (b) Xe lamp normalized intensity.

The intensity of the Xe light source is calculated as a mean of the normalised integrated spectral data from the monitor spectroradiometer, and the temperature corrected SiC detector readings. Figure 5.b shows the normalized intensity and its standard uncertainty against time.

Table 1. Brewer routine and duration in minutes for each measurement type.

Measure	Mode	Input Port	Duration (min)	Cycles	Filter1	Filter2
SL	ozone	Internal Lamp	10	20	256	0
JL	aod	Internal Lamp	20	10	256	0/64
VL	uv	Internal Lamp	15	4	256	0
UQ	ozone	Global Port	5	50	128	0
JU	aod	Global Port	15	10	128	0
UX	uv	Global Port	10	1	128	0
ZD	ozone	Direct Port	5	20	256	0/64
ZJ	aod	Direct Port	15	10	256	0/64
ZU	uv	Direct Port	10	1	256	64

Different types of measurements were performed throughout the duration of the experiment, measuring through the two input port and the internal halogen lamp in three different operational modes: ozone, aod and uv. Table 1 shows the main parameters for each type of measurement. The total time to complete all measurements along with the alignment test was about 2 hours.

Figure 6 shows $\log(I_i)$ before temperature correction for the different operating modes and the different input ports, for those wavelengths closer to 310nm in each case (310.1nm for ozone mode, 310.0 for the uv mode and 311.0 for aod mode). Measurements to external lamp are corrected using the monitor measurements to take account of changes in the lamp. As expected, the measurements made through the same port have similar behavior. However there are major differences between measurements obtained through different ports. The measurements made using the internal lamp show some discontinuities, suggesting an unstable behavior of the lamp.

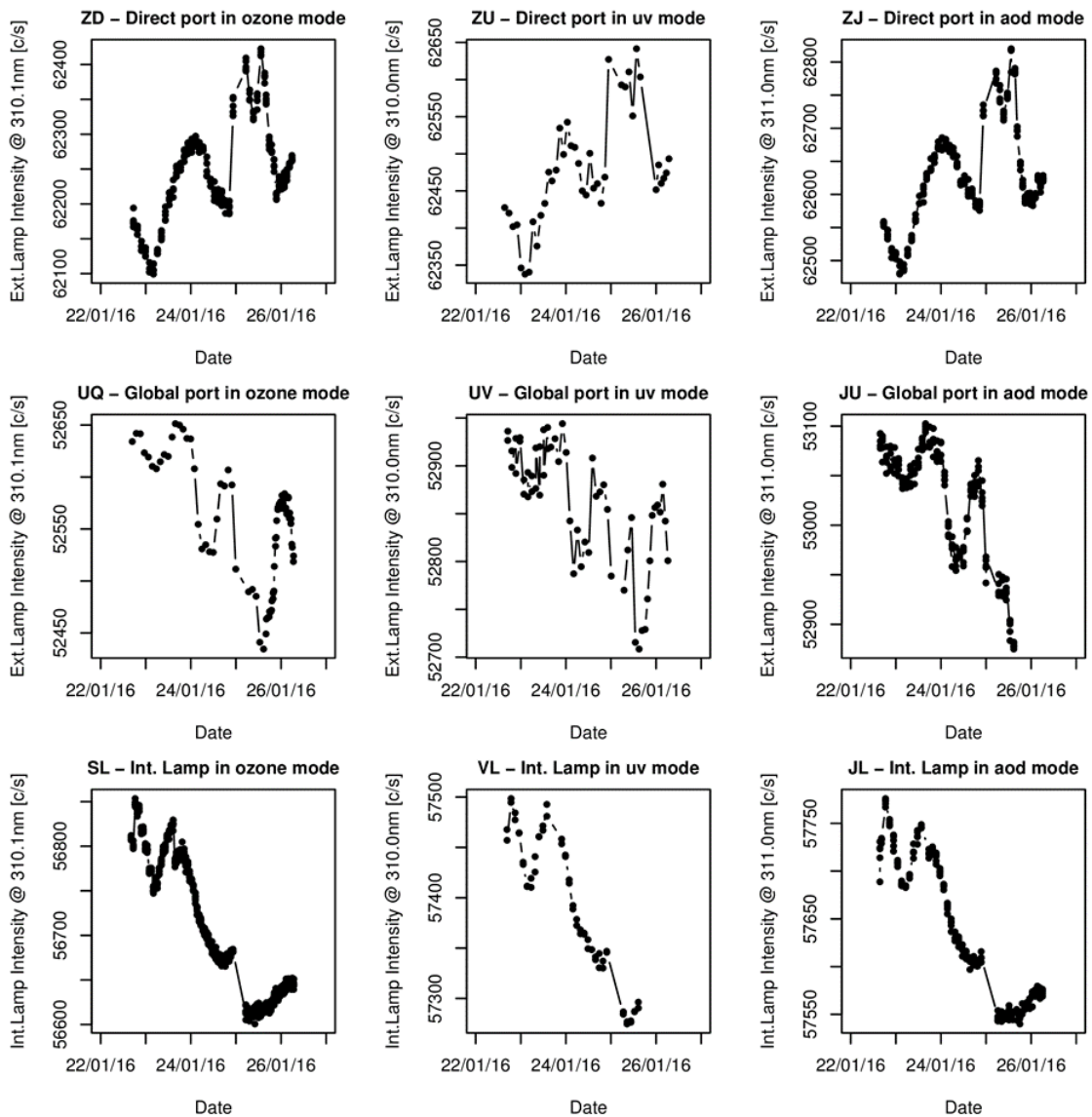


Figure 6. Brewer measurements before temperature correction for the different operating modes and the different input ports.

Correlation between Brewer measurements, $\log(I_i)$, and temperature, Figure 7, also give different results depending on the input port. The measurements made through the direct port have a negative correlation with temperature,

which becomes positive in the case of the global port and internal lamp. The Coefficient of determination is higher in the case of the measurements made through the direct port, around 0.7, than in the rest of measurements. It is worth noting the hysteresis when using the direct port.

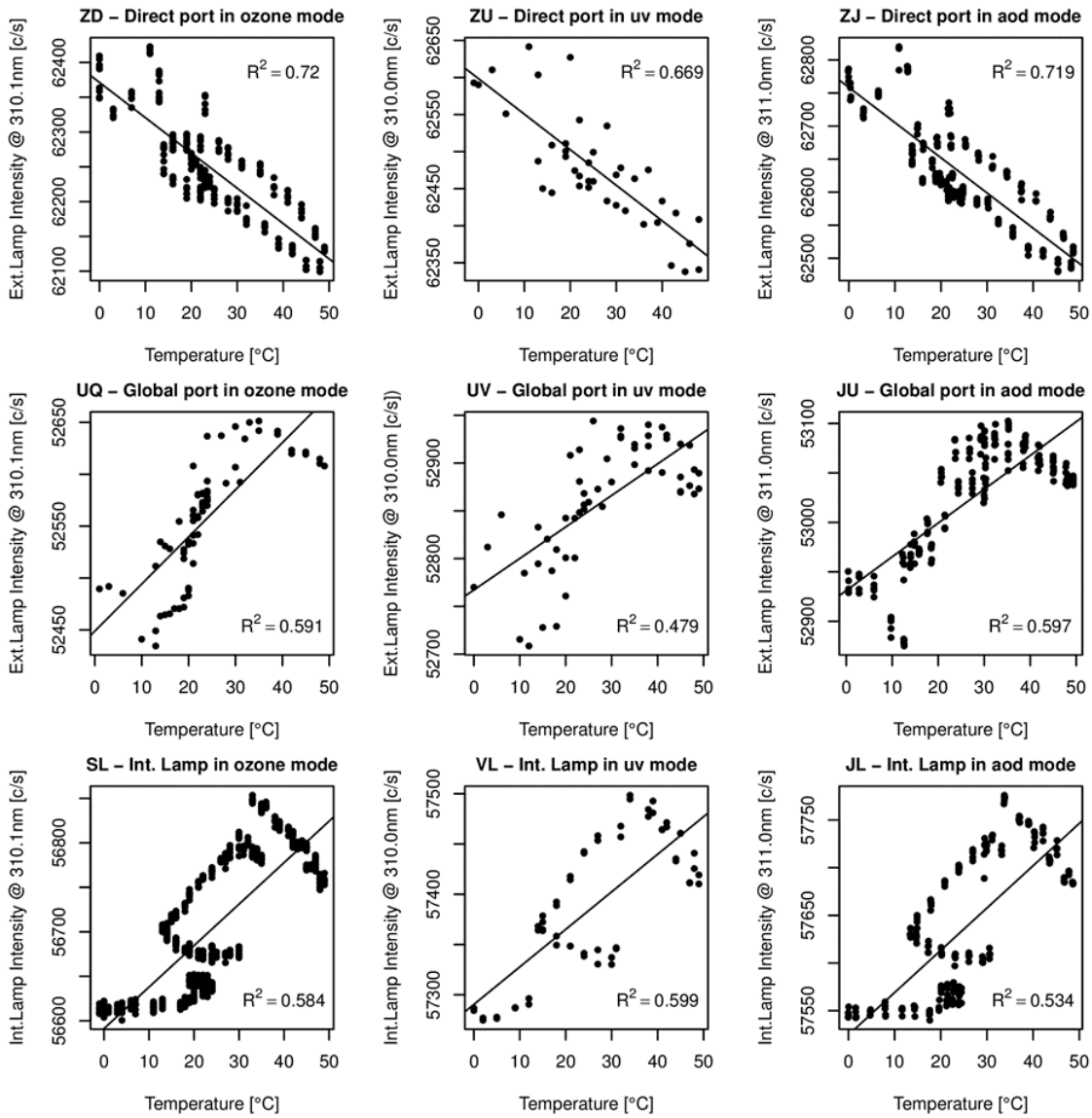


Figure 7. Correlation between Brewer measurements and temperature.

Figure 8 shows parameter R_6 (Equation 2) calculated for measurements in ozone mode. We can see again a different

behavior depending on the used port, but in the case of SL measures this behavior is nonlinear, increasing R_6 value noticeably above 40 degrees.

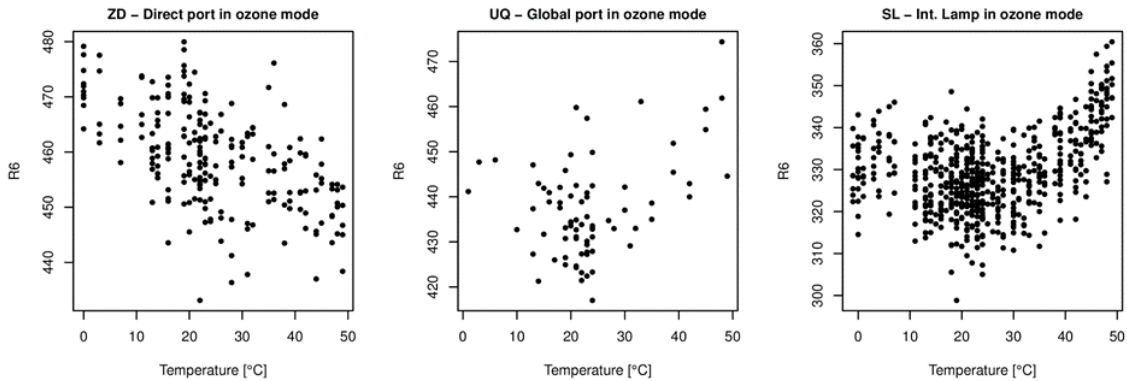


Figure 8. R_6 parameter for measurements in ozone mode.

5. Brewer internal lamp, ozone measurement

The temperature dependence is usually determined by the measurements of the internal halogen lamp. This lamp is

measured every two hours and its readings are used to track the spectral response of the instrument. The so-called “Standard Lamp Test” is an ozone observation using the

internal lamp as a source. During the calibration a reference value of the test is provided together with the ETC, and then ozone observations are corrected by the measurements of the lamp, assuming that the lamp is stable and changes detected are due to changes in the responsivity of the instrument. This assumption is confirmed in a subsequent calibration of the instrument.

In this section, we analyze the internal lamp measurements of the chamber and the field observations of the 2015 record (Figure 9). During the field observations, the temperature ranges from 17 to 38 degrees with 60% of the observations in the 19 °C range whereas the chamber measurements ranged from 0 to 50 °C. During the Chamber experiment, the internal temperature heating was switched-off.

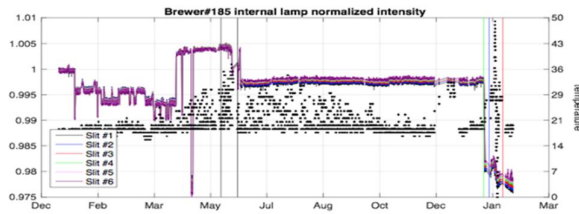


Figure 9. Normalized intensity of the Standard Lamp (SL) of the Brewer #185. The vertical lines denote the RBCC-E campaign in Huelva, and the lamp replacement before the Chamber experiment.

Figure 9 shows the normalized count for the six operational slits, with evident intensity changes which are even more evident when plotted against temperature (figure 10). The measurements on the chamber show also this intensity changes not related with temperature. This is usually fixed correcting the measurements by a polynomial fit with time (Figure 11).

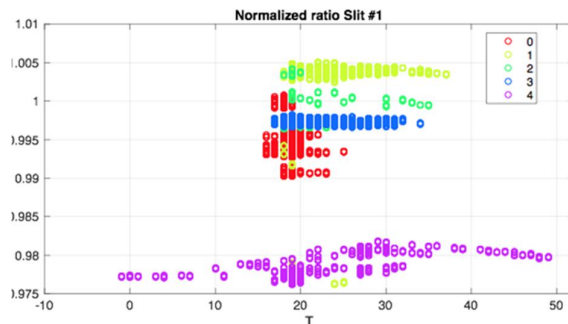


Figure 10. SL intensity normalized for Slit #1 vs Temperature, the colors indicate different time

periods, see text. We select period 1 (before the Huelva campaign and after maintenance) to determine the temperature dependence. The last period (which corresponds to the chamber experiment) looks not suitable to determine the temperature coefficients.

For the analysis we chose four periods, April-June which includes the Huelva campaign in June with temperatures up to 38°C, the period April-May which ranges up to 30, the June-December period with excellent stability of the lamp and finally the Chamber experiment. These periods are labeled as 1 to 4 in Figure 10.

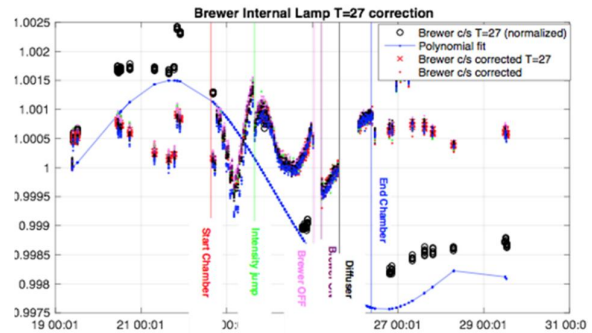


Figure 11. SL counts/second (c/s) normalized to the first measurement, the measurements for $T=27\pm 1C$ (black circles), are used to fit a 5 degree polynomial of time (blue) used to correct the time dependence. This polynomial reduces the change from 0.4% to better than 0.2% (red crosses). The normalized and corrected counts/second are represented by dots.

The temperature dependence of the Brewer#185 is very small. Indeed, currently the temperature coefficients are set to zero, so no temperature correction is performed (Table 2). This is confirmed in the usual temperature operative range, 18-35 °C.

The temperature coefficients are calculated using the method described above, using a linear regression of the counts/second against temperature. Figure 12 shows the ozone ratio for two of the periods in study, both vs time and vs temperature, with no temperature correction and with the correction derived from the coefficients. The improvement resulting from the application of the calculated coefficients is very small for the usual range and only noticeable for high temperatures greater than 35 °C and low temperatures lower than 10 °C.

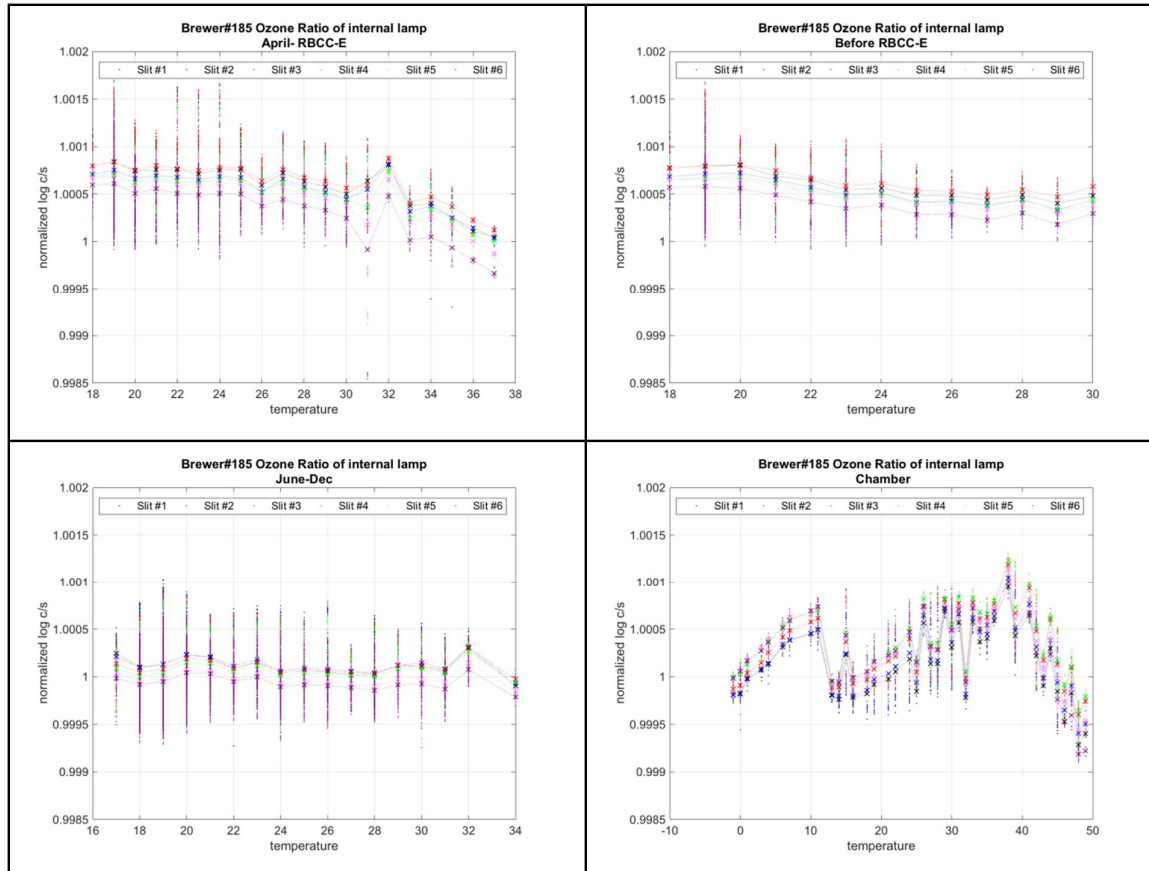


Figure 12. Temperature dependence of the internal lamp (counts/second normalized to the first measurement) for the four periods. The six slits are represented and grouped by temperature, the mean value is represented by crosses. The temperature dependence is small and only evident for temperatures outside of the normal operative temperatures within 18-30 °C.

As in the ozone measurement, with the measurements of the internal lamp we are not sure if the observed changes, in this case the temperature dependence, are due to a real change on the responsivity of the instrument or changes of the lamp system. The lamp and the power supply are inside the instrument and could be affected by changes on the temperature. The measurement of the external Xe lamp analyzed on next section will help to this analysis.

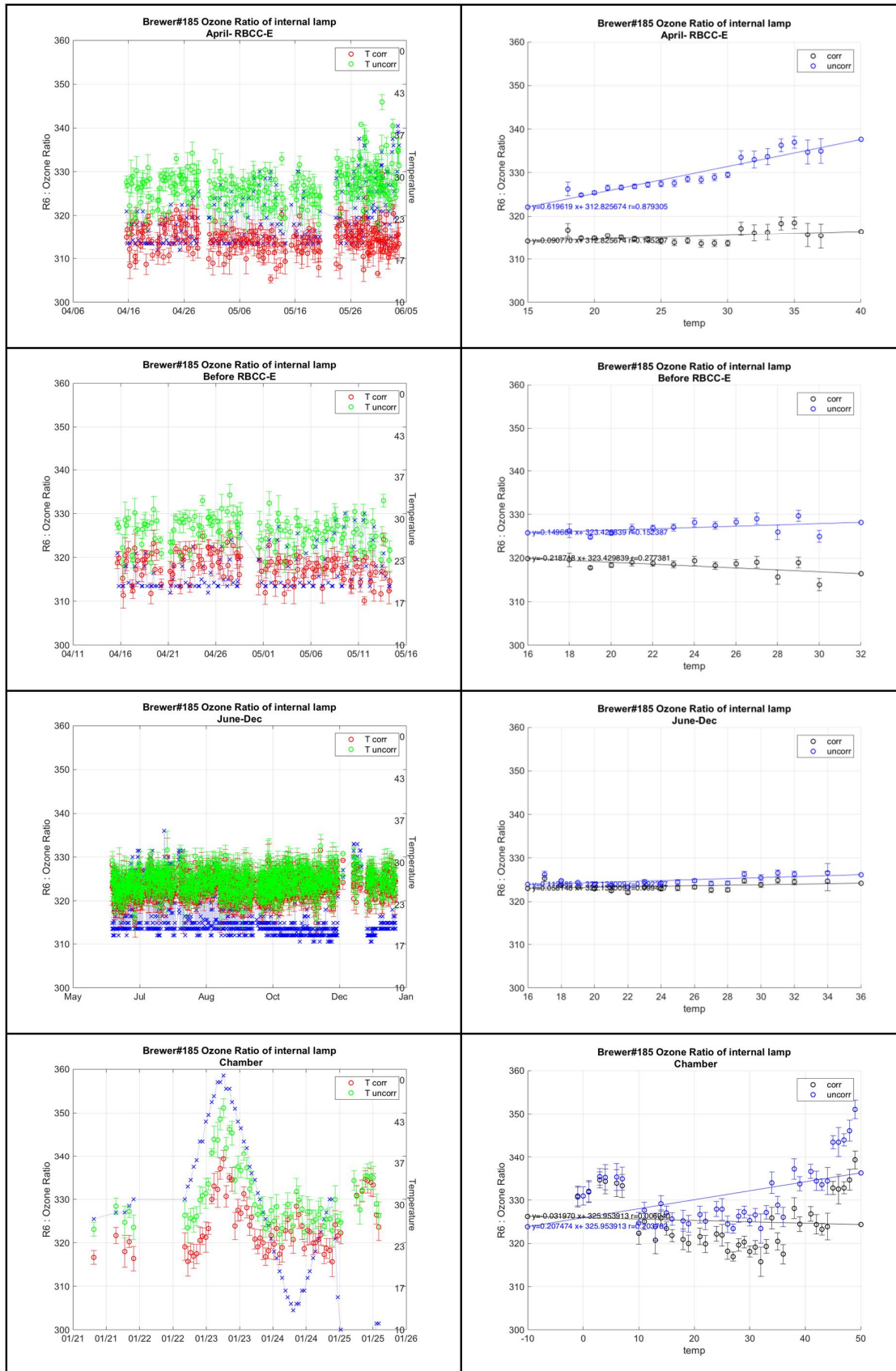


Figure 13. Time series (left) and temperature dependence (right) of the ozone ratio of the internal lamp for the measurements during the selected periods. The ratios are averaged by temperature (every 1 °C) and hourly in the case of time series. The mean and standard deviation are represented by error bars for uncorrected and corrected temperature dependence.

6. Brewer Direct External Lamp ozone measurement

This measurement is a standard ozone measurement using as source the external Xe lamp. The readings of the brewer are dark corrected, converted to counts/second, and dead time corrected. The counts/second are corrected according to the monitor (Fig 5b) and finally logarithmic scaled as in the standard brewer software (Fig 14).

The temperature dependence shows a marked hysteresis (Figure 15), with measurements taken at the same temperature showing 2% differences. At the time of writing this report we don't have an explanation for this behavior, and we don't know which optical element of the instrument can cause this.

We apply the standard method to the corrected data to obtain the temperature coefficients (Figure 16) and finally calculate the ozone ratios with the temperature corrected (Figure 17). In this case the brewer standard method works and successfully removes the temperature dependence of the ratios.

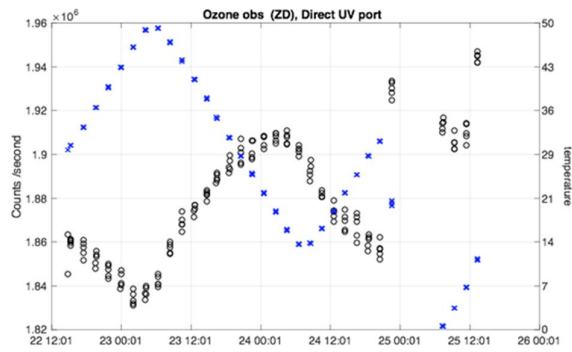


Figure 14. Counts/sec of the ozone direct observation corrected by the monitor (black circles) and the temperature recorded by the brewer (blue crosses).

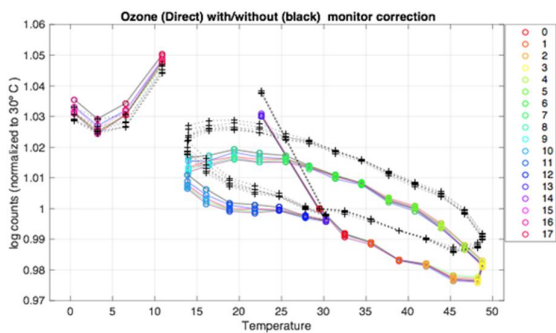


Figure 15. Normalized corrected Counts/sec of the ozone direct observation for the six standard wavelengths against the temperature recorded by the brewer. The color indicates the time of the measurement (each color represents 6 hours)

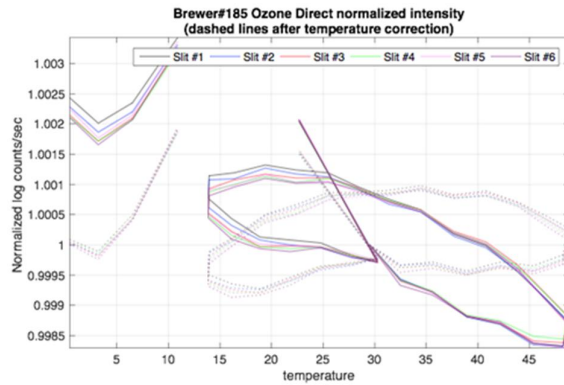


Figure 16. Normalized corrected Counts/sec of the ozone direct observation of the Xe lamp for the six standard wavelengths against the temperature recorded by the brewer.

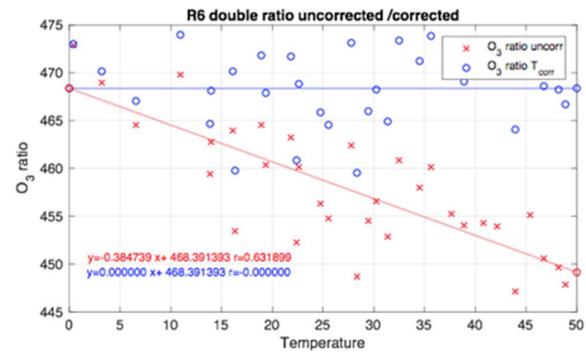


Figure 17. Ozone ratio from the external lamp against the temperature recorded by the brewer, uncorrected (red crosses) and temperature corrected (blue circles).

The figures show the single ratio and double ratios used for the calculation of SO2 and O3 calculated with the internal lamp (Figure 18) and the external lamp (Figure 19), with and without the temperature correction. The parabolic shape of the double ratios observed on the internal lamp during the Chamber experiment is not seen on the external lamp. This could indicate that this behavior at high temperatures, also shown on field observations, is due to changes on the lamp and should not be applied to the ozone calculations.

Direct Ozone Ratios and double Ratios
 Temperature corrected (blue x) / uncorrected (red o)

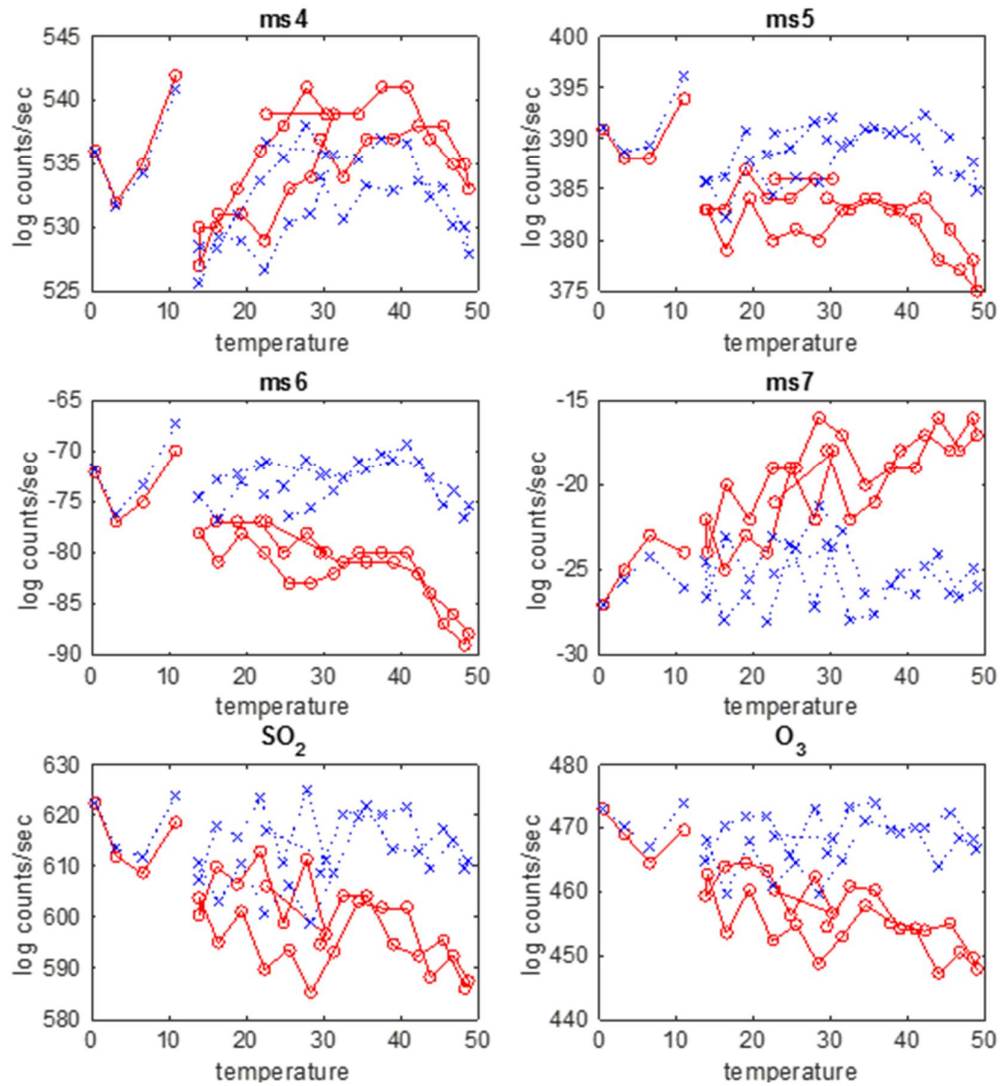


Figure 18. Single and double ratios (for SO₂ and Ozone) from the external lamp against the temperature recorded by the brewer, uncorrected (red circles) and temperature corrected (blue circles).

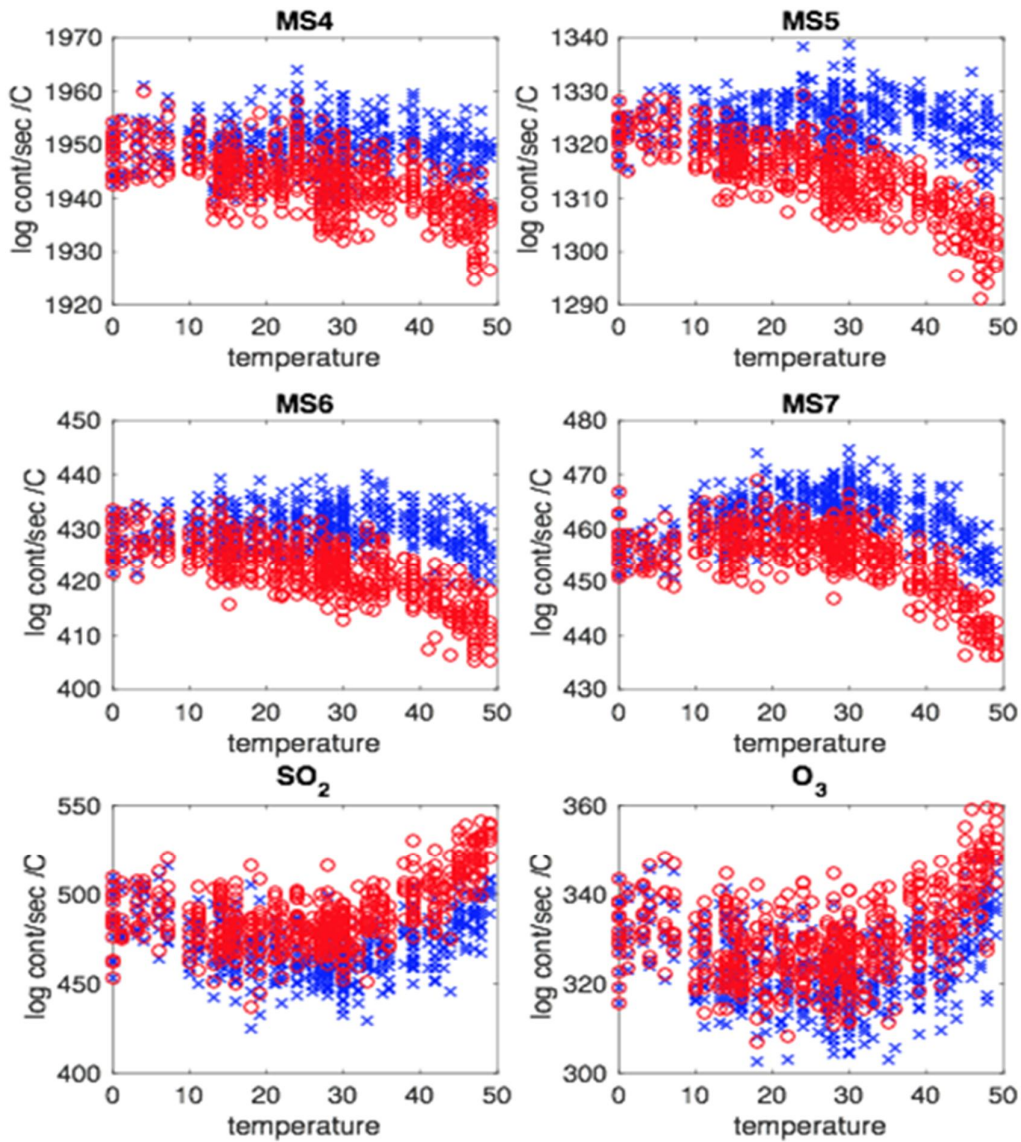


Figure 19. Single and double ratios (for So2 and Ozone) from the internal lamp against the temperature recorded by the brewer, uncorrected (red circles) and temperature corrected (blue circles).

Table 2. Temperature coefficients for the ozone standard wavelengths, for the four internal lamp periods and the External lamp measurements.

Experiment	Wavelength (nm)					
	302.1	306.3	310.1	313.5	316.8	320.1
April - June	-1.485	-1.327	-1.264	-1.316	-1.601	-2.027
Before RBCC-E	-2.438	-2.278	-2.073	-2.039	-2.179	-2.417
Jun-Dec	-0.303	-0.136	0.098	0.135	-0.122	-0.207
Chamber	0.024	0.15	0.292	0.207	-0.093	-0.372
External Xe	-5.031	-4.838	-4.533	-4.475	-4.734	-4.548

As in the case of the spectral temperature dependence which affects the ozone calculation, it is usual to normalize the coefficients to slit#2, giving 0 for the temperature coefficient of this slit. Figure 20 depicts this spectral dependence, showing similar results for the internal lamp in the chamber and during the first analyzed period. The external lamp determination and the second and third periods are in another group. The spectral dependence will be analyzed in more detail with the analysis of uv and aerosol mode measurements.

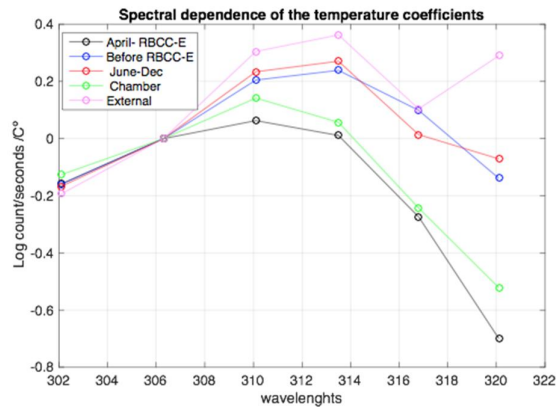


Figure 20. Temperature coefficients normalized to slit#2 vs wavelength (nm).

Conclusions

The temperature dependence is very small for the Brewer#185, only a few counts/seconds per degree, which makes the analysis difficult.

The measurements from direct port shows and negative slope whereas the measurements using the global port and the internal lamp are positive. The field internal lamp measurement, performed in a reduced temperature range (18-34 °C) shows also a negative or near zero slope.

The analysis of the internal lamp is difficult as evident changes on the emission of the internal lamp are not related to the temperature whereas the ozone ratios are not affected by changes on the intensity. This suggests to derive the temperature coefficients from the ratios instead of the individual wavelengths, as the

The ozone ratios using the internal lamp shows a quadratic dependence during the chamber experiment, this behavior is also shown on field measurements with high temperatures, but is not shown on external Xe lamp experiment. This suggests that this behavior is due to changes on the lamp system (lamp and power supply) and the standard lamp correction should not be applied to the ozone observations when the temperature is above 35 °C.

Acknowledgement This work has been supported by the European Metrology Research Programme (EMRP) within the joint research project EMRP ENV59 "Traceability for atmospheric total column ozone." The EMRP is jointly funded by the EMRP participating countries within EURAMET and the European Union.

References

- [1] Dobson, G. M. B., "Forty Years: Research on Atmospheric Ozone at Oxford: a History," *Appl. Opt.* **7**, 387–405 (1968).
- [2] Kerr, J. B., "New methodology for deriving total ozone and other atmospheric variables from Brewer spectrophotometer direct Sun spectra," *J. Geophys. Res.* **107** (D23), 4731 (2002). doi:10.1029/2001JD001227
- [3] Redondas, A., Evans, R., Stuebi, R., Köhler, U. and Weber, M., "Evaluation of the use of five laboratory-determined ozone absorption cross sections in Brewer and Dobson retrieval algorithms," *Atmos.Chem. Phys.* **14**, 1635–1648 (2014). doi:10.5194/acp-14-1635-2014
- [4] Kerr, J. B., McElroy, C.T., Wardle, D.I., Olafson, R.A., and Evans, W.F.J., "The Automated Brewer spectrophotometer," in *Proceedings of the 4th Ozone Symposium on Atmospheric Ozone*, pp. 396–401, D. Reidel, Norwell, Mass., 1985.
- [5] Fioletov, V.E., Kerr, J.B., McElroy, C.T., Wardle, D.I., Savastiouk, V., and Grajnar, T.S., "The Brewer reference triad," *Geophys. Res. Lett.* **32** (2005). doi:10.1029/2005GL024244

Out-of-range stray light characterization of single-monochromator Brewer spectrophotometer

*Tomi Pulli¹, Petri Kärhä¹, Tomi Karppinen², Juha M. Karhu², Kaisa Lakkala²,
Anna Vaskuri¹, Maksim Shpak³, and Joop Mes⁴*

1. Metrology Research Institute, Aalto University, Espoo, Finland
2. Finnish Meteorological Institute - Arctic Research Centre, Sodankylä, Finland
3. MIKES Metrology, VTT Technical Research Centre of Finland Ltd., Espoo, Finland
4. Kipp & Zonen, Delft, Netherlands

Introduction

One of the workpackages of the ongoing EMRP project ENV59 Atmoz ‘Traceability for atmospheric total column ozone’ is dedicated to characterizing the instruments of the two major ozone measurement networks, Brewer and Dobson. One of the activities in the workpackage is the study of the out-of-range stray light properties of single-monochromator Brewer spectrophotometers. The motivation for this activity is the observed discrepancy in the measured spectral irradiances at short wavelengths, below approximately 300 nm, between the single- and double-monochromator Brewer instruments [1]. The in-range stray light correction of single-monochromator Brewers has been shown to improve the consistency between the results of the two instrument types considerably [1-3], but even after the correction, the single-monochromator instruments give out higher values than double-monochromator ones at short wavelengths where there should be very little solar UV radiation. It is reasonable to suspect that the residual error could be caused, at least in part, by out-of-range stray light.

The in-range stray light properties of Brewer instruments are typically characterized using a HeCd laser at 325 nm [2,3], with an assumption that the stray light characteristics remain the same at other in-range wavelengths. Characterization and correction of the out-of-range stray light is inherently more difficult than that of the in-range stray light, because the instrument does not measure the wavelength component responsible for stray light directly, but only the resulting stray light. In case of a laser-based stray light characterization this means that we cannot measure the signal level at the peak wavelength directly with the instrument, but can only observe the short wavelength tails of the slit scattering function. Moreover, the stray light caused by a laser line whose wavelength is relatively far from the passband of the instrument may be difficult to detect during the characterization, but can still potentially cause issues in the real measurement conditions due to (a) the high irradiance level of solar radiation at out-of-range (visible) wavelengths compared to the in-range (UV) wavelengths, and (b) the broad sensitivity range of the photomultiplier tube (PMT) of the instrument. To combat the issues of out-of-range stray light, the two types of single-monochromator Brewer instruments currently in use, types MKII and MKIV, are equipped with solar blind filters – consisting of a nickel sulfate (NiSO₄) filter sandwiched between two glass filters – that block radiation in the visible wavelength range. Even so, out-of-range stray light can still cause issues if the filter transmittance in the stopband is too high, or if there the filter has additional transmission bands in the visible wavelength range.

In order to study the out-of-range stray light characteristics of single-monochromator Brewer instruments, the Brewer MKII #037 of Finnish Meteorological Institute (FMI) was characterized in Sodankylä using discrete laser wavelengths in the UV and visible wavelength range. The results of this characterization are presented in the following section. To obtain better understanding of the potential levels of out-of-range stray light, the transmittance of the NiSO₄-based UV bandpass filter of the Brewer instrument was characterized both spatially and as a function of wavelength. These results are also presented in the paper.

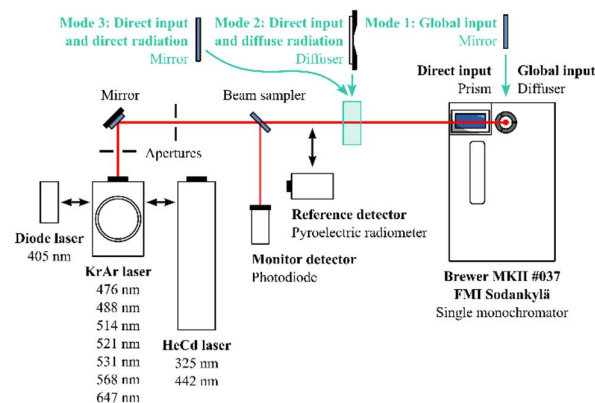


Figure 1. Measurement setup for the out-of-range stray light characterization of the Brewer spectrophotometer. The laser lines used in the characterization are listed below the corresponding lasers.

Out-of-range stray light characterization of Brewer MKII

Measurement setup

The stray light characterization of Brewer MKII #037 of FMI was carried out in February 2015 in Sodankylä. The schematic view of the measurement setup is shown in Figure 1. Three lasers – a helium-cadmium (HeCd), a krypton-argon (KrAr), and a gallium nitride (GaN) diode laser – were used as radiation sources. The intensity of each laser line was measured before the actual stray light measurement by placing a reference detector, a pyroelectric radiometer, in front of the laser beam. The reference detector was moved aside before each stray light measurement. During all the measurements, the stability of the laser was monitored using a combination of a beam sampler and a photodiode.

The stray light of the Brewer spectrophotometer was characterized in three measurement geometries. In Mode 1,

the laser beam was guided to the global diffuser entrance port of the instrument using a mirror assembly that was constructed on top of the spectrophotometer housing. In Mode 2, an auxiliary transmissive diffuser was placed in front of the laser beam, and the direct input port was aligned to view the back surface of the diffuser. Finally, in Mode 3, the laser beam was guided into the direct input port of the spectrophotometer by placing a mirror between the beam sampler and the instrument.

Of all the available laser lines of the three lasers, only the 325-nm line of the HeCd laser was within the wavelength range limited by the mechanical movement of the monochromator. For this reason, the slit scattering function could be measured for the 325-nm line alone, and only the short-wavelength tails of the stray light profile are observable for the other lines. Moreover, only the 325-nm line of the HeCd laser was in the nominal passband of the solar blind filter. This means that the level of stray light entering the PMT at the input wavelength of 325 nm is expected to be significantly higher than that at any other wavelength available in the characterization setup.

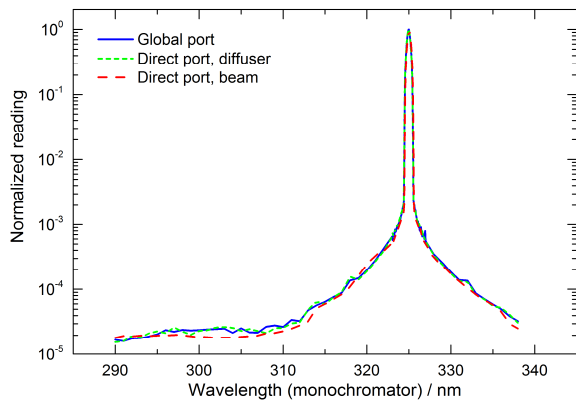


Figure 2. Slit scattering function of Brewer MKII #037 as a function of monochromator wavelength at a fixed radiation wavelength of 325 nm using different measurement geometries.

Measurement results

The slit scattering function of the spectrophotometer at 325 nm was measured in all three measurement geometries (Modes 1 – 3 in Figure 1). The slit scattering functions as a function of monochromator wavelength setting are shown in Figure 2. The area around the peak of the laser line (323 – 327 nm) was scanned in 0.1 nm steps, while a step-size of 1 nm was used for the tails of the slit scattering function. In order to cover a wider wavelength range than would be possible with a single slit of the Brewer instrument, slit 1 of the cylindrical slit mask was used for the short wavelength side of the stray light measurement (290 – 323 nm), and slit 5 for the long wavelength side (327 – 338 nm). The slit scattering functions shown in Figure 2 were constructed from the measurements at these three wavelength ranges. The internal neutral density (ND) filters of the Brewer instrument were used to attenuate the signal near the laser peak in all three measurement geometries. In addition, when the laser beam was guided directly into the direct port of the instrument (Mode 3), the internal ground glass diffuser of the entrance optics was utilized.

The out-of-range stray light was measured in Mode 1 with the HeCd laser (at the wavelength of 442 nm), the diode laser (405 nm), and the KrAr laser (476 nm, 488 nm, 514 nm, 521 nm, 531 nm, 568 nm, and 647 nm). In addition, the out-of-range stray light was also measured through the direct port (Modes 2 and 3) with the 442-nm line of the HeCd laser. No ND filters were used during the measurements, but the ground glass diffuser was utilized in measurement Mode 3. The possible out-of-range stray light was below the noise floor of the measurements in all measurement geometries and all the studied wavelengths.

The worst-case out-of-range stray light can be estimated by calculating the ratio between the stray light levels for the in-range stray light at 325 nm and the out-of-range stray light at x nm as

$$R = \frac{C_{\text{stray},x \text{ nm}} / (t_{\text{int},x \text{ nm}} P_{x \text{ nm}})}{C_{\text{stray},325 \text{ nm}} / (t_{\text{int},325 \text{ nm}} P_{325 \text{ nm}})}, \quad (1)$$

where C_{stray} refers to the measured stray light counts at the monochromator wavelength of interest at integration time t_{int} and laser power P . At the radiation wavelength of 325 nm, the stray light as a ratio of counts in the wavelength range of interest to the peak counts can be estimated directly from Figure 2. In the monochromator wavelength range of 300 – 310 nm, the relative stray light is about $2.5 \cdot 10^{-5}$. The corresponding relative stray light at out-of-range wavelengths can be estimated by multiplying this value by the ratio R . This gives the stray light level caused by out-of-range radiation of a given wavelength assuming the same integration time and laser power as with 325 nm, normalized such that peak value at 325 nm is unity (as in Figure 2).

The worst-case estimates for the ratio R and the relative stray light at 300 – 310 nm are presented in Table 1 for different measurement geometries and wavelengths. As an example, when the laser beam was guided directly into the direct port of the instrument (Mode 3), the laser power at 325 nm measured with the pyroelectric radiometer was 0.7 mW, the number of integration cycles was 5, and the dark-subtracted average stray light at 300 – 310 nm was 1030 counts. Correspondingly, the laser power and the number of integration cycles at 442 nm were 18 mW and 40 cycles. As no out-of-range stray light was observed in the results, the standard deviation of the measured signal (about 40 counts at the integration of 40 cycles) was used as the worst-case estimate of stray light counts. These values indicate that the stray light at 300 – 310 nm caused by radiation at 442 nm is approximately $R = 1.9 \cdot 10^{-4}$ times that of the stray light caused by radiation at 325 nm.

Since no out-of-range stray light was observed at any of the studied wavelengths, the worst-case estimates at different wavelengths depend mainly on the optical power of the laser lines. The measurement geometry also affects the results through differences in the signal of the PMT at 325 nm, Mode 3 giving the strongest and Mode 2 the weakest signal.

Table 1. Ratio R of equation (1) and the relative stray light at 300 – 310 nm at different laser wavelengths and measurement geometries. The values for laser wavelengths other than 325 nm should be considered worst-case estimates.

Mode	Wavelength	R	Stray light
1	325 nm	1.0	$2.5 \cdot 10^{-5}$
	405 nm	$9.5 \cdot 10^{-4}$	$2.4 \cdot 10^{-8}$
	442 nm	$1.0 \cdot 10^{-3}$	$2.6 \cdot 10^{-8}$
	477 nm	$3.9 \cdot 10^{-3}$	$9.8 \cdot 10^{-8}$
	488 nm	$2.4 \cdot 10^{-3}$	$6.0 \cdot 10^{-8}$
	515 nm	$5.1 \cdot 10^{-3}$	$1.3 \cdot 10^{-7}$
	521 nm	$1.8 \cdot 10^{-3}$	$4.5 \cdot 10^{-8}$
	531 nm	$1.9 \cdot 10^{-3}$	$4.7 \cdot 10^{-8}$
	568 nm	$3.9 \cdot 10^{-3}$	$9.7 \cdot 10^{-8}$
2	325 nm	1.0	$2.5 \cdot 10^{-5}$
	442 nm	$3.3 \cdot 10^{-3}$	$8.1 \cdot 10^{-8}$
3	325 nm	1.0	$2.0 \cdot 10^{-5}$
	442 nm	$1.9 \cdot 10^{-4}$	$3.8 \cdot 10^{-9}$

Figure 3 shows the slit scattering function of the Brewer instrument as a function of the wavelength of radiation at fixed monochromator position of 325 nm (as opposed to the fixed radiation wavelength of Figure 2) in measurement Mode 1. The continuous line of Figure 3 is derived from the slit scattering function of Figure 2, taking into account the spectral responsivity of the Brewer instrument, presented in ref [3]. In analyzing the data, the slit scattering function was assumed to retain its shape (shown in Figure 2) at different in-range radiation wavelengths. The individual points of Figure 3 are the stray light values of Table 1.

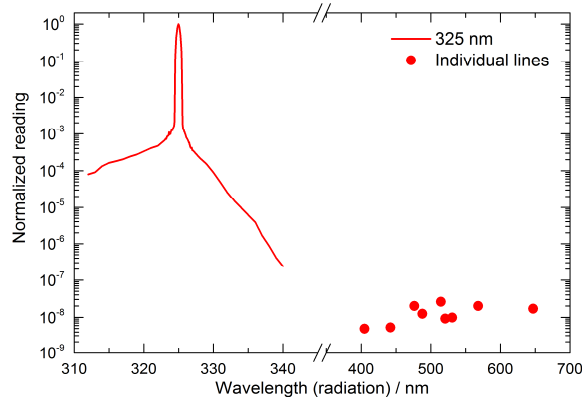


Figure 3. Slit scattering function of Brewer MKII #037 as a function of laser wavelength at a fixed monochromator position of 325 nm in Mode 1.

Solar blind filter characterization

Spectral measurement

The transmittance of a new solar blind filter – consisting of a NiSO_4 element between two glass filters – of the single-monochromator Brewer spectrophotometer was measured spectrally using a commercial spectrophotometer, PerkinElmer Lambda 900. The area around the passband of the filter (200 – 345 nm) was measured in the standard measurement mode of the instrument. To increase the

signal-to-noise ratio of the measurement, cascade measurement was used in the area around the stopband of the filter (340 – 850 nm), i.e. the transmittance of the filter was compared to that of a known ND filter with approximately 1 % transmittance. The size of the rectangular beam was approximately $3 \times 11 \text{ mm}^2$ in the UV range and $5 \times 11 \text{ mm}^2$ in the visible wavelength range. The bandwidths were 1 nm and 5 nm, in the UV and visible wavelength ranges, respectively.

The spectral transmittance of the filter is shown in Figure 4. The peak transmittance at 300 nm is about 73 %. The worst-case stopband transmittance of the filter in the visible wavelength range is of the order of 10^{-7} . The noise floor in short wavelength stopband is approximately two orders of magnitude higher than this value because the area was measured in non-cascade mode. There are no leakage bands in the visible wavelength range above the noise floor of 10^{-7} .

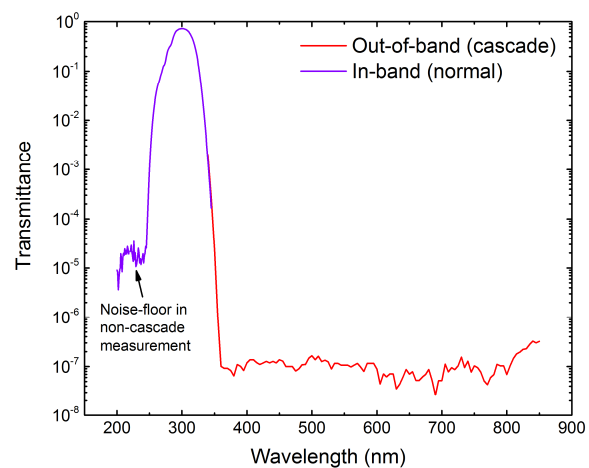


Figure 4. Spectral transmittance of the solar blind filter of Brewer spectrophotometer.

Spatial measurement

The spatial uniformity of the filter was measured in the automated laser setup of Aalto designed for characterizing optical components [4]. The setup consists of various lasers, beam conditioning optics, a sample holder mounted on an XY-translator, and an integrating sphere with a photodiode to detect the transmitted optical power. The 325 nm line of a HeCd laser was used in the measurement. The $1/e^2$ diameter of the beam was 1.6 mm. The area of the filter was scanned in along two perpendicular axis in 0.5 mm intervals.

The result of the spatial transmittance measurement is shown in Figure 5. The transmittance of the filter is relatively smooth near the center of the filter. There is a drop in transmittance of about 10 % in one spot near the edge of the filter. No major defects could be detected on the surfaces of the filter upon inspection, and thus it is possible that the defect is located within the structure of NiSO_4 or between the NiSO_4 filter and the glass cover plates of the filter assembly.

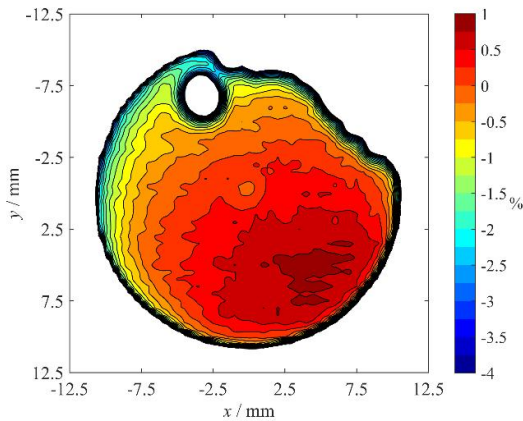


Figure 5. Spatial uniformity of the solar blind filter of Brewer spectrophotometer. The color axis describes the difference in transmittance relative to the transmittance of the center of the filter.

Conclusions

The out-of-range stray light properties of a single-monochromator Brewer spectrophotometer were measured using multiple discrete laser wavelengths. No out-of-range stray light was observed at any of the out-of-range wavelengths, i.e. the measurement was noise limited. The results indicate that the stray light caused by radiation at 442 nm is at least $5 \cdot 10^3$ times smaller than that caused by radiation at 325 nm. At other wavelengths, the worst-case stray light estimates are higher due to lower laser power levels.

A better estimate of the worst-case out-of-range stray light of the single-monochromator Brewer instruments can be reached by studying the properties of the solar blind filter positioned in front of the PMT of the instrument. The worst-case transmittance of the filter at the wavelength range of 360 – 850 nm is of the order of 10^{-7} . The measurement in the visible wavelength range is noise limited, and so the actual transmittance is likely to be even smaller.

If we assume that the out-of-range stray light in absence of the solar blind filter is, at most, of the order of the in-range stray light, approximately $2 \cdot 10^{-5}$ (see Figure 2), and combine this with the stopband transmittance of the solar

blind filter, approximately 10^{-7} , we end up with a worst-case out-of-range stray light estimate of the order of $2 \cdot 10^{-12}$. This is lower than the measured in-range stray light of a double-monochromator Brewer spectrophotometer [2,3], and thus it is unlikely that the higher spectral irradiance values of single-monochromator instruments at short wavelengths compared to those of double-monochromator instruments are explained by the poor out-of-range stray light characteristics of single-monochromator instruments. However, as the single-monochromator instruments exhibit significant in-range stray light, further research is still required in this area. One of the major topics for further study is whether the slit scattering function remains constant or changes shape from wavelength to wavelength in the passband and the transition band of the instrument. It is also as of yet unknown how the transmittance characteristics of used solar blind filters differ from those of new filters, or how the humidity absorbed by the filter affects the transmittance in long and short terms.

Acknowledgement This work has been supported by the European Metrology Research Programme (EMRP) within the joint research project EMRP ENV59 “Traceability for atmospheric total column ozone.” The EMRP is jointly funded by the EMRP participating countries within EURAMET and the European Union.

References

- [1] A. F. Bais, C. S. Zerefos, and C. T. McElroy, “Solar UVB measurements with the double- and single-monochromator Brewer Ozone Spectrophotometers,” *Geophys. Res. Lett.* **23**, 833–836 (1996).
- [2] V. E. Fioletov, J. B. Kerr, D. I. Wardle, and E. WU, “Correction of stray light for the Brewer single monochromator,” *Proc. Quadrennial Ozone Symp.*, Sapporo, Japan, 369–370 (2000).
- [3] T. Karppinen, A. Redondas, R. D. Garcia, K. Lakkala, C. T. McElroy, and E. Kyrö, “Compensating for the Effects of Stray Light in Single-Monochromator Brewer Spectrophotometer Ozone Retrieval,” *Atmosphere-Ocean* **53**, 66–73 (2014).
- [4] A. Vaskuri, P. Kärhä, A. Heikkilä, and E. Ikonen, “High-resolution setup for measuring wavelength sensitivity of photoyellowing of translucent materials,” *Rev. Sci. Instrum.* **86**, 103103 (2015).

A UV/Vis solar spectroradiometer for the remote sensing of the Atmosphere (PSR-ATMOZ)

*Julian Gröbner¹, Natalia Kouremeti¹, Patrik Langer¹, Ricco Soder¹,
Pascal Schlatter¹, Marek Smid², and Geiland Porrovecchio²*

1. Physikalisches-Meteorologisches Observatorium Davos, World Radiation Center, Davos, Switzerland
2. Cesky Metrologicky Institut, Brno, Czech Republic

Introduction

The composition of the atmosphere can be probed remotely by measuring the solar radiation which is absorbed and scattered in the atmosphere. Most commonly, the direct solar irradiance which is scattered and absorbed in the atmosphere is measured, in order to retrieve the total column amount of various atmospheric trace gases. In the frame of the EMRP project ATMOZ “Traceability for total column ozone”, instruments based on diode array detectors are used to determine the total column ozone amount using measurements of direct solar irradiance in combination with a retrieval model based on the Beer-Lambert law.

Ozone is usually retrieved in the UV part of the solar spectrum, between 300 nm and 340 nm due to its high absorption cross-section in that wavelength range. Unfortunately, this strong ozone absorption attenuates the solar radiation by several orders of magnitude over this very short wavelength range, leading to several significant constraining factors for the instruments measuring this quantity:

- Large dynamic range of up to 5 orders magnitude over which the instrument has to measure reliably the solar radiation, from very low to very high signal levels. The challenges which need to be overcome are the high sensitivity required at short wavelengths on the one hand, and the problem of saturation at longer wavelengths on the other,
- Irradiance at short wavelengths is affected by scattered light within the detector. Correction methods based on a comprehensive characterisation of the spectroradiometer using tuneable laser sources and sophisticated post-processing techniques are needed to correct for this so called stray-light,
- The retrieval of the total column ozone used the characteristic spectral signature of the ozone absorption cross-sections, which requires a high spectral resolution of the spectroradiometer,
- The retrieval of an atmospheric trace gas from direct solar irradiance measurements using the Beer-Lambert law necessitates a reference solar spectrum with no atmospheric attenuation, e.g. from the top of the atmosphere. This reference spectrum can be either a literature solar spectrum, or else based on an in-situ retrieval using the zero airmass extrapolation (Langley-plot technique). Both techniques rely on the fact that the spectroradiometer remains stable from the time of its calibration to its subsequent use for retrieving atmospheric trace gases.

Spectroradiometer design specifications

The spectroradiometer was designed with the objective of allowing not only the retrieval of total column ozone, but to be versatile enough to retrieve other trace gases such as nitrogen dioxide (NO₂), oxygen dimer (O₄) and water vapour (H₂O) in the visible wavelength range between 400 nm to 670 nm as well. Therefore, a nominal resolution of 0.3 nm, defined as the full width at half maximum (FWHM) was chosen.

As shown in Figure 1, model simulations have demonstrated that an over-sampling of at least 6 pixels per FWHM is required to allow full spectral retrieval of the solar spectrum at any wavelength with less than 0.1% uncertainty, from the discretely sampled solar spectrum based on the detector pixels.

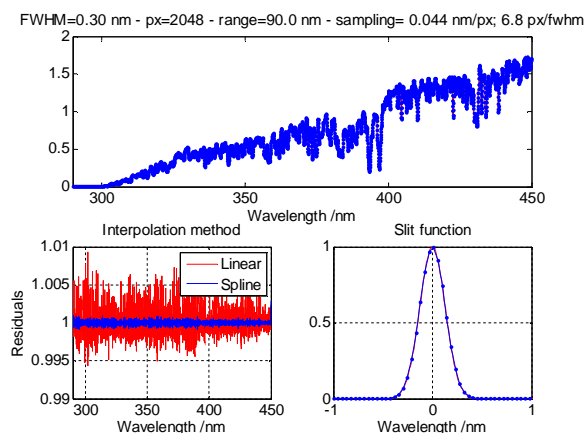


Figure 1. Simulated solar spectrum using a spectral resolution of 0.3 nm and a sampling range of 90 nm with a detector having 2048 pixels. The top figure shows the attenuated solar spectrum and the left figure the residuals from interpolating the discretely sampled solar spectrum. The right figure shows the instrument slit function of 0.3 nm and the corresponding pixels as dots.

To achieve this high resolution of 0.3 nm over the desired wavelength range between 290 nm and 560 nm with commercial detectors having only 2048 pixels, a novel approach based on a CCD array detector and a moving grating was required: by imaging only a part of the solar spectrum on the detector for a specific grating rotation, different regions of the solar spectrum can be sampled for retrieving distinct atmospheric species, based on their spectral absorption cross-sections, as will be discussed later.

Spectroradiometer design

The spectrometer was designed using the ray-tracing software Zemax, with the objective of achieving a resolution of 0.3 nm, constant over the length of the CCD detector. To achieve the required resolution, a Cerny-Turner design was selected. To reduce the aberrations in the system, a parabolic mirror is used as collimating mirror, while a custom-made spherical mirror is used as focusing mirror. The high resolution and large oversampling on the detector is obtained by using a diffraction grating with 1800 lines /mm, dispersing a wavelength range of about 90 nm across the detector. The nominal wavelength range in

the default grating position is 295 nm to 390 nm with a full width at half maximum resolution of 0.25 nm. The instrument is designed to cover the UV/Vis wavelength range, in view of its future use to retrieve trace gases at longer wavelengths as well. Therefore the grating is mounted on a high precision rotating turret, with the possibility of sampling also other regions of the solar spectrum. Table 1 displays the main characteristics of the spectroradiometer as retrieved from the design analysis, for five chosen wavelengths regions, based on their use for the retrieval of atmospheric trace gases. Obviously, any intermediate wavelength region can be selected as well by rotating the grating to a specific intermediate angle.

Table 1. Design characteristics of the spectroradiometer obtained from the ray-tracing analysis, using a detector with 2048 pixels.

	Min Wavelength (nm)	Max Wavelength (nm)	Imaged Wavelengths (nm)	linear step nm/pixel	FWHM (nm)	Pixels within the FWHM
UV	295.0	386.8	91.8	0.045	0.25±0.02	5.6
Vis	376.0	460.3	84.3	0.041	0.25±0.03	6.1
Vis-II	600.0	660.0	60.0	0.029	0.21 to 0.31	7-10
NIR	740.0	780.0	40.0	0.020	0.17 to 0.32	10-15
NIR-II	852.0	873.3	21.3	0.010	~1 nm	100

As can be seen in Table 1, the instrument is designed to measure the solar irradiance spectrum with a resolution of better than 0.3 nm over the wavelength range from 295 nm to 870 nm.

Two sample slit functions as retrieved from the ray-tracing analysis are shown in Figure 2, for 340 nm and 440 nm and a FWHM of 0.25 nm.

The optical bench of the instrument is shown in Figure 3 together with the main optical components in place.

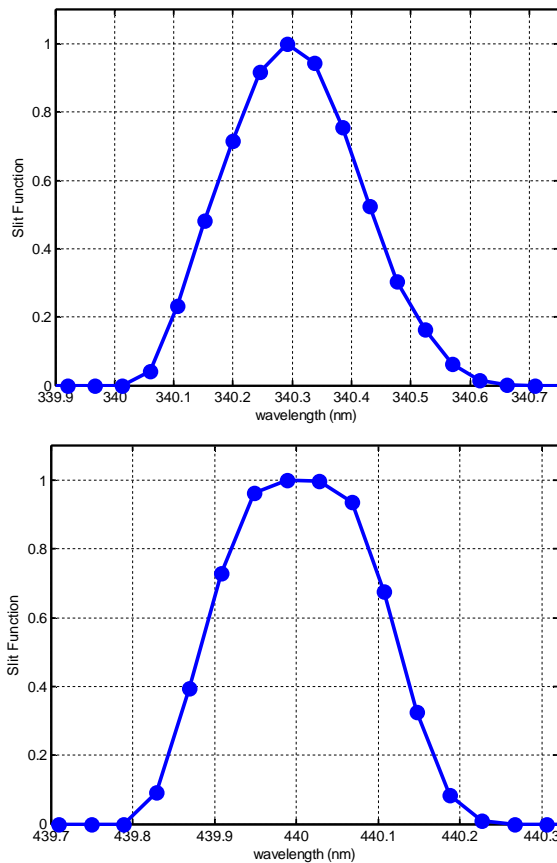


Figure 2. Sample slit functions retrieved from the ray tracing analysis. The slit function on top is for a wavelength of 340 nm, while the lower figure shows the slit function of the spectroradiometer at 440 nm.

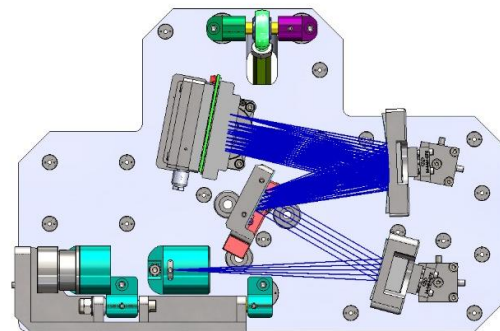


Figure 3. Optical bench of the spectroradiometer with a sample ray initiating at the entrance slit (bottom part) and reaching the detector (top). The dimensions of the optical bench are 315 mm in length by 210 mm in width.

The radiation is coupled into the spectroradiometer with an optical fiber, followed by a set of collimating lenses and two filter wheels (not shown). The filter wheels are used to attenuate the radiation intensity by various neutral density filters, while interference filters placed in the second filter wheel are used to restrict the passband of the spectroradiometer to the specific wavelength region selected by the grating position. The latter is used to improve the stray light characteristics of the instrument by reducing the out of range stray light (Nevas *et al.*, 2014). An entrance slit of width 60 μm and height 1 mm was selected to produce the required resolution of 0.3 nm. The optical bench is made out of a carbon alloy with a very low thermal expansion coefficient. Since the detector will be

Thematic Network for Ultraviolet Measurements

cooled to a nominal temperature of 253 K (see next section), the whole optical bench is enclosed in an air-tight enclosure and flushed with nitrogen.

Detector Selection

The specifications for the detector to use for this spectroradiometer had to fulfill the following requirements:

- High sensitivity,
- At least 2048 pixels over the spatial length of the detector of not more than 25 mm to limit the aberrations of the system
- Height of the detector of at least 2 mm in order to under-fill the detector. This is necessary in order to be insensitive to small fluctuations in the thermal environment which would lead to large intensity variations in case of an overfilled detector,
- Integrated TE-Cooler in case of CCD detectors.

Based on the availability of commercial detectors, the back-thinned Hamamatsu CCD imaging sensors family S10141 were taken into consideration. Three devices with 2048 pixels in length and 122, 250, and 506 effective pixels in height and integrated TE-cooler were investigated for their noise characteristics. A data acquisition system from the company Jeti was used, which has a nominal resolution of 16 bits and an integrated Peltier driving stage.

The effective dynamic range (*EDR*),

$$EDR = \frac{2^{ADbits} - \text{Dark signal}}{\text{std}(\text{Dark Signal})} \quad (1)$$

was used as criterion for selecting the most promising candidate. The results are shown in Figure 4 for the three CCD devices. As comparison, we have also included the NMOS detector used in the precision solar spectroradiometer (PSR), developed by PMOD/WRC. The *EDR* is displayed as a function of integration time, between 10 ms and 10 seconds, covering 4 orders of magnitude.

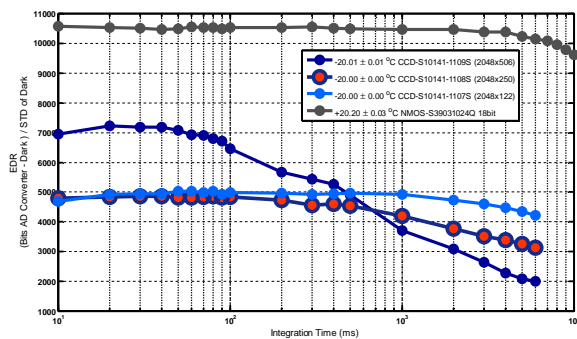


Figure 4. Effective dynamic range (*EDR*) for Hamamatsu CCD detectors type S10141-110xS and NMOS S3903.

As can be seen in Figure 4, the NMOS detector performs best, with an *EDR* of more than 10 000 nearly constant over the whole integration range. However its sensitivity is more than a factor of 100 less in the UV wavelength region than the CCD detectors, which was the main reason why it was not used here.

The *EDR* determined for the three CCD detectors S10141-1107S (2048x122 px), S10141-1108S (2048x250 px), and S10141-1109S (2048x506 px) show a large variability between 2 000 and 7 000, for integration times between 10 ms and 10 seconds. Note that, this large integration range is needed to cover the dynamic range of the solar spectrum in the UV on the one hand and when switching between the direct irradiance and radiance operating modes of the instrument on the other. The largest CDD candidate, S1109S, was excluded even though it showed the highest *EDR* at integration times below 500 ms. However the unexplained decrease of the *EDR* and the spectral dependence of the dark signal (not shown) at larger integration times could indicate a problem with this particular detector.

The remaining candidate fulfilling all requirements was S1108S, 2048 x 250 pixels, with an *EDR* between 4000 and of 5000, for the integration range between 10 ms and 1 sec. The slight decrease in *EDR* to 3000 at integration times of up to 10 sec might need to be investigated once the instrument is finally assembled.

Conclusions

We have designed a spectroradiometer for the UV/Vis wavelength range with a high resolution of 0.3 nm across its operational wavelength range. The instrument is designed for measuring the solar spectrum between 295 nm to 780 nm by rotating the grating to specific positions and imaging up to 95 nm of the solar spectrum on the detector.

The instrument is expected to cover 9 orders of magnitude of incoming solar radiation, by combining the dynamic range of the detector, the available integration time range between 10 ms and 10 sec, and the attenuations available in the fore-optics in terms of neutral density filters between ND0 and ND2.5.

Acknowledgement This work has been supported by the European Metrology Research Programme (EMRP) within the joint research project EMRP ENV59 “Traceability for atmospheric total column ozone.” The EMRP is jointly funded by the EMRP participating countries within EURAMET and the European Union.

Reference

Nevas, S., Gröbner J., Egli, L., and Blumthaler, M., “Stray light correction of array spectroradiometers for solar UV measurements,” *Appl. Opt.* **53**, 19, 4313-4319 (2014).

UV-LED based source for tracking radiometric stability of array spectroradiometers

Saulius Nevas, Sven Pape, Fabian Kemus, Meelis-Mait Sildoja, and Stefan Pendsa

Physikalisch-Technische Bundesanstalt (PTB), Braunschweig, Germany

Introduction

Traditionally total column ozone (TOC) in the atmosphere has been retrieved from measurements of the solar ultraviolet (UV) radiation carried out first by the Dobson and latter also by the Brewer spectrophotometers at several discrete wavelengths. Using the full solar UV spectrum for the TOC retrieval could offer some advantages, provided reliable measurement data are available. Within the EMRP ENV59 project ATMOZ “Traceability for total column ozone”, efforts are being made to develop, characterise, and apply array spectroradiometers to measure the direct solar UV irradiance. One of the key requirements for the instruments in this application is their radiometric stability. For this purpose a compact and stable reference source based on state-of-the-art commercially available light emitting diodes (LEDs) is being built. The UV-LEDs based source system will allow tracking radiometric stability and wavelength scale of the array spectroradiometers. In this report we present preliminary design of the UV source system and results of the stability studies on the UV-LEDs.

Design of the source

The spectral range of interest for the TOC retrieval spans wavelengths from 300 nm to 350 nm. So far there are no many commercially available alternatives among UV-LED products that would enable a gapless coverage of this spectral range. UV-LEDs with peak wavelengths distributed from 240 nm to 355 nm every 5 nm are provided by the Sensor Electronic Technology, Inc. (SETi). Some of the LEDs were investigated for similar purposes in the previous study [1]. In the mean time a new product has been introduced into market. At present also several LED chips can be combined in a single package. Such a design is especially attractive having compactness and efficient system integration in mind. The original source design idea was to attach the UV-LED device to a port of a small integrating sphere. An output port of the sphere would then be coupled to entrance optics of array spectroradiometers for the direct solar UV irradiance measurements. Selected constellation of the UV-LEDs in the device included 9 chips in a TO8 package with nominal peak wavelengths at 300 nm, 310 nm, 320 nm, 330 nm and 365 nm. Two chips at every peak wavelength except at 365 nm were chosen. The selection of the UV-LED chips was based on information collected from the previous studies as reported in [1]. For radiometrically stable operation of the UV-LEDs it is critical to ensure constant current and diode junction temperature conditions. The LEDs are operated at a nominal current of 20 mA. Every anode of the chip has a dedicated pin in the package while the cathode is common. Hence, to operate all the chips simultaneously 9 stable current drivers are needed. In the first stage of the project, seasoning studies, two Keithley source meters of type 2611A and 2612B were used as LED current drivers enabling a simultaneous operation of three LEDs. In the

latter stage when the UV-LED source is built and used, stabilised current for every chip is provided by LED current drivers of type Supertex CL2 realised in a compact integrated circuit (IC) chip. The stabilised current drivers were proved to ensure current stability within $\pm 5 \mu\text{A}$. To control the temperature of the UV-LEDs, the device was mounted in a copper block. Its temperature is controlled by a Peltier element to $\pm 0.05\text{K}$. The heat dissipated from the Peltier element is given out to a cooling body with a fan.

Radiometric stability of the UV-LEDs

Based on the results of earlier studies reported in [1], seasoning under well defined conditions is necessary until the required stability of the individual LED chips is achieved. Aimed value was a relative irradiance change of $5 \times 10^{-4}/\text{h}$. The seasoning studies were carried out according to a following scheme. The UV-LED device was attached to a port of a PTFE-based integrating sphere with a diameter of 50 mm. The integrating sphere was planned also to be used as part of the UV-LED source. The radiometric output from the UV-LEDs and sphere combination at an output port of the sphere was monitored by an array spectroradiometer. Additionally, a silicon monitor photodiode was attached to a third port of the sphere. A batch of three UV-LEDs was aged at a time. Voltages over each of the LED chips were monitored and recorded during the burn-in time.

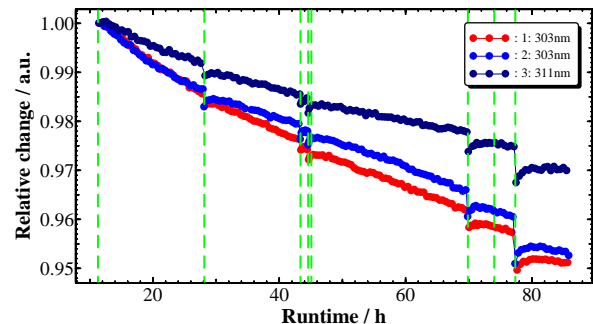


Figure 1. Relative change in the radiometric flux generated by UV-LEDs chips with peak wavelengths at 303 nm, 303 nm and 311 nm attached to an integrating sphere. The measurements were done at an output port of the integrating sphere.

Seasoning results for the first batch of the LED chips are shown in Figure 1. Here, relative changes of irradiance generated by the three UV-LEDs are shown. Vertical green lines show breaks in the operation of the LEDs. The breaks were in the range from ca. 2 h to 15 h. It was observed that the longer the rest period was, the larger was the observed discontinuity in the radiometric output when the LEDs were switched on again. The poor reproducibility was traced back to a change in the throughput of the integrating sphere under the UV radiation of the LEDs. Figure 2 shows seasoning behaviour of the same LEDs monitored without

the integrating sphere. I.e., the UV-LED device was irradiating the input optics of the array spectroradiometer and the monitor photodiode directly. As can be seen from the figure, the apparent seasoning rate changed while the reproducibility of the LED irradiance values was significantly improved. The observations with respect to the changes in the throughput of the PTFE based integrating sphere comply with earlier studied changes of the PTFE material under a high level of UV irradiance [2]. As a result of these observations a decision was taken to pursue further UV-LED seasoning studies without the integrating sphere. Also it was concluded that the use of an integrating sphere in the reference source system would deteriorate its stability and reproducibility. Voltages of the three UV-LED chips during the seasoning studies are shown in Figure 3. The figure shows that most of the changes in the LED parameters had happened within the first 30 hours of operation.

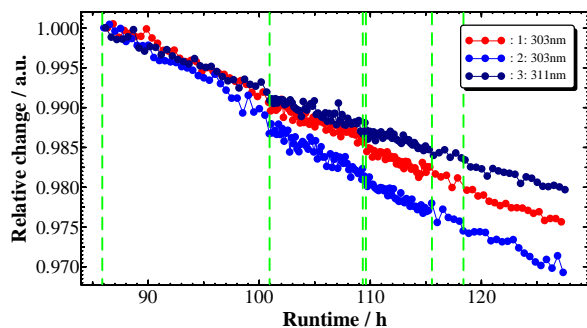


Figure 2. Relative change in the radiometric flux generated by the UV-LEDs when measured directly, without the integrating sphere.

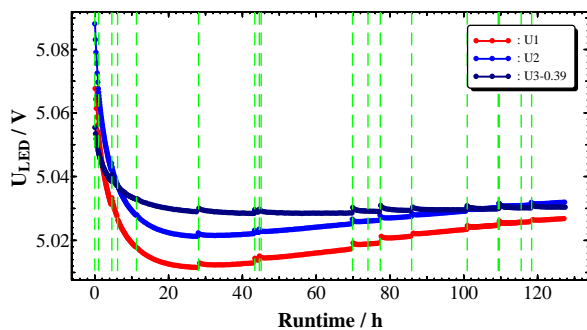


Figure 3. Voltages of the UV-LEDs recorded during the burn-in time.

Similar burn-in behavior was observed also for other UV-LED chips, except for the one with the peak nominal wavelength of 365 nm. This LED showed completely different behavior. Relative changes in the radiometric outputs of the LED chips from the third batch of LED chips studied are depicted in Figure 4. The observed drift for the 365 nm LED was much higher than expected. Also the peak wavelength of this LED showed a much higher drift as compared to those of the other chips. The spectral irradiance level of the LED was lower than expected as well. Such a different behavior can be explained by the fact that the 365 nm chip stems from a different manufacturer. The parameters of all the LED chips determined during the seasoning studies are summarized in Table 1. The data show that the spectral irradiance of the UV-LED source has reached the stability at the level of $5e-4/h$. Figure 5 depicts

spectral irradiance of the UV-LED source. Apparently, the spectrum lacks content at the wavelengths above 340 nm. Thus, additional UV-LEDs need to be included in the source.

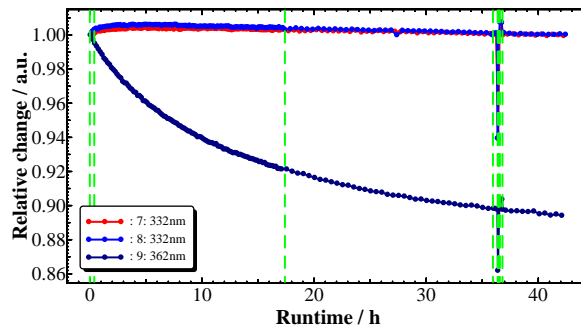


Figure 4. Relative irradiance change of three upper wavelength UV-LED chips in the device.

Table 1. Parameters of the UV-LED chips determined during the seasoning studies.

Peak wavelength (nm)	FWHM (nm)	Burn-in time (h)	Radiometric drift	Wavelength drift
303	9.1	125	$6 \times 10^{-4} / h$	$< 0.2 \text{ pm} / h$
311	9.9	125	$4 \times 10^{-4} / h$	$< 0.2 \text{ pm} / h$
319	9.6	80	$4 \times 10^{-4} / h$	$< 0.2 \text{ pm} / h$
332	8.8	45	$1 \times 10^{-4} / h$	$< 0.5 \text{ pm} / h$
364	17.7	45	$6 \times 10^{-4} / h$	$< 4 \text{ pm} / h$

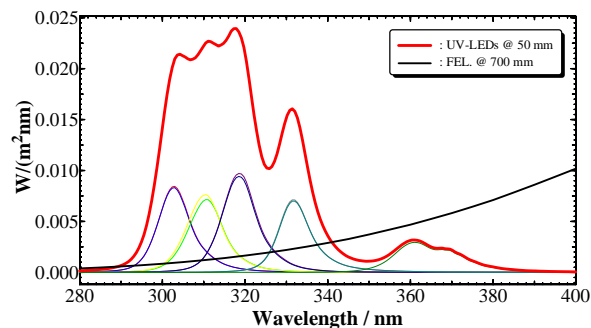


Figure 5. Spectral irradiance generated by individual UV-LED chips and all of them together at a 50 mm distance from the measurement plane. For comparison purpose, spectral irradiance of a 1000 W FEL lamp at 700 mm is shown.

At the end of the seasoning studies the stability of the UV-LED source was checked using a dedicated current driver where current for each LED is provided by a separate Supertex CL2 driver. The CL2 driver chips were selected from a large number of products to have nominal current values close to 20 mA. Figure 6 shows observed irradiance stability of the UV-LED source.

Summary and outlook

A compact reference source based on UV-LEDs is under construction in order to track radiometric stability of array spectroradiometers in application of measuring direct solar UV irradiance. The UV-LED device includes LED chips of different peak wavelengths put in a single package. Performance of the individual UV-LED chips under laboratory conditions was proved to be very good. I.e.,

stable and reproducible irradiance values were achieved after burn-in times that were even shorter than expected based on the experience gained in EMRP project ENV03 solarUV. One outcome of the seasoning studies was that PTFE-based integrating spheres obviously change under the UV-LED irradiation and are, thus, not ideal for use in the reference UV-LED source. Also temperature dependences of the PTFE-based materials may pose a stability problem. As a result a decision was taken to avoid the use of the integrating spheres in the monitor source. An alternative optical interfacing based on diffusers in order to match required irradiation conditions of spectroradiometer input optics for the direct solar irradiance measurements is being tested.

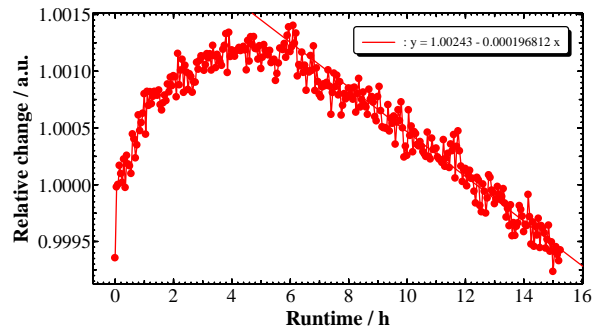


Figure 6. Irradiance stability of the UV-LED device when current for every LED is supplied by own Supertex CL2 driver chip.

Acknowledgement This work has been supported by the European Metrology Research Programme (EMRP) within the joint research project EMRP ENV59 “Traceability for atmospheric total column ozone.” The EMRP is jointly funded by the EMRP participating countries within EURAMET and the European Union.

References

1. S. Nowy, S. Nevas, M. López, M. Lindemann, A. Sperling, P. Blattner, and S. Foaleng, “Stability of light-emitting diodes in the solar UV spectral range,” *AIP Conf. Proc.* **1531**, 833 (2013). doi: 10.1063/1.4804899
2. S. Nevas, P. Sperfeld, S. Teichert, and A. Höpe, “Extraordinary changes in PTFE-based integrating-sphere properties under high levels of UV irradiation,” in *Proc. NEWRAD 2008*, 10th International Conference on New Developments and Applications in Optical Radiometry, Daejeon, 2008, pp. 333-334.

Adaptation of a Fourier Transform Spectroradiometer for outdoor measurements of the direct solar spectral irradiance

I. Kröger and S. Winter

Physikalisch-Technische Bundesanstalt, Bundesallee 100, 38116 Braunschweig

1. Introduction

A Fourier-Transform Spectroradiometer (FTS) combines the benefits of high spectral resolution (< 0.05 nm), fast measurements cycles (< 30 s) and intrinsic wavelength traceability via the internal HeNe-laser of the interferometer. The challenge is to modify such an instrument for outdoor measurements of the direct solar spectral irradiance in the range of 300 nm – 350 nm as well as the characterization and radiometric calibration of the combined instrument [1]. In this article we present the modifications of the FTS and preliminary measurements of the direct solar spectral irradiance.

2. Operation principle of the FTS

The FTS Bruker VERTEX 80 is an interferometer, illustrated simplified in Figure 1. The incident light to be measured is coupled via entrance optics onto a beamsplitter. A fraction of light passes the fixed interferometer arm, the second fraction passes the interferometer arm with the moving mirror of displacement x . Both beams are superimposed on each other and focused on a detector i.e. a photodiode. Dependent on the displacement x there is a distinctive phase shift for each wavelength of the incident light spectrum leading to an interference signal for each wavelength, i.e. photocurrent proportional to the constructive or destructive interference intensity. The superposition of all interferograms (weighted by their contribution to the overall spectral irradiance of the incident irradiation and the spectral responsivity of the detector) leads to the overall white light interferogram $I(x)$. The Fourier-Transformation of this interferogram leads to the spectrum of the incident irradiation.

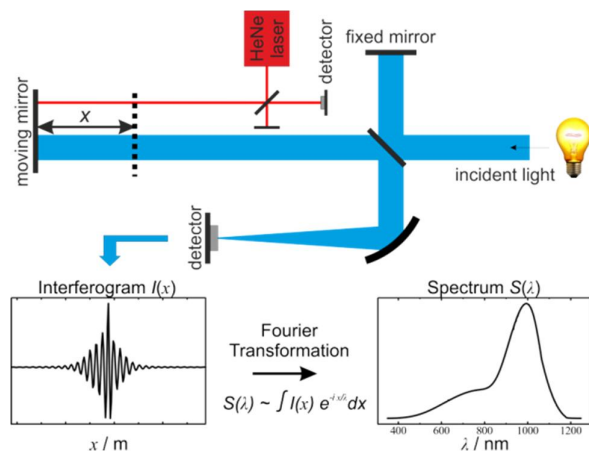


Figure 1. Simplified illustration of the operating mode of a Fourier-Transform-Spectroradiometer.

In order to achieve a correct wavelength i.e. wavenumber scale of the spectrum, the displacement x must be known very precisely. This is realized by a second interferometer and a Helium-Neon laser of known wavelength ($\lambda_{\text{HeNe}} =$

632,816 nm), using the same moving mirror. The HeNe wavelength value is recommended by the Comité international des poids et mesures (CIPM) as a realization of the SI unit metre. Since the wavelength is known, the displacement x of the moving interferometer arm can be determined traceable to the SI by measuring the interferogram of the internal HeNe-laser. As a consequence also the wavelength scale of the spectrum generated from the Fourier transformation of the interferogram is traceable to the SI-unit system. Using an external HeNe laser the wavelength uncertainty of the FTS was determined to be less than $u(\lambda_{\text{FTS}}) < 0,004$ nm ($k = 1$).

3. Modification of the FTS for outdoor measurements

There are three major modifications that have been made. At first the detector was chosen to be a GaP-diode combined with an UG11 bandpass filter limiting the responsivity to the spectral range from 250 nm to 400 nm. This reduction of spectral range avoids saturation and non-linearity effects resulting from the high solar spectral irradiance from 400 nm – 600nm. Hence a higher amplification and better signal to noise ratio (SNR) can be achieved.

Secondly a fiber optics was developed for coupling the direct solar irradiance into the FTS. A technical drawing of the tubus with a clear aperture of 50.8 mm is shown in Figure 2. The incoming light is focused by a biconvex lens with focal length $f = 200$ mm on a plane 50 mm behind the entrance of the fiber bundle of diameter of 7 mm. This enables a homogeneous illumination of the fiber bundle.

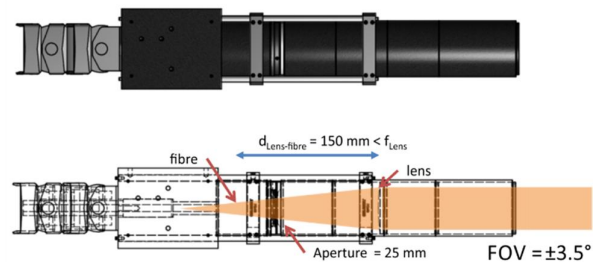


Figure 2. Technical drawing of the entrance optics.

The fiber bundle consist of approximately 1100 pure fused silica core fibers with diameter of 185 microns with a numerical aperture of 0.22 and an operating wavelength from 200 nm – 1100 nm. The fibers are randomly mixed leading to an additional homogenization at the fiber bundle exit plane that is coupled into the FTS. The field of view of this entrance optics was experimentally determined to be approximately $\pm 3.5^\circ$.

Finally a housing of the combined instrument was constructed since the FTS has to be operated outdoor. This mobile housing includes an internal cooling and ventilation system and a transfer system for the FTS.

4. Preliminary results

A relative radiometric calibration of the combined instrument was performed using a calibrated halogen standard lamp. Since the spectral irradiance of the standard lamp in the spectral range < 350 nm is extremely low leading to poor SNR this radiometric calibration is considered to be preliminary. The derived radiometric correction function is shown in Figure 3.

In order to test the combined instrument a series of measurements of the relative direct solar spectral irradiance was performed. The location was Braunschweig, Germany. The weather was a bit hazy, the sun tracking was performed provisory. The spectral resolution was set to 4 cm^{-1} (< 0.05 nm). The integration time was approximately 25 s. The results are shown exemplary in Figures 3 and 4. The comparison with a high resolution extraterrestrial spectrum [2] shows good agreement considering the spectral resolution, the position and shape of the spectral features. However a systematic wavelength shift of 0.02 nm was observed. Regarding the SNR level the noise becomes dominant below 310 nm. Higher spectral irradiance at clear sky conditions, a higher amplification range as well as averaging over more cycles might reduce this problem. However the integral contribution of this part of the spectrum below 310 nm is less than 0.5% compared the overall signal from 300 nm – 350 nm.

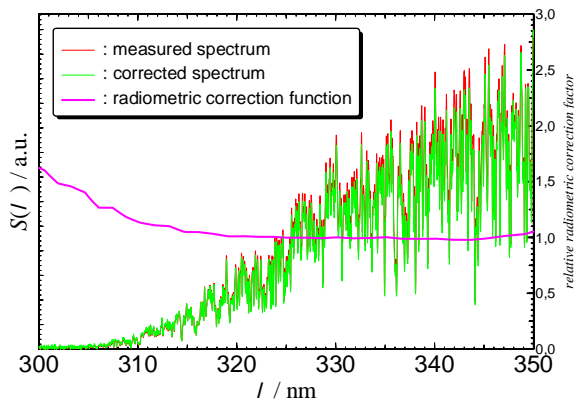


Figure 3. Relative direct solar spectral irradiance measured with the FTS.

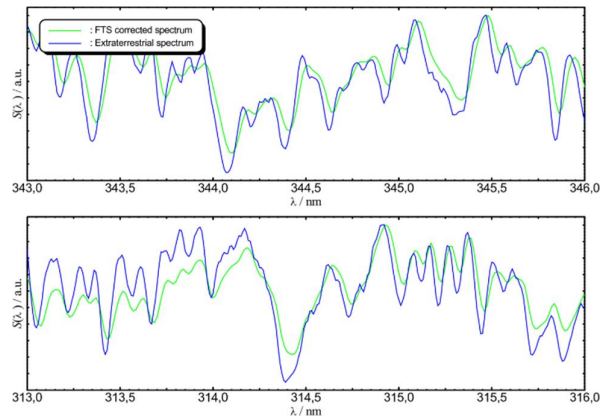


Figure 4. Detailed parts of the measured FTS spectra compared with a high resolution extraterrestrial solar spectrum [2].

5. Conclusion

A Bruker Vertex 80 Fourier Transform Spectroradiometer was adapted for performing high resolution relative direct solar spectral irradiance measurements. An entrance optic based upon a lens tubus and an optical fiber bundle was developed in order to allow the operation of the FTS in combination with a solar tracker. For the outdoor operation a movable housing with internal cooling and ventilation was built. Preliminary measurements proofed the principal ability to perform high resolution direct spectral irradiance measurements in the wavelength range from 300 nm – 350 nm with a spectral resolution of less than 0.05 nm and with reasonable measurement cycles periods less than 60 seconds.

Acknowledgement This work has been supported by the European Metrology Research Programme (EMRP) within the joint research project EMRP ENV59 “Traceability for atmospheric total column ozone.” The EMRP is jointly funded by the EMRP participating countries within EURAMET and the European Union.

6. References

- [1] P. Meindl, M. Wähler, and C. Monte, “Usability of a Fourier transform spectroradiometer for absolute surface spectral solar UV irradiance measurements,” *Optics Express* **22**, 25071-25083 (2014).
- [2] WRC PMOD, *Annual Report 2012*, p. 35 (2012).

Improvements in DOAS-derived total ozone from Phaethon

Alkiviadis Bais¹, Fani Gkertsis¹, Theano Drosoglou¹, Konstantinos Fragkos¹, and Natalia Kouremeti²

1. Aristotle University of Thessaloniki, Laboratory of Atmospheric Physics, Thessaloniki, Greece
2. Physikalisch - Meteorologisches Observatorium Davos, Switzerland

Introduction

Total ozone column (TOC) measurements are traditionally obtained from ground-based instruments since the early 1920s by Dobson and the early 1980s by Brewer spectrophotometers. Recently diode-array or CCD equipped spectrographs are being tested for their ability to provide measurements of total ozone of accuracy comparable to that of the conventional instruments, such as the Pandora system [Herman et al., 2015; Tzortziou et al., 2012] and the Phaethon system [Kouremeti et al., 2013]. The differential optical absorption spectroscopy (DOAS) technique [Platt and Stutz, 2008] has been used extensively during the last 2-3 decades to derive total, stratospheric and tropospheric columns of various trace gases, such as NO₂, SO₂, BrO, HCHO, etc. In the framework of ATMOZ, REG (AUTH) is testing the applicability of a DOAS variant to derive TOC from direct radiance spectral measurements acquired by Phaethon, without being necessary to determine and use an extraterrestrial solar spectrum. Various sensitivity tests have been made to investigate the effects of cross-section datasets and the temperature they were measured, the selection of the reference spectrum and the determination of the corresponding TOC, the spectral range used in the DOAS analysis, and the effects of other trace gases absorbing in the same spectral regions. Based on the results of these tests a standard set of settings and parameters has been established for the DOAS retrieval of TOC from Phaethon direct-sun radiance spectra. The error in the retrieved TOC reported by the DOAS analysis was found to be less than 10 DU for 90% of the data and below 5 DU for 75% of the data. These errors which increase with solar zenith angle (SZA) are still high and further attempts are made to reduce the error to less than 1% (about 3 DU).

In the following we first present briefly the Phaethon system and the DOAS analysis of TOC and then we focus on the effect of the noise-level in the measured spectra on the derived TOC. Measurements of a collocated Brewer spectrophotometer are used for the evaluation of the accuracy of the DOAS-derived TOC.

Instrumentation and data

Phaethon is a mini DOAS/max-DOAS system which consists of a cooled, miniature CCD spectrograph (AvaSpec-ULS2048LITEC) and a 2-axes tracker [Kouremeti et al., 2013]. It performs spectrally resolved measurements of direct solar irradiance and sky radiance at several elevation angles, including the zenith, in the UV-visible region (300-450nm). The total and tropospheric columns of trace gases (O₃, NO₂, HCHO, SO₂, etc.) are retrieved using the differential optical absorption technique. Phaethon operates regularly on the roof of the Physics Department building of the Aristotle University of Thessaloniki, Greece (latitude 40.634°N, longitude 22.956°E, altitude 60m) in the center of the city of Thessaloniki. At the same location a suite of others

instruments are also in operation, including two Brewer spectrophotometers.

The data of direct-sun spectral radiance used in this study have been acquired at Thessaloniki from December 2015 until February 2016. Measurements were performed continuously every about 20 min from sunrise to sunset, as long as the solar disc was not covered by clouds. Each set of measurements comprises 40 direct-sun scans acquired in about 6 min, depending on the signal level and therefore on Integration time. The integration time is adjusted automatically to achieve the highest possible signal without saturating the detector. The first 20 scans are taken through a short-pass filter that suppresses the intensity level at wavelengths longer than about 370 nm and the other 20 with the usual configuration, i.e., without the filter.

Methodology of TOC retrieval

The DOAS retrieval of the total ozone column from Phaethon is based on the estimation of the differential slant column densities (DSCD) which are derived from the analysis of direct-sun spectral radiance measurements relative to a reference spectrum.

The recorded spectra are corrected for the dark signal and stray light and are compared to a reference spectrum that has been recorded with the same instrument, to remove the absorption Fraunhofer signatures of solar irradiance and unmask the absorption signatures that are caused by atmospheric constituents. The reference spectrum has been selected to correspond to the smallest possible absorption by ozone, in order to enhance the ozone absorption signal in each of the measured spectra.

The DSCD is derived from the DOAS analysis of each of the measured spectra, using the QDOAS software (Version 2.108) developed by BIRA-IASB and S[&]T [Danckaert et al., 2013]. In the analysis, the following parameters were used:

- Spectral window: 315-337 nm
- Cross section for O₃: [Paur and Bass, 1984], 228K
- Cross section for NO₂: [A Vandaele et al., 1996], 294K
- Cross section for SO₂: [A C Vandaele et al., 1994], 294K
- Cross section for HCHO: [Meller and Moortgat, 2000], 293K
- Reference spectrum: DOY 343/2015 @ SZA 63°

If SCD_i is the slant column density of ozone at the time of the measured radiance spectrum (i), and SCD_{REF} is the slant column density of ozone at the time of the measured reference spectrum, the differential slant column density of ozone can be expressed as:

$$DSCD_i = SCD_i - SCD_{REF} = TOC_i \times AMF_i - SCD_{REF} \quad (1)$$

where AMF_i is the airmass factor. It corresponds to the enhancement of the radiation path through mainly the stratospheric ozone layer where most of the ozone absorption occurs. For SZAs smaller than about 75° it is approximated by the secant of the SZA at the altitude of ~ 22 km, for mid-latitude locations.

The SCD_{REF} , can be derived from (1) by applying a Langley extrapolation to the $DSCD_i$ against AMF_i , during periods with fairly constant TOC so that (1) is linear. Alternatively, the SCD_{REF} can be derived from a collocated instrument measuring the TOC_{REF} , as in our case the Brewer spectrophotometer #005. Note that for the same instrument the reference spectrum can be measured once and used repeatedly, irrespective of location. Once the SCD_{REF} is known, (1) can be rewritten to derive the TOC from each measured direct radiance spectrum:

$$TOC_i = \frac{DSCD_i + SCD_{REF}}{AMF_i} \quad (2)$$

The overall error in the TOC estimation, σ_{TOC} , can be derived by propagating the errors of the individual terms of (2), yielding:

$$s_{TOC_i} = \frac{\sqrt{s_{DSCD_i}^2 + s_{SCD_{REF}}^2}}{AMF} \quad (3)$$

In (3) the error in the calculation of AMF is assumed negligible, the error of the $DSCD$ is provided by the $QDOAS$ analysis software, while the error of the SCD_{REF} is the uncertainty of the Brewer derived TOC_{REF} , usually less than 2.5 DU.

Discussion and Results

Until recently the spectral measurements recorded by Phaethon have been covering the entire spectral range of the spectrograph, the highest wavelength being 452 nm, while for the retrieval of TOC only the measurements between 315 and 337 nm are used in the DOAS analysis. This was necessary since Phaethon is used also for deriving the NO_2 column, which is retrieved at the long-wavelength region (400-450 nm). Since the dynamic range of the CCD is 16 bit (equivalent to about 64000 counts) to avoid damage from overexposure the integration time is adjusted accordingly so that the maximum count-rate stays below about 60 000 counts throughout the operational spectral range. The adjustment is based on the highest intensity which usually occurs towards the end of the spectral region (between 440 and 450 nm). As the intensity increases rapidly with wavelength in the UVA region, at the ozone retrieval range the signal is very low and at large SZAs often comparable to the dark signal. Consequently the spectra that have been used so far for the retrieval of TOC have very low signal and are highly uncertain. Since late November 2015, a short-pass filter has been installed in the filter-wheel of the fore optics allowing the acquisition of a second set of spectra with diminished intensity at wavelengths longer than 370 nm. This caused the peak intensity to move to shorter wavelengths allowing higher integration times and much stronger signal at the ozone retrieval range. An example is shown in Figure 1, where

the two spectra recorded one after the other, with and without the short-pass filter, are shown. Evidently, in the spectral range 315-337 nm the peak intensity of the spectrum taken with the short-pass filter is at least 4 times higher than without the filter.

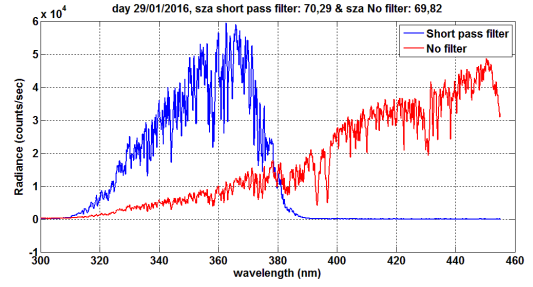


Figure 1. Example of direct-sun spectral radiance measurements recorded by Phaethon with (blue) and without (red) the short-pass filter.

The spectra from both subsets (with and without the short-pass filter) were used to retrieve the TOC with $QDOAS$, and the quality of the retrieval was evaluated by analyzing the retrieval error, as well as by comparing the derived TOC with that derived by the Brewer. The frequency distribution of the retrieval error reported by $QDOAS$ for the two subsets during the period December 2015-February 2016 is shown in Figure 2. The increase in the number of data with smaller errors is obvious when the filter is used; 80% of the data have errors below 3 DU compared to 40% for the spectra taken without the filter.

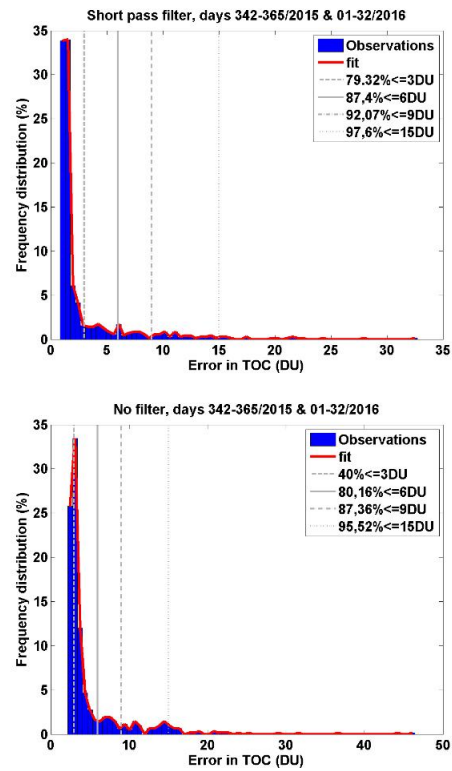


Figure 2. Frequency distribution of errors in TOC retrieval as reported by the $QDOAS$ analysis of spectra recorded with (top) and without (bottom) the short-pass filter. The red line is a smoothing function fit and the vertical lines mark the percentage of data with error smaller than 3, 6, 9 and 15 DU.

Thematic Network for Ultraviolet Measurements

Whether the improvement of the retrieval error has affected the absolute values of the derived *TOC* has been assessed by comparison with the corresponding Brewer-derived *TOC*. Figure 3 shows the scatter plots between the *TOC* values of the two systems with and without the short-pass filter in Phaethon. As the two instruments have different operation protocols, the data are not exactly coincident, so for the comparisons only data recorded within one hour have been used.

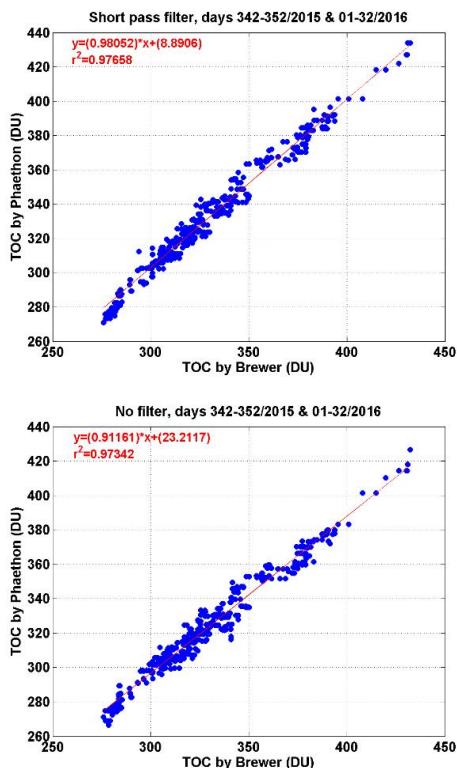


Figure 3. Scatter plot of Phaethon- and Brewer-derived *TOC* based on spectra recorded through the short-pass filter (top) and without the filter (bottom).

From a first look the two scatter plots are very similar with slight differences only in the statistical estimates. The correlation coefficient is practically the same, but the slope of the regression is closer to unit (0.98) for the Phaethon data with the filter compared to 0.91 for the data without the filter. Moreover, in the first case the offset term is smaller (about 9 DU compared to 23 DU). These results suggest an improvement in the *TOC* derived from the dataset with the short-pass filter, which mainly arises from the increase of the signal to noise ratio in the measured radiances. This is also confirmed by the percentage differences in *TOC* between Phaethon and Brewer for the two subsets of data (Figure 4). The mean absolute difference is $0.76 \pm 1.5\%$ when the short-pass filter is used, increasing to $-1.13 \pm 1.5\%$ without the filter.

The frequency distribution of errors shown in Figure 2, have been derived from all data recorded by Phaethon. Considering only the data used for the comparisons with the Brewer, the peak of the distribution moves to smaller errors, as shown in Figure 5. For the data set with the short-pass filter practically all data have errors below 3 DU (about 1% of *TOC*) while more than 95% of the data have errors even below 1.5 DU (about 0.5% of *TOC*).

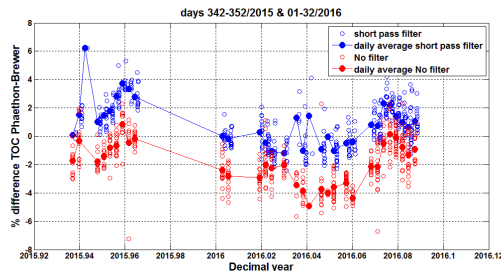


Figure 4. Percentage differences in *TOC* derived from Phaethon spectra recorded through the short-pass filter (blue) and without the filter (red) relative to Brewer-derived *TOC* for the period December 2015 - February 2016. The filled symbols correspond to daily averages.

Furthermore, we investigated whether there is any *SZA* dependence in the *TOC* ratio from Phaethon and Brewer. The range of *SZA* variation in the available dataset is very narrow (58° - 74°), since the data were collected during the winter season, and the variability of the ratio is quite high at such large *SZAs*. Therefore no firm conclusions can be derived, but there are indications that the ratio decreases slightly with increasing *SZA* for the dataset acquired without the short-pass filter. This should be confirmed as more data are collected at smaller *SZAs* during spring and summer 2016. Finally, a similar test for the dependence on the *TOC* amount revealed no dependence in both datasets.

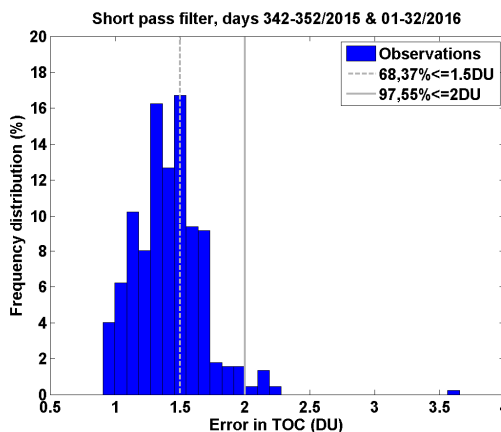


Figure 5. Frequency distribution of errors in *TOC* retrieval as reported by the QDOAS analysis of spectra recorded with the short pass filter, only for the dataset used in the comparisons with the Brewer. The vertical lines mark the percentage of data with errors below 1.5 and 2 DU.

Conclusions

The use of a short-pass filter in the measured direct-sun radiance spectra by Phaethon suppresses the higher intensities of solar radiation a wavelengths longer than 370 nm, allowing the use of higher integration times in the recorded spectra. This modification lead to increased signal to noise ratio and a remarkable reduction of the retrieval error in the differential slant column density of ozone, so that 80% of the total ozone data have errors below 3 DU (about 1%), compared to 40% for the data recorded without the filter. The improvement has mainly affected the data taken at large solar zenith angles.

Comparison of *TOC* derived from Phaethon and the collocated Brewer #005 for December 2015-February 2016 (with largest *SZA* 58°) revealed an agreement of $0.75 \pm 1.5\%$ when the short-pass filter is used, slightly better than for data recorded without the filter ($-1.15 \pm 1.5\%$). It is expected that during seasons with smaller *SZAs* and better weather conditions the agreement would be even better. For the data used in the comparisons with the Brewer the retrieval error is further reduced so that 98% of the data have errors below 2 DU.

Finally, the short-pass filter may have served also to reduce the effect of the far-field stray-light from longer wavelengths as it suppresses the signal at these wavelengths. However, this has not been proven so far.

Acknowledgement This work has been supported by the European Metrology Research Programme (EMRP) within the joint research project EMRP ENV59 "Traceability for atmospheric total column ozone." The EMRP is jointly funded by the EMRP participating countries within EURAMET and the European Union.

References

- Danckaert, T., C. Fayt, M. v. Roozendael, I. d. Smedt, V. Letocart, A. Merlaud, and G. Pinardi, *QDOAS Software user manual Rep.*, 117 pp, BIRA-IASB and S[&]T, (2013). <http://uv-vis.aeronomie.be/software/QDOAS>
- Herman, J., R. Evans, A. Cede, N. Abuhassan, I. Petropavlovskikh, and G. McConville, "Comparison of ozone retrievals from the Pandora spectrometer system and Dobson spectrophotometer in Boulder, Colorado," *Atmos. Meas. Tech.* **8**, 3407-3418 (2015).
- Kouremeti, N., A. F. Bais, D. Balis, and I. Zyrichidou, "Phaethon: A System for the Validation of Satellite Derived Atmospheric Columns of Trace Gases," in *Advances in Meteorology, Climatology and Atmospheric Physics*, edited by C. G. Helmis and P. T. Nastos, pp. 1081-1088, Springer Berlin Heidelberg (2013).
- Meller, R., and G. K. Moortgat, "Temperature dependence of the absorption cross sections of formaldehyde between 223 and 323 K in the wavelength range 225-375 nm," *J. Geophys. Res.* **105**, 7089-7101 (2000).
- Paur, R. J., and A. M. Bass, "The ultraviolet cross-sections of ozone: II. results and temperature dependence," Ozone Symposium, Chalkidiki, 611-616 (1984).
- Platt, U., and J. Stutz, *Differential optical absorption spectroscopy. Principles and Applications*, Springer-Verlag, Berlin Heidelberg (2008).
- Tzortziou, M., J. R. Herman, A. Cede, and N. Abuhassan, "High precision, absolute total column ozone measurements from the Pandora spectrometer system: Comparisons with data from a Brewer double monochromator and Aura OMI," *J. Geophys. Res.* **117**, D16303 (2012).
- Vandaele, A., C. Hermans, P. Simon, M. Van Roozendael, J. Guilmot, M. Carleer, and R. Colin, "Fourier transform measurement of NO₂ absorption cross-section in the visible range at room temperature," *J. Atmos. Chem.* **25**, 289-305 (1996).
- Vandaele, A. C., P. C. Simon, J. M. Guilmot, M. Carleer, and R. Colin, "SO₂ absorption cross-section measurement in the UV using a fourier transform spectrometer," *J. Geophys. Res.* **99**, 25599-25606 (1994).

A simulation-tool to model ozone retrieval uncertainties of Brewer and Dobsons instruments

Luca Egli¹, Julian Gröbner¹, Ulf Köhler², Alberto Redondas³, Virgilio Carreño³, and Henri Diemmoz⁴

1. Physikalisches-Meteorologisches Observatorium Davos, World Radiation Center, PMOD/WRC, Davos Dorf, Switzerland
2. Deutscher Wetterdienst (DWD), Hohenpeissenberg, Germany
3. Izaña Atmospheric Research Center, AEMET, Tenerife, Canary Islands, Spain
4. ARPA Valle d'Aosta, Saint-Christophe, Italy

Introduction

The depletion of the stratospheric ozone layer is reported in many international scientific publications since the 1970s (e.g. [1], [2]). As the ozone layer absorbs the UV radiation in the atmosphere, the total of stratospheric ozone is crucial for the incoming UV radiation at earth surface and its impact on human health [3]. This strong absorption in the UV band allows retrieving the total ozone column (TOC) at the earth surface by measuring the UV radiation from direct sun measurements. In order to monitor the aforementioned depletion of stratospheric ozone and its impact on the UV exposure on the ground, initially Dobson instruments (e.g. [4]) were installed to establish a worldwide network. These Dobson instruments were operated manually and required substantial manpower and maintenance.

In the 1980s the Brewer spectrometer [5], was introduced as an automatic device measuring direct solar UV radiation with state of the art technology using gratings instead of prism. The Brewers also allowed measuring absolute intensities displaying advantages to the Dobson instruments. Both instruments were installed to observe TOC at different places worldwide and are simultaneously operated in networks until now.

Several work addressed the comparison between the Dobson network and the Brewer network (e.g. [6],[7]). Even though both instruments are measuring in the UV band between 305 nm and 340 nm and the TOC retrieval are based on the same principle, there are biases and seasonal dependency observed when comparing both instruments ([8]) displaying fundamental uncertainties in estimating TOC.

The EMRP-ENV59 project ATMOZ – “Traceability for atmospheric total column ozone” aims to thoroughly determine the sources of uncertainties in of TOC retrieval using different instruments such as the Dobsons or Brewers, but also as array spectroradiometers. The first step within the project is to characterize and calibrate the Dobsons and Brewer instruments to assess the sources of uncertainty originating from the UV measurements. Another workpackage of the project additionally aims to produce a comprehensive uncertainty budget for ground based TOC retrieval including the retrieval method from Dobsons, Brewers and array spectroradiometer.

This letter presents a software-tool to model the sources of uncertainty from the standard Dobson and Brewer retrieval method. As a first example of the overall uncertainty budget, the software estimate with Monte Carlo ensemble runs the impact of uncertainties of the major parameters affecting the ozone estimation such as instruments

characteristics (wavelength shift), different ozone cross-sections and temperatures of the stratospheric ozone layer. The software is one step for the comprehensive uncertainty budget which will be finalized by the end of the project.

Data and Method

1. Input spectra

In order to understand the sources of different uncertainties using the retrieval of Dobsons and Brewers, only modelled solar UV spectra were used instead of real data. The spectra were generated with a simple atmosphere attenuation model implemented in “Matlab” environment based on the Beer-Lamberts law

$$I_{\lambda} = I_{\lambda}^0 e^{-\tau_{\lambda} m}, \quad (1)$$

where I_{λ}^0 is the extraterrestrial spectrum generated during the previous EMRP-ENV03 project “Solar UV” (see: http://www.pmodwrc.ch/annual_report/annualreport2012.pdf, page 35) and $\tau_{\lambda} m$ is the atmospheric absorption term.

Expanding $\tau_{\lambda} m$ and rewriting Equation (1) we obtain

$$\log I_{\lambda} = \log I_{\lambda}^0 - \tau_{\lambda}^R m_R - \tau_{\lambda}^{O_3} m_{O_3} - \tau_{\lambda}^{aod} m_{aod} \quad (2)$$

where m_R, m_{O_3}, m_{aod} are different air-masses due to different respective heights of the ozone air and particle molecules within the atmospheric profiles. These different air-masses are determined by a “Matlab” algorithm calculating the air-masses based in the geographical parameters such as location of the station and time of measurements. Our modelled spectra were generated at the same location, the same day of the year at 7 different times of these days exhibiting 7 different air-masses. The absorption terms τ_{λ}^R and τ_{λ}^{aod} were also kept constant for all generated spectra, by using a parametrization of these parameters. Contrary, the absorption term for the ozone layer $\tau_{\lambda}^{O_3}$ was based on two different absorption cross-sections:

1. Bass and Paur (BP), which is the official and generally used cross-section for the brewer retrieval [8]. For the temperature interpolation the set with quadratic coefficient is used (http://igaco-o3.fmi.fi/ACSO/files/cross_sections/Bass-Paur/bp.par)
2. The new cross-section by the university of Bremen (“Bremen”, [8]), which displays an alternative data set to generate modelled spectrum (http://igaco-o3.fmi.fi/ACSO/files/cross_sections/Serdyuchenko/SerdyuchenkoGorshchev5digits.dat). The dataset was interpolates for the temperatures between all measured

cross-section spectra for the temperatures from 193°K to 293°K by a linear fit.

The spectra can be generated by assuming different values for the stratospheric ozone temperature. The default value is -45°C. However, to investigate the sensitivity of the ozone retrieval, the atmospheric temperature was varied between -80°C and -30° C (see results).

In summary: the main variables for the model calculations were the total column ozone (TOC) and the air-mass m_{O_3} . A total of 49 (= 7 TOC x 7 m_{O_3}) spectra were computed over the wavelength range between 300 nm to 360 nm for the TOC range from 200 to 500 DU and air-mass m_{O_3} range between 1 and 4.

It should be highlighted, that since the retrieval method strongly depends on the full width half maximum (FWHM) and the spectral resolution of the generated spectrum, both parameters were chosen to be similar as the extraterrestrial spectrum. Namely, the FWHM of the generated spectrum was 0.01 nm and the resolution was 0.01 nm. This means that the input spectrum was not convolved with the instruments slits after the attenuation of the extraterrestrial spectrum. The input spectrum was homogenized as a last step of the generation procedure by a convolution with a triangular slit of 0.01 nm FWHM.

2. Ozone retrieval

The retrieval of the ozone from Dobson and Brewer instruments are based on the same principle. Basically, 4 wavelengths in the UV band are measured to derive the ozone by calculating the ratio between these wavelengths. The retrieval algorithms are fully described e.g. in [4], [5] and [7].

To summarize the Dobson and Brewer retrieval method, Equation (2) can be written for each of the 4 wavelength to:

$$\log I_i = \log I_i^0 - \tau_i^R m_R - \alpha_i^{O_3} X m_{O_3} - \beta_i^{SO_2} Y m_{SO_2} - \tau_i^{aod} m_{aod} \quad (3)$$

while i indexes the different wavelengths at the Brewer or the Dobson instrument, respectively (Table 1).

Table 1. Center wavelength of the different slits at Dobsons and Brewers.

i (Slit)	1	2	3	4
/-Brewer (nm)	310.1	313.5	316.8	320
/-Dobson (nm)	305.51	317.62	325.08	339.97

Combining all four wavelengths, the so called “weighted ratio” or “double ratio” technique is applied according to

$$F = F_0 - \Delta\tau^R m_R - \Delta\alpha^{O_3} X m_{O_3} - \Delta\tau^{aod} m_{aod} \quad (4)$$

where $\Delta\tau^R = \sum_i W_i \tau_i^R$; $\Delta\alpha^{O_3} = \sum_i W_i \alpha_i^{O_3}$, and the four wavelength are weighted differently for Dobson and Brewer:

$W_i(\text{Dobsons})=(+1,-1,+1,-1)$ and $W_i(\text{Brewers})=(+1,-0.5,-2.2,+1.7)$, with $\sum_i W_i = 0$.

The weights are chosen so that $\Delta\tau^{aod}$ becomes negligible assuming that $\Delta\tau^{aod}$ varies slowly with wavelength.

$$\Delta\tau^{aod} = \sum_i W_i \tau_i^{aod} \approx 0 \quad (5)$$

Then, Equation (4) becomes

$$F = F_0 - \Delta\tau^R m_R - \Delta\alpha^{O_3} X m_{O_3} \quad (6)$$

and the total ozone column (TOC) is obtained as

$$TOC = X = \frac{F_0 - F - \Delta\tau^R m_R}{\Delta\alpha^{O_3} m_{O_3}} \quad (7)$$

The retrieval method mentioned above is implemented in a “Matlab” routine with following slit functions at the respective wavelengths (see Table 1) for:

1. the Brewer #185 from the RBCC-E triad installed at the Izaña Atmospheric research center in Tenerife, Spain, using a parametrization of the slit function with known FWHM.
2. the Dobson 064, which is the regional Dobson reference at Hohenpeissenberg in Germany. This slit functions were recently measured during the ATMOZ project with tuneable laser facilities at PTB in Braunschweig Germany (see http://projects.pmodwrc.ch/atmoz/images/Presentation_s_web/symposium_2/1_Symposium_2.pdf).

The extraterrestrial spectrum (F_0) was the same as used for the generation of the spectrum as well as the molecule scattering $\Delta\tau^R m_R$, which was parametrized according to Nicolet [9]. The absorption cross-section $\Delta\alpha^{O_3}$ was either Bass and Paur (PB) or “Bremen” [8] at the stratospheric temperature of -45°C.

To computationally calculate the quantities $F_0, F, \Delta\tau^R m_R$ and $\Delta\alpha^{O_3}$, the integral of the respective spectral quantities over the slit function at each wavelength is calculated and weighted with the corresponding weights for Dobson and Brewer.

Results and Discussions

1. Evaluation of the two retrieval method

The retrieval method described above is evaluated by comparing the ratios of the known TOC, which is used as an input variable to generate the spectrum and the TOC derived from the retrieval, either for the Brewer and the Dobson wavelengths. Figure 1 shows the ratios between the true and the retrieval for the different air-masses and total column ozone, for 1a) the Dobson wavelengths and 1 b) Brewer wavelengths.

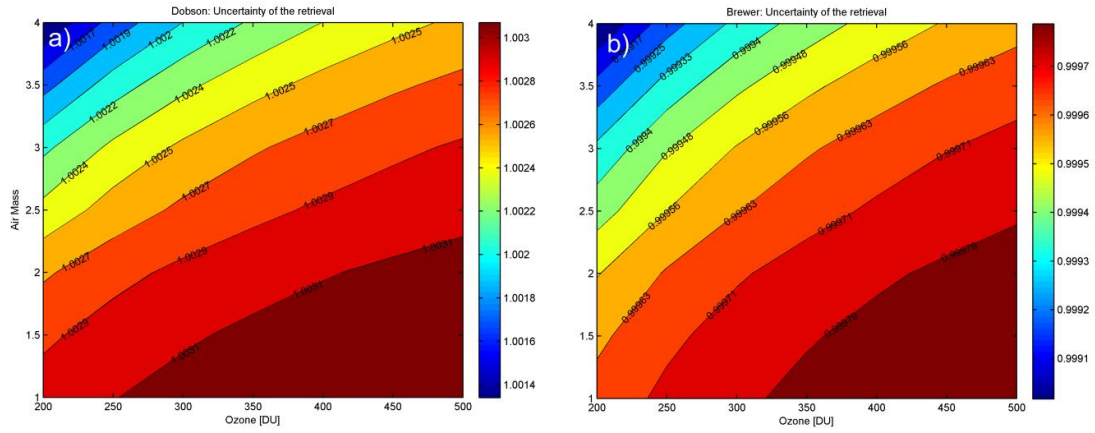


Figure 1 a-b: Ratios of the input TOC and the TOC from the retrieval for different air-masses and ozone for a) Dobson and b) Brewer simulation.

The legend in the subfigures of figure 1 shows that the agreement between the known ozone value and the retrieved TOC is generally less than 0.01 % for the Brewer and Brewer retrieval. A typical spectrum from array spectroradiometer exhibits a FWHM of about 0.5 nm and a spectral sampling rate of about 0.2 nm. Contrary to the standard input spectrum (FWHM=0.01 nm with 0.01 nm sampling rate), the generated spectrum was convolved with a triangular slit of 0.5 nm FWHM and a sampling rate of 0.2 nm to simulate the measurement of an array spectroradiometer. Applying the method describes above to this low resolution spectrum, the retrieval of ozone deviates significantly from the input TOC. Figure 2 a) and b) shows that these biases range between 0.5% and 0.7% using the Dobson wavelength, which is similar as the retrievals using a high resolution spectrum (Figure 1 a). The Brewer retrieval shows deviations between -4% and -6%. These uncertainties are too large for an operational retrieval of TOC based on array spectroradiometer data. However, since the deviations are systematic and mainly more depending on the air-mass than on the ozone, the retrieval can be calibrated by a Langley-plot calibration determining an extraterrestrial constant F_0 specifically for the array spectroradiometer used for the retrieval.

One may use measured spectra from e.g. array spectroradiometer to retrieve ozone by using the Dobson and Brewer retrieval. A typical spectrum from array spectroradiometer exhibits a FWHM of about 0.5 nm and a spectral sampling rate of about 0.2 nm. Contrary to the standard input spectrum (FWHM=0.01 nm with 0.01 nm sampling rate), the generated spectrum was convolved with a triangular slit of 0.5 nm FWHM and a sampling rate of 0.2 nm to simulate the measurement of an array spectroradiometer. Applying the method describes above to this low resolution spectrum, the retrieval of ozone deviates significantly from the input TOC. Figure 2 a) and b) shows that these biases range between 0.5% and 0.7% using the Dobson wavelength, which is similar as the retrievals using a high resolution spectrum (Figure 1 a). The Brewer retrieval shows deviations between -4% and -6%. These uncertainties are too large for an operational retrieval of TOC based on array spectroradiometer data. However, since the deviations are systematic and mainly more depending on the air-mass than on the ozone, the retrieval can be calibrated by a Langley-plot calibration determining an extraterrestrial constant F_0 specifically for the array spectroradiometer used for the retrieval.

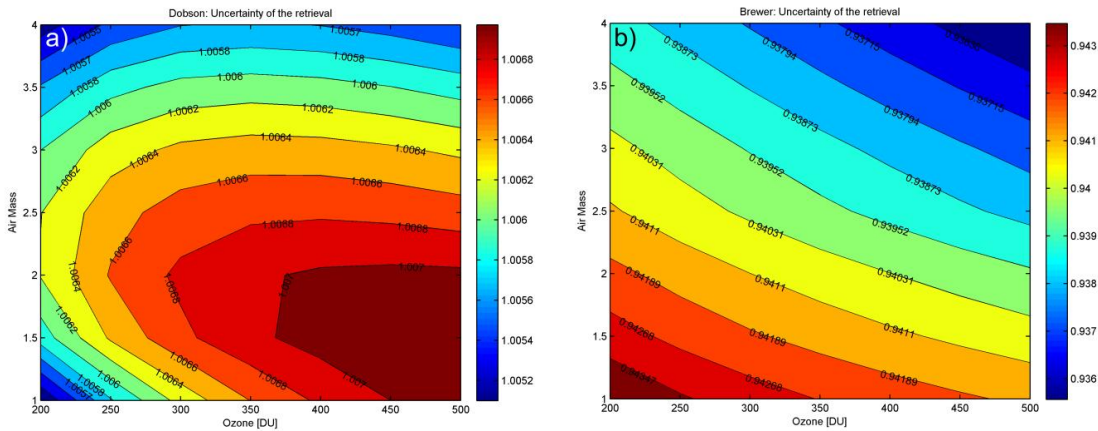


Figure 2 a-b: Ratios of the input TOC and the TOC from the retrieval, when using an input spectrum with a FWHM of 0.5 nm and a spectral resolution of 0.2 nm as for typical array spectroradiometer. The rations are shown for different air-masses and ozone for a) Dobson and b) Brewer simulation.

2. Variation of the input spectrum

The software tool described above allows now investigating the impact of the different sources of uncertainty from either

- a) Measurements provided by the Dobson or Brewer instruments or
- b) Uncertainties of the retrieval model,

on the overall uncertainty to determine TOC.

As a first example, the impact of the uncertainty in wavelength determination of the instrument is analyzed. Second the influence of the unknown stratospheric ozone temperature, when using the predefined retrieval temperature of -45° , is investigated

a) Wavelength uncertainty

Spectroradiometer inherently exhibit an uncertainty in determining the exact wavelength of the measurement. The wavelength uncertainty of the center wavelength at the Dobson instruments can be quantified to be around 0.025 nm

(<http://www.esrl.noaa.gov/gmd/ozwv/dobson/papers/report13/5th.html>). Since the wavelength of the Brewers are calibrated during operation with an internal Hg lamp by adjusting the gratings with a step-motor, the center wavelength uncertainty of the Brewers is at least half a step or $0.0075/2 \text{ nm} = 0.0035 \text{ nm}$ [11]. This is the minimal

wavelength shift. However, the shift may be larger when considering other effects.

In order to investigate the uncertainty of the derived TOC as a function of the mentioned instrument uncertainties, the entire modelled input spectrum is shifted by a randomly selected wavelength shift. The random wavelength shift if taken from a Gaussian distribution with a standard deviation of the corresponding instrument (i.e. 0.025 nm for Dobson and 0.0035 nm for Brewer). The so modified spectrum is then used for the standard retrieval. This procedure was repeated 500 times with a new randomly selected wavelength shift for each of the 500 retrieval-runs. The ratio between the input TOC to generate the spectrum and the resulting TOC are calculated for each run and for all spectra with the 49 different atmospheric conditions. The average of all these ratios and the corresponding standard deviation is then calculated over all runs. The mean indicate a systematic deviation and the standard deviation displays overall uncertainty caused by the wavelength-shift. Figure 3 a) and b) shows the overall uncertainty, i.e. the standard deviation of the ratios from all 500 runs. The results reveal that for both instruments the uncertainty caused by the instrument's wavelength shift is generally higher at low ozone concentrations and low air-mass. At these atmospheric conditions the Dobson and the Brewer retrieval shows an uncertainty of less than 0.5%, which is the maximum uncertainty found. Remarkably, the uncertainties are comparable for both instruments.

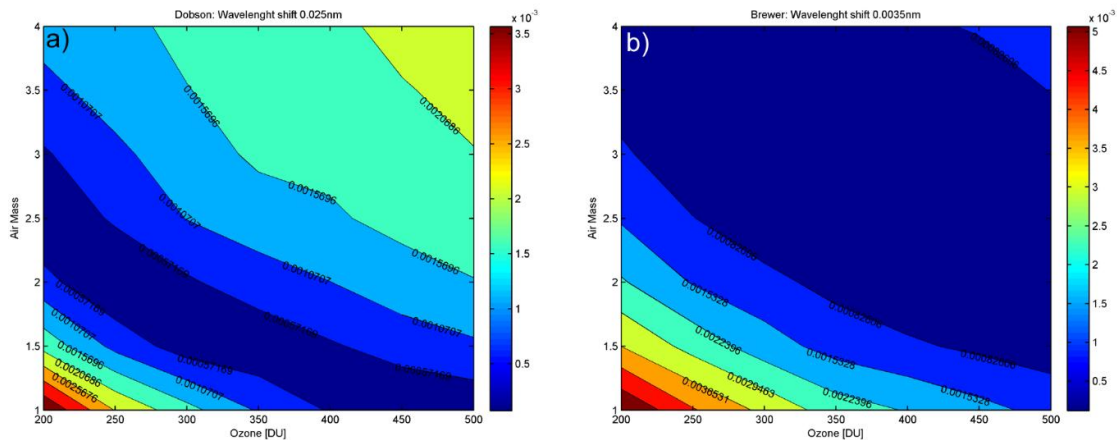


Figure 3 a-b: Ratios of the input TOC and the TOC from the retrieval, when varying the wavelength of the input spectra. The numbers indicate the standard deviation of 500 realizations of ozone retrieval based on the modified spectrum.

b) Uncertainty of the stratospheric temperature

As mentioned above, the retrieval of the TOC assumes that the stratospheric temperature is constant at -45°C . This temperature is taken to calculate the absorption cross-section $\Delta\alpha^{O_3}$. However, the real atmospheric temperature of the ozone layer in the stratosphere is unknown. The impact of this source of the retrieval model uncertainty on the overall uncertainty determining TOC is investigated by generating different input spectrum with different atmospheric temperatures ranging from -30°C to -80°C . Please note that the temperature of the retrieval method is kept to be -45° as for the standard retrieval. Similar as for the wavelength uncertainty, the spectra were generated with a random selection of the atmospheric temperature for each spectrum at the 49 different atmospheric conditions in

terms of air-mass and TOC. Again, this procedure was repeated 500 times in order to calculate the mean and the standard deviation of all these possible realizations. In additions, the retrieval was performed using two different cross sections: 1. Bass Paur and 2. "Bremen" [8].

Figure 4 a) - c) shows all representations of the different runs (grey line) with the mean (redline) and +/- half of the standard deviation from the mean value (dashed red line). The spectrum number indicates the spectra at a specific atmospheric conditions in terms of air-mass and ozone. For example spectrum number 1 is at air-mass 1.0 and ozone 200 DU and spectrum number 49 at air-mass 4.0 and 500 DU. Remarkably, there is no dependence on the atmospheric conditions for all 4 scenarios. However it is evident, that the Dobson retrieval (Figure 4 a-b) is more

Thematic Network for Ultraviolet Measurements

sensitive to unknown stratospheric temperature than the Brewer retrieval (Figure 4 c-d). This result is in line with previous studies, addressing the differences of the cross-section on the final TOC result [8]. The mean value of the Dobson is between 0.5% and 1% (Figure 4 a - b), while the Brewer can show a systematic bias of up to 1.1 % (Figure 4 d). These systematic biases originate from the asymmetric variation of temperature between -80°C to -

30°C while the retrieval is at -45°C . The lowest uncertainty is shown for the Brewer when using the “Bremen” cross-section, with an overall deviation from the mean value of about 0.5 %. Remarkably, there is no systematic bias, indicating that the Brewer retrieval using “Bremen” is stable regarding variation of the stratospheric temperature.

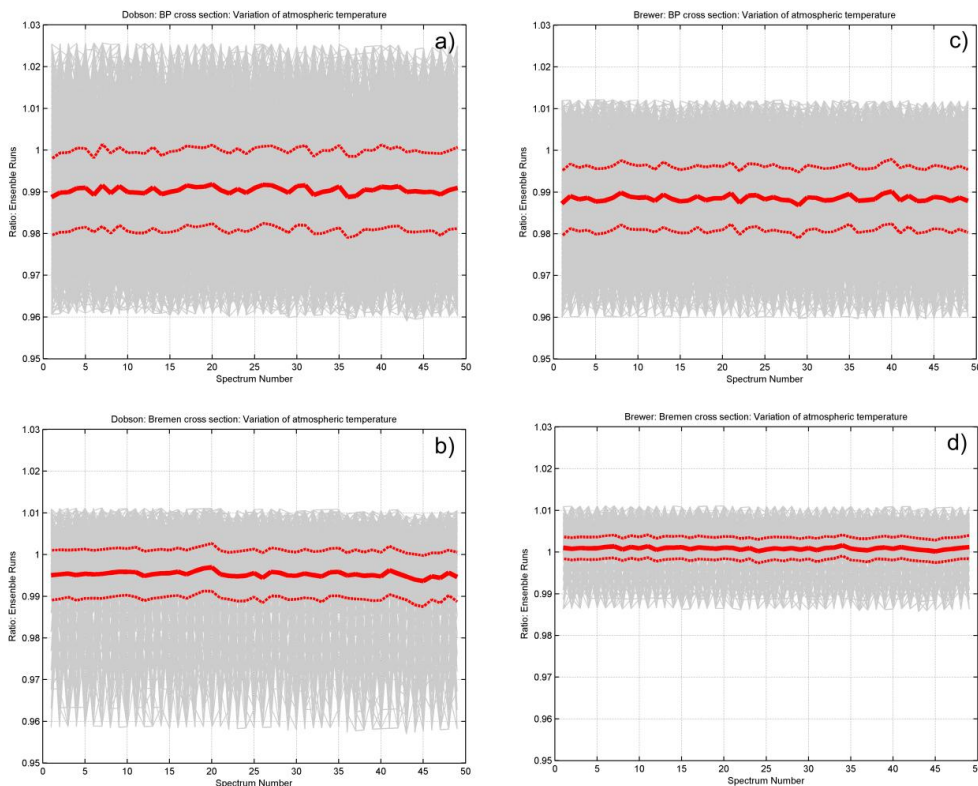


Figure 4 a-d: Ratios of 500 ensemble runs of TOC retrieval with variation of the stratospheric temperature between -80°C and -30°C . The grey line indicates the ratio of one TOC retrieval to the input TOC. The red line indicated the mean over all 500 realizations and the dashed red line presents the deviation from the mean (\pm half standard deviation). The ensemble runs were performed for two different cross-sections: Bass-Paur and “Bremen”.

Conclusions

This letter presented a software-tool to estimate the impact of different sources of uncertainty for the ozone retrieval with Dobson and Brewer instruments.

It was shown that in the ideal case of modelled input spectra, the Brewer retrieval is able to determine total ozone column (TOC) with less than 0.01%. The Dobson retrieval shows a larger deviation of up to 0.3%.

The software allows now simulate different sources of uncertainty originating either from the measurement uncertainty or uncertainties of the retrieval model assumptions and therefore to investigate the impact of these sources to the overall uncertainty of TOC determination.

The first results towards a comprehensive uncertainty budget showed that the wavelength uncertainties lead to overall TOC uncertainties of less than 0.5% for both retrievals. The uncertainty caused by the unknown stratospheric temperature depends on the used cross-section and ranges from 0.5% for Brewers with the

“Bremen” cross-section up to 2% for the Dobson, when using the Bass-Paur cross section.

The sensitivity of other sources of uncertainty can now be further investigated using the software.

Acknowledgement This work has been supported by the European Metrology Research Programme (EMRP) within the joint research project EMRP ENV59 “Traceability for atmospheric total column ozone.” The EMRP is jointly funded by the EMRP participating countries within EURAMET and the European Union.

References

- [1] Molina, M. J., and F. S. Rowland, “Stratospheric sink for chlorofluoromethanes-Chlorine atom catalyzed destruction of ozone,” *Nature* **249**, 810– 812 (1974).
- [2] Staehelin, J., N. Harris, C. Appenzeler, and J. Eberhard, “Ozone trend: A review,” *Rev. Geophys.* **39**, 231– 290 (2001).
- [3] Zerefos, C. S., “Long-term ozone and UV variations at Thessaloniki, Greece,” *Phys. Chem. Earth A/B/C* **27**, 455– 460 (2002). doi: 10.1016/S1474-7065(02)00026-8

- [4] Vanier, J., and I. Wardle, "The effects of spectral resolution on total ozone measurements," *Q. J. R. Meteorol. Soc.* **95**, 395–399 (1969).
- [5] Kerr, J. B., "New methodology for deriving total ozone and other atmospheric variables from Brewer spectrophotometer direct Sun spectra," *J. Geophys. Res.* **107**, 4731 (2002). doi:10.1029/2001JD001227
- [6] World Meteorological Organization (WMO), *Comparison of total ozone measurements of Dobson and Brewer spectrophotometers and recommended transfer function, Global Ozone Res. Monit. Proj. Rep.* **149**, Geneva, Switzerland, 2003.
- [7] Scarnato, B., J. Staehelin, T. Peter, J. Gröbner, and R. Stübi, "Temperature and slant path effects in Dobson and Brewer total ozone measurements," *J. Geophys. Res.* **114**, D24303 (2009). doi:10.1029/2009JD012349
- [8] Redondas, A., Evans, R., Stuebi, R., Köhler, U. and Weber, M., "Evaluation of the use of five laboratory-determined ozone absorption cross sections in Brewer and Dobson retrieval algorithms," *Atmos.Chem. Phys.* **14**, 1635–1648 (2014). doi:10.5194/acp-14-1635-2014
- [9] Nicolet, M., "On the molecular scattering in the terrestrial atmosphere: An empirical formula for its calculation in the homosphere," *Planetary and Space Science* **32**, 1467-1468 (1984).
- [10] Mayer, B. and Kylling, A., "Technical note: The libRadtran software package for radiative transfer calculations - description and examples of use," *Atmos. Chem. Phys.* **5**, 1855-1877 (2005). doi:10.5194/acp-5-1855-2005
- [11] Gröbner, J., Wardle, D. I., McElroy, C. T., and Kerr, J. B., "Investigation of the wavelength accuracy of Brewer spectrophotometers," *Appl. Opt.* **37**, 8352–8360 (1998).

A birefringence-based wavelength ruler for on-site wavelength scale calibration of spectroradiometers in the UV

O. El Gawhary*, N. van der Leden, S.A. van den Berg, and D. Voigt

VSL, Dutch Metrology Institute, Delft, the Netherlands (*oelgawhary@vsl.nl)

Abstract

Generally speaking, the wavelength calibration of array spectroradiometers in the UV range of the electromagnetic spectrum requires the availability of a source that can provide a known reference spectrum. Such a spectrum usually consists, in practice, by a collection of narrow-band lines from laser sources or low-pressure discharge lamps. Accurate knowledge of the wavelength of the source allows a direct and simple calibration of the wavelength scale of the device under test. Because the number of reference wavelengths available in the UV is rather limited, surely for portable standards, it is hard to achieve an accurate wavelength scale calibration. In this paper we describe the main principle behind the realization of an artificial wavelength calibration system and its realization.

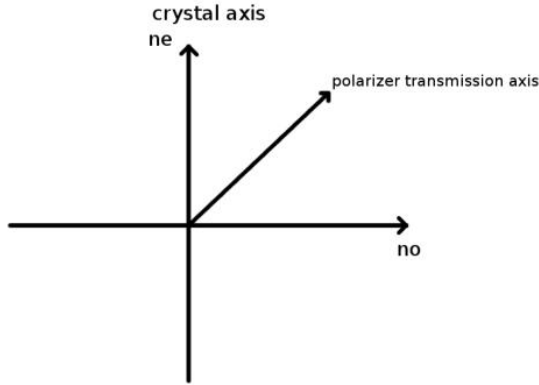


Figure 1. Polarizers and crystal axes orientation. The x -axis coincides with the ordinary axis of the anisotropic crystal while the y -axis coincides with the extraordinary axis. The transmission axes of the two polarizers are either parallel or orthogonal to each other. In either case, the polarizers transmission axes are not parallel with any of the crystal axes.

I. INTRODUCTION

Spectroradiometers, measuring spectral radiance or irradiance, require calibration of their wavelength scale. This is typically accomplished by using wavelength standards, which are either low-pressure discharge lamps filled with pure gas species (He, Ne, Ar) or laser sources. In both cases the lines available can be not equally distributed in the spectral range of interest, they can consist of multiplets or they can be of low intensity. Additionally, not all the wavelength standards can be conveniently used for on-site calibrations. Within the EMRP project “Traceability for atmospheric total column ozone” (ATMOZ), coordinated by PDMO/WRC, VSL has realized a wavelength ruler for wavelength scale calibration in the range 290 – 350 nm. In the following sections we will show how this can be done by

implementing a Lyot filter using a uniaxial birefringent crystal.

II. PHYSICAL PRINCIPLE

The physics of a Lyot filter has been first introduced by Bernard Lyot in 1933 as a way to build narrow-band filters for solar observations [1, 2]. The same system has been successively nicely described by Evans [3]. Most of the applications of such filter have been triggered by the need of observing the emission of $H\alpha$ line of hydrogen coming from the prominences of the limb of the sun while suppressing all the rest of the continuous spectrum. In order to do so, a narrow-band filter, of about 0.4 nm bandwidth, is required, which can be obtained by means of a multi-stage Lyot filter. Additional works on different improvements of the basic concept of a Lyot filter have been in most part presented later in a series of works by Title [4–7]. In more recent works, other aspects, such as designing filters based on nematic liquid crystal cells and motor-controlled ones for side lobes reduction, have been presented [8]. The basic idea of a birefringence filter is quite simple. Let us assume a uniaxial birefringent crystal of thickness d is given. Since the crystal is uniaxial, it will have one optical axis, which coincides with the direction of the extraordinary axis. We will assume that the crystal is cut in such a way that such an axis is parallel to the polished input/output surfaces of the crystal. Such a plate is positioned between two linear polarizers. The orientation of the transmission axis of the first polarizer is set at 45° with respect to the optical axis of the plate. We denote by n_o and n_e the index of refraction for the extraordinary and ordinary axis, respectively. Fig. 1 shows the orientation of the crystal ordinary and extraordinary axes and the polarizer transmission direction. After passing through the crystal, we will have the following output field distribution on the exit plane

$$\mathbf{E}_{\text{after plate}} = \frac{\sqrt{2}}{2} \begin{pmatrix} \exp(ikn_e d) \\ \exp(ikn_o d) \end{pmatrix} = \frac{\sqrt{2}}{2} \exp(ikn_e d) \mathbf{x}_0 + \frac{\sqrt{2}}{2} \exp(ikn_o d) \mathbf{y}_0 \quad (1)$$

where $k = 2\pi/\lambda$, with λ the light wavelength. The field in Eq. 1 is in general, for any wavelength, elliptically-polarized. Let us now assume that the transmission axis of the second polarizer is at an angle θ with respect to the x_0 axis. The Jones matrix of the polarizer can be written as

$$T_{\text{pol}} = \begin{pmatrix} \cos^2 \theta & \sin \theta \cos \theta \\ \sin \theta \cos \theta & \sin^2 \theta \end{pmatrix} \quad (2)$$

If we neglect the effect of propagation between the plate and the second polarizer, we can directly write the expression for the complex field emerging from the second polarizer, which reads

$$\begin{aligned} \mathbf{E}_{final} &= \frac{\sqrt{2}}{2} \begin{pmatrix} \cos^2 \theta & \sin \theta \cos \theta \\ \sin \theta \cos \theta & \sin^2 \theta \end{pmatrix} \begin{pmatrix} \exp(ikn_e d) \\ \exp(ikn_o d) \end{pmatrix} \\ &= \frac{\sqrt{2}}{2} \begin{pmatrix} \cos^2 \theta \exp(ikn_e d) + \sin \theta \cos \theta \exp(ikn_o d) \\ \sin \theta \cos \theta \exp(ikn_e d) + \sin^2 \theta \exp(ikn_o d) \end{pmatrix} \end{aligned} \quad (3)$$

Normally, at optical wavelengths, a detector will only measure the intensity of the light beam. This means that the measured intensity will have the following expression

$$\begin{aligned} I_{final}(\theta) &= \frac{1}{2} [|\cos^2 \theta \exp(ikn_e d) + \sin \theta \cos \theta \exp(ikn_o d)|^2 \\ &\quad + |\sin \theta \cos \theta \exp(ikn_e d) + \cos^2 \theta \exp(ikn_o d)|^2] \end{aligned} \quad (4)$$

If we choose $\theta = \pi/4$ (this means that the transmission axes of the two polarizers are parallel to each other and set at 45° with respect to the extraordinary axis of the crystal), we obtain for Eq. 3

$$I_{final}(\theta = \frac{\pi}{4}) = \frac{1}{2} [1 + \cos(k\Delta n d)] \quad (5)$$

where $\Delta n = n_e - n_o$. If, on the other hand, we rotate the second polarizer by additional $\pi/2$ degrees (this means that the two polarizers are crossed with respect to each other), we get

$$I_{final}(\theta = \frac{3\pi}{4}) = \frac{1}{2} [1 + \sin(k\Delta n d)] \quad (6)$$

By sandwiching more polarizer-plate-polarizer sequences, one can in principle obtain the product of several functions like that in Eq. 5 or 6, which results in much sharper lines. The way the wavelength dependence appears in Eq. 5 and Eq. 6 is through the dispersion of the birefringence $\Delta n(\lambda)$ and $k = 2\pi/\lambda$. When an instrument measures such intensities as a function of the wavelength, an additional wavelength dependence is introduced by the instrument itself. If the device introduces a nonlinear relation $\varphi(\lambda)$ between measured and ideal wavelength, then the actual measured intensity will take the form

$$I_{final}^{(meas)}(\theta = \frac{\pi}{4}) = \frac{1}{2} \left\{ 1 + \cos \left[\frac{2\pi}{\varphi(\lambda)} \Delta n(\varphi(\lambda)) d \right] \right\} \quad (7)$$

or

$$I_{final}^{(meas)}(\theta = \frac{3\pi}{4}) = \frac{1}{2} \left\{ 1 + \sin \left[\frac{2\pi}{\varphi(\lambda)} \Delta n(\varphi(\lambda)) d \right] \right\} \quad (8)$$

depending on the orientation of the second polarizer. When drawn as function of the wavelength λ , the filter response shows many peaks, whose positions depend on the crystal thickness and birefringence. By acquiring a priori knowledge on the system on the actual thickness at the operating temperature and on the birefringence Δn and its dispersion, one can predict the position of the transmission peaks of the filter and use them to characterize the instrument response $\varphi(\lambda)$. As example, Fig. 2 shows the

ideal transmission of a system based on a quartz plate of thickness $d \approx 1.4\text{mm}$, with two linear polarizers, in the parallel configuration. The actual material absorption of both polarizers is taken into account in the plot. The choice of the most suitable plate thickness is a trade-off between having enough lines in the spectral region of interest and a proper SNR for a single spectral line is too low, the wavelength determination is limited by the spectral resolution of the instrument, which can be as large as 0.1 nm. A final remark is that for the model to work, the crystal thickness d has to stay constant. For a thickness of the order of 1 mm, with a thermal expansion coefficient of about $0.33 \cdot 10^{-6}/\text{K}$ (linear thermal expansion coefficient for quartz), a temperature control of the order of 0.1°C will guarantee a thickness stability in the range of tens of picometers.

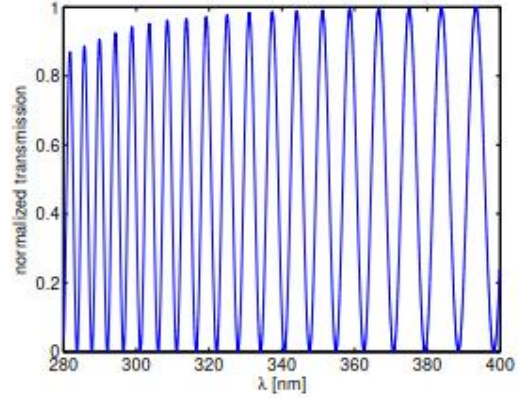


Figure 2. Ideal transmission of a one-stage Lyot filter, in the range 280 – 400 nm.

III. REALIZATION

The optical response is determined by sandwiching two uncoated Glan-Laser alpha-BBO Polarizers, 10.0 mm in diameter clear aperture, with a birefringent element in between. These two polarizers are placed in two rotation mounts in order to allow the proper alignment of the two transmission axes. The birefringent plate will consist of a 1.4 mm (nominal value) quartz plate. All the components are mounted in 30mm cage system and fixed to a 10 × 15 mm² optical breadboard. This will facilitate the use of the wavelength ruler when employed for system calibrations.

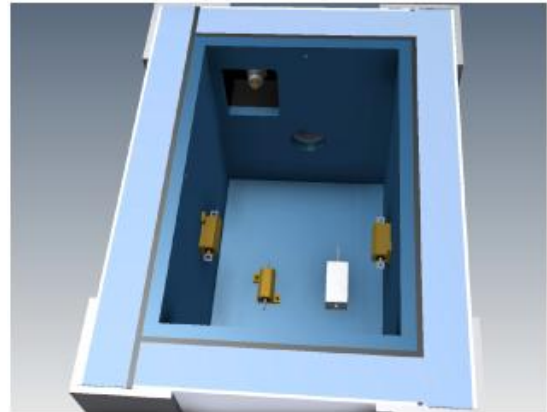


Figure 3. Detail of the isolation plate and temperature control system in the cover cap of the wavelength ruler.

Thematic Network for Ultraviolet Measurements

The system is provided with an isolation cap, to ensure the proper thermal isolation from external conditions. Additionally, the temperature is controlled within 0.1°C by means of a system of resistors and temperature sensors. This prevent thermal expansion of the quartz plate which, in turn, would translate into an instability of the transmission lines. The operating temperature is expected to be not higher than 25°C.

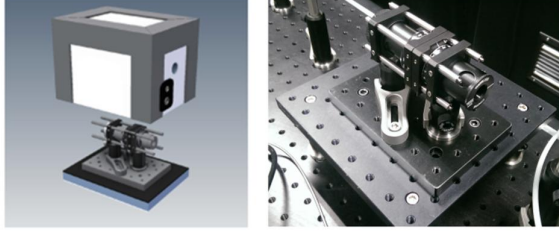


Figure 4. A view of the wavelength ruler in all its main components (left) and a detail on the actual realization for the optical components (right). The optical elements are fixed on a small bread board. The thermal isolation housing is placed as a cap that can be easily removed if necessary. The electronic for the temperature controller is not shown.

IV. MEASUREMENTS

The spectral transmission of the ruler has been first measured at the double-monochromator based permanent facility at VSL, used to perform calibration of transmission of filters. These measurements are combined with an independent measurement of the thickness of the quartz plate, performed by using gauge blocks. The average thickness, along the cross section of the plate, resulted to be $1.39496 \text{ mm} \pm 0.04 \text{ }\mu\text{m}$. Since this thickness has been measured at 20.0°C, a correction of 3.87 nm must be considered, when operating the system at 25°C. The peak wavelengths are determined by using the centroid method and are reported in table I

Table I. Peak wavelengths of the wavelength ruler determined through the centroid method.

# peak	λ [nm]	# peak	λ [nm]
1	291.86	7	321.90
2	296.25	8	327.81
3	300.98	9	334.03
4	305.90	10	340.56
5	310.96	11	347.45
6	316.24		

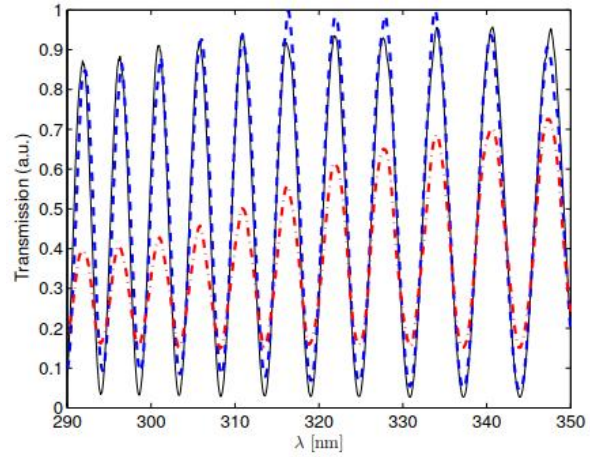


Figure 5. Spectral response wavelength ruler as measured by three different systems. The red curve has been measured by a double-monochromator system available at VSL. The blue and black curves have been measured by two array spectrometers produced by two different manufacturers.

V. SENSITIVITY OF PEAKS POSITION WITH RESPECT TO PHYSICAL DIMENSIONS VARIATION

As we have seen, the thickness d of the plate in the filter influences the transmission of the filter. For convenience, in this section we will call this thickness d_{Lyot} . If we neglect for a moment any material dispersion phenomenon, the normalized transmission can be written as

$$|t|^2 = \frac{1}{2} \cos^2 \left(\frac{k_0 \Delta n d_{Lyot}}{2} \right) \quad (9)$$

The peaks' positions result to be

$$\lambda_{peak}^m = \frac{\Delta n d_{Lyot}}{m} \quad (10)$$

where $m = \pm 1, 2, \dots$ is an integer labelling the m^{th} transmission peak. The sensitivity of the position of the transmission peaks of a Lyot filter with respect to a variation of its thickness d_{Lyot} is given by

$$\frac{\partial \lambda_{peak}^m}{\partial d_{Lyot}} = \frac{\Delta n}{m} \quad (11)$$

It is useful to perform a similar calculation for another type of cavity, this time of multi- beams interference type. Let us consider a Fabry-Perot cavity of thickness d_{FP} . We assume to have a simple Fabry-Perot system made of one single medium. Due to the multiple reflections taking place in the system, the intensity of the total transmitted field can be written as (again after neglecting any material dispersion)

$$|t|^2 = \frac{T^2}{(1 - R)^2 + 4R \sin^2(k_z d_{FP})} \quad (12)$$

where T is the product of the two Fresnel transmission coefficients for the two interfaces of the cavity (supposed

to be made of a medium of index of refraction n immersed in vacuum), and R is the product of the two Fresnel reflection coefficients for the same interfaces. $kz = \sqrt{k_0^2 n^2 - k_x^2}$, which is equal to $k_0 n$ in case of normal incidence ($k_x = 0$). k_x, k_z are the wave vector components of the incoming wave. We can say that the transmission peaks are located at position

$$\lambda_{peak}^m = \frac{2nd_{FP}}{m} \quad (13)$$

Where, again, $m = \pm 1, 2, \dots$ is an integer labelling the m^{th} transmission peak. From Eq. 13 we can easily compute the sensitivity of a peak with respect to a thickness variation, which is simply given by

$$\frac{\partial \lambda_{peak}^m}{\partial d_{FP}} = \frac{2n}{m} \quad (14)$$

Because of the different sensitivity coefficients, if both systems are stabilized with respect to temperature changes, then one is left only with the uncertainty in the thickness of the cavities. We see that a ruler based on a Lyot-filter system is inherently less sensitive to thickness uncertainty than a Fabry-Perot cavity, due to the fact that the birefringence Δn is typically a couple of orders of magnitude smaller than the index of refraction n of dielectrics.

VI. CONCLUSIONS

In this work we have described the design and the realization of a portable wavelength calibration system, to be used to calibrate the wavelength scale of spectroradiometers in the UV. The system is based on a single-stage Lyot filter and is designed for on-site calibration of spectroradiometers working in the range 290 – 350 nm.

Acknowledgement This work has been supported by the European Metrology Research Programme (EMRP) within the joint research project EMRP ENV59 “Traceability for atmospheric total column ozone.” The EMRP is jointly funded by the EMRP participating countries within EURAMET and the European Union.

References

1. B. Lyot, *Comptes Rendus* **197**, 1593 (1933).
2. B. Lyot, *Ann. Astrophys.* **7**, 31 (1944).
3. J. W. Evans, *JOSA*, **39** 229-242 (1949).
4. A.M. Title, *Appl. Opt.* **14**, 445 (1975).
5. A.M. Title, *Solar Phys.* **33**, 521 (1973).
6. A.M. Title, *Appl. Opt.* **14**, 229 (1975).
7. A.M. Title, *Appl. Opt.* **15**, 2871 (1976)
8. G. Yang, Z. Zheng, H. Li, X. Liu, *Appl. Opt.* **49**, 1280-1287 (2010).

Application of stray light corrected array spectroradiometers for UV measurements

Denan Konjhodžić

Instrument Systems GmbH, Munich, Germany

Introduction

The main limitation of the performance of an array spectroradiometer in photometry and colorimetry is the occurrence of stray light in the instrument. This means that a particular element of the array detector registers radiation from a different spectral region than the designated one. The reason for the occurrence of stray light can be found in various mechanisms:

- scattered light from the diffraction grating due to manufacturing inaccuracies in the shape and spacing of the lines, or roughness of the surface of the grating,
- higher diffraction orders, particularly for detectors with a wide spectral range,
- double diffraction of the light reflected back on the grating,
- inter-reflections between the detector and other optical components,
- reflection and scattering from surfaces, especially from the inner wall of the spectrograph,
- fluorescence of optical components,
- and the way how the light is coupled into the spectroradiometer.

Thus, the total amount of the measured radiant power contains a part of incorrect radiation, which causes an error in the spectral power distribution. The main approach to improve the radiometric performance of the spectroradiometer is to avoid, or at least largely suppress, the stray light by design measures of the spectrograph. When further suppression is technically not possible, the residual stray light can be effectively corrected to a great extent by a suitable method of measuring and calibration, for example, by applying the NIST method [1], as outlined in the following.

Creation of the stray light matrix

The calculation of correction functions requires precise knowledge of the stray light behaviour of the spectroradiometer used for measurements over the full detectable spectral range. The complex stray light behaviour of an array-spectroradiometer can, as shown in [1], be determined with the aid of tuneable laser sources. The idea is that monochromatic radiation can be attributed for the most part to a certain pixel of the detector. The entire light that is measured outside the bandpass function for this wavelength is the stray light contribution of pixel i that is seen from all other pixels j in the detector. Most realisations of the stray light correction are based on this method, such as that described in [2].

In our practical realisation, excitation wavelengths are tuned within the measurement range of the spectroradiometer in 10 nm steps with the aid of OPO laser excitation, and one spectrum is recorded for each step. An optical parametric oscillator (OPO) is a driven harmonic oscillator that oscillates at optical frequencies. It converts an input laser wave into two output waves of lower frequency by means of second-order nonlinear optical interaction. The set of all recorded spectra over all excitation wavelengths appropriately interpolated results in a device-specific LSF matrix. If the band-pass function of the real signal is subtracted, one obtains a stray light distribution function (SDF) matrix. The inverse of the SDF matrix can be multiplied with raw spectra in order to obtain stray light corrected spectra.

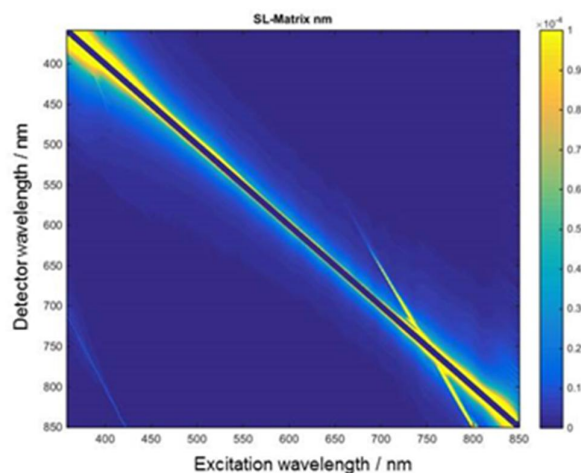


Figure 1. Typical stray light matrix using the example of a CAS 140CT (Model VIS).

Our realisation of the stray light correction method is the first commercially available, convenient method for any user. The stray light matrix determined for a certain spectroradiometer can already be numerically applied during the calibration of the spectroradiometer with any accessory. For the subsequent stray light corrected measurements, one has to choose the appropriate calibration and the stray light matrix is applied automatically to any measured spectra, without additional time and effort. Depending on the application, lamp type, and the spectral range observed, a stray light correction of array spectroradiometers provides lesser or greater advantages.

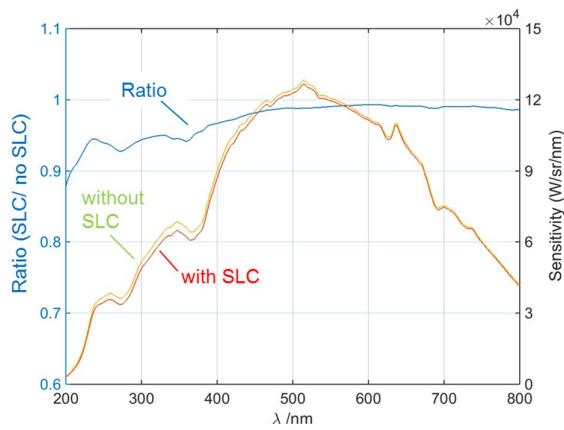


Figure 2. Relationship of sensitivity curves with and without stray light correction.

Advantage of the stray light correction for spectral calibrations

Broadband sources such as halogen lamps and deuterium lamps are normally used for the spectral calibration of spectroradiometers. The impact of stray light correction on the spectrum of a broadband source is particularly distinct in the UV but also in IR spectral range, because the detector of an array spectroradiometer has very low sensitivity at the edges. Stray light correction of the spectrum used for calibration is particularly meaningful, as in particular, errors in the areas of lower sensitivity are intensified due to the division of the measured spectrum by the reference spectrum.

If we compare the relationship of the sensitivities with and without stray light correction after calibration, we can recognize a stray light portion of up to 10% in the UV range (Figure 2). Stray light free sensitivity in this range of the already low sensitivity, has a direct effect on the absolute precision. In particular applications based on UV radiometry thus profit from stray light correction, e.g. measurements of UV LEDs, sun simulators or halogen lamps with a high portion of UV radiation.

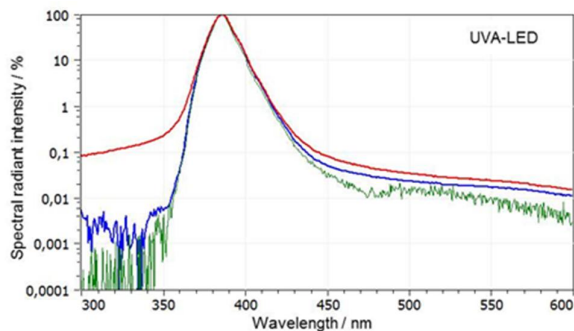


Figure 3. Logarithmic display of the spectra of a UVA LED without (red) and with stray light correction (blue) and measured with a double monochromator (green).

Stray light correction in the UV range

The ultraviolet range is normally subdivided into UVA (320-400 nm), UVB (280-320 nm), and UVC (200-280 nm) regions. UVA radiation is used, e.g. for curing of printing inks, adhesives and coatings. UVC radiation is used, e.g. for disinfection and water purification.

Figure 3 shows by way of example the spectra of a UVA LED with and without stray light correction in logarithmic presentation. The suppression of stray light in the spectral course by somewhat more than one order of magnitude in the UV range to almost 10^{-5} is clearly recognizable. Beyond this, we measure about 3% more precise radiant intensity in this example with the use of stray light correction. The impact of stray light correction is somewhat greater for UVC LEDs. It almost reaches the stray light level of a double monochromator and about 4% more precise radiant intensity (Figure 4). While the peak wavelength (257 nm) does not change at all with the stray light correction, the centroid wavelength shifts by about 0.8 nm in the direction of the peak wavelength.

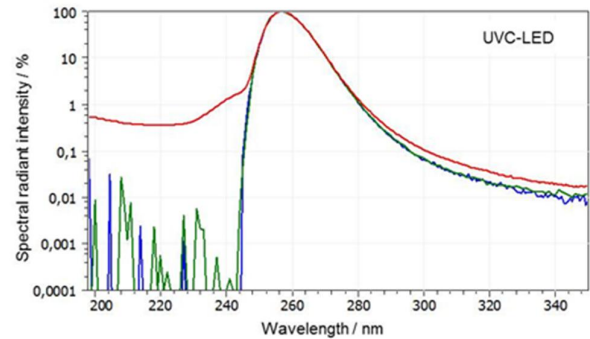


Figure 4. Logarithmic display of the spectra of a UVC LED without (red) and with stray light correction (blue) and measured with a double monochromator (green).

In the measurement of UV LEDs, considerable errors are made in the determination of the absolute value alone by reason of stray light contaminated calibration. As a direct consequence, stray light correction thus has a higher precision in radiometric evaluation. All applications based on UV LEDs profit from this, e.g. curing of adhesives and coatings, lithography, scanning heads, horticulture lighting, biomedical devices, and combatting of hospital infections.

Influence of stray light correction on colour LED measurements

Figure 5 shows an example of the spectra of white, blue, green and red LED standards, in each case with and without stray light correction. The LED standards refer to stabilized and temperature-controlled LEDs. These were measured in a luminous intensity measuring adapter in the I-LED-B configuration with an array-spectroradiometer CAS140 CT (UV-VIS-NIR) with and without application of the stray light correction matrix.

The logarithmic presentation of the spectra clearly shows the impact of stray light correction in the marginal zone and the signal around zero. In ranges with a generally low signal, particularly in the blue and UV range, the stray light level is corrected up to one order of magnitude and reaches a level of 10^{-4} down to $5 \cdot 10^{-5}$.

The impact of stray light correction on the x, y colour coordinates with up to 0.0005 is not to be neglected, if we bear in mind that high-quality array spectral radiometers exhibit measurement uncertainties of ± 0.002 to ± 0.0015 and the LED industry strives for an ambitious tolerance of

± 0.001 . Any increase in measurement accuracy is thus very welcome.

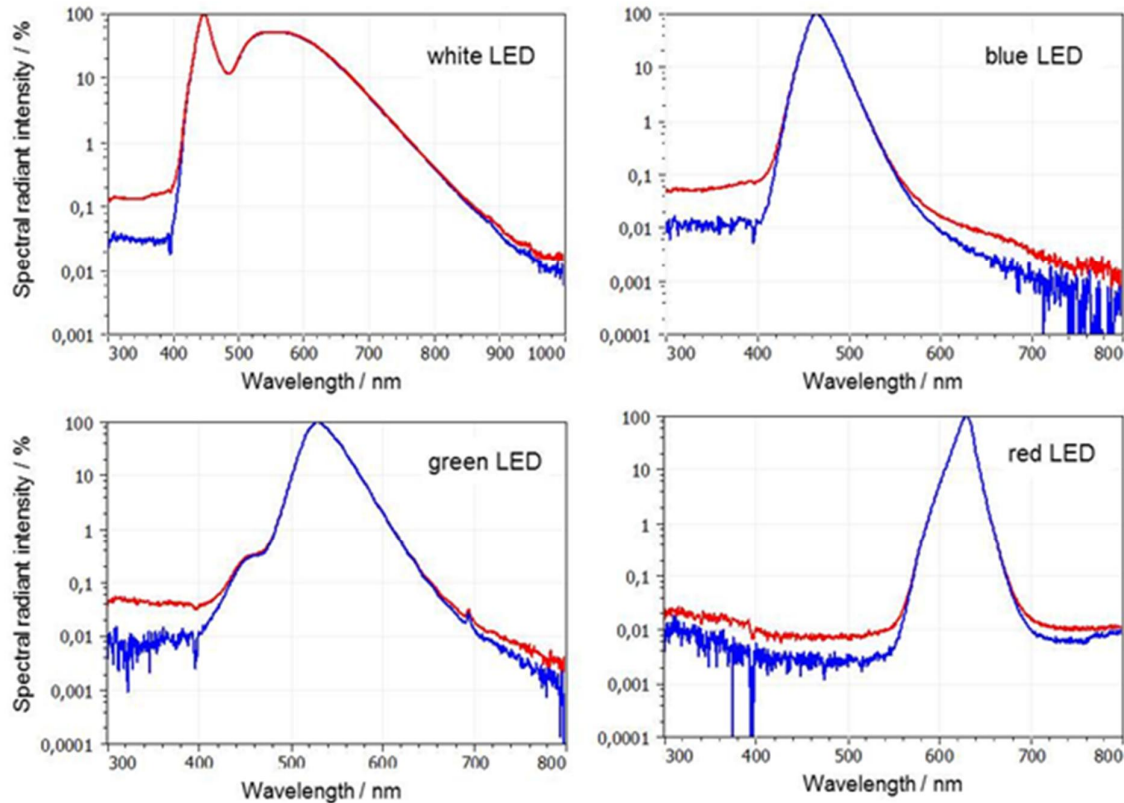


Figure 5. Logarithmic display of the spectra of white, blue, green and red LED without (red) and with stray light correction (blue).

Outlook: Photobiological safety

One application that could particularly benefit from stray light correction is the evaluation of the photobiological hazards of optical radiation, in particular the blue light hazard on the human eye. The blue light hazard is defined as the potential risk of photochemical damage to the retina, caused by radiation in the wavelength range 300-700 nm, with the greatest effect in the range between 400 and 500 nm. So far, the standard EN 62471 recommends complex and expensive double monochromators as measuring instruments, in particular due to the extremely low stray light level. The higher stray light level in the area of greatest impact, in the blue and UV regions, can simulate a non-existent hazard. With the correction of the stray light,

a greater measurement accuracy and measurement dynamics can be achieved in this range. Due to the stray light correction, the array spectroradiometer could become a more convenient and lower-cost alternative to the monochromator for determining the blue light hazard.

References

- [1] Y. Zong, S.W. Brown, B.C. Johnson, K.R. Lykke, and Y. Ohno, "Simple spectral stray light correction method for array spectroradiometers," *Appl. Opt.* **45**, 1111-1119 (2006).
- [2] S. Nevas, J. Gröbner, and L. Egli, "Stray light correction of array spectroradiometer data for solar UV measurements," *UVNews* **9**, 17-19 (2013).

News

UV Index and UV-B solar recorded measurements at Valladolid University, Spain

Julia Bilbao and Argimiro de Miguel

Atmosphere and Energy Laboratory, University of Valladolid, Faculty of Sciences, Spain

Different meteorological and solar variables are being monitored and recorded in outdoor conditions by the Atmosphere and Energy Laboratory, through the research Project "Ultraviolet solar radiation, measurements, models and series reconstruction," (CGL2011-25363), funded by the Spanish Ministry of Economy and Competitivity. The measurement station is located at the Science Faculty of Valladolid University, Spain, whose geographical coordinates are (41°39'48" N; 4°42'20" W; and 705 m asl).

The UV Index is evaluated every 5 min from the erythemal UV-B irradiance and total ozone column measurements. Values of air temperature, solar broadband global and ultraviolet-B horizontal irradiances, and UV-index are shown graphically online, in real time, at

<https://www5.uva.es/laten/index.php/es/radiacion-uv-y-uvi>

Further information: juliab@fa1.uva.es
<http://www5.uva.es/laten/>



The LED-J1019 Transfer standard

Josef Schreder

CMS - Ing. Dr. Schreder GmbH, Kirchbichl, Austria

Since LEDs of a wide range of colors and high intensities have become available (Fig. 1), the applications have expanded enormously, from color displays to street lighting. For better specification of LED characteristics, calibrated standards are required by the industry. Since LEDs are much more complex than conventional lamps in terms of physical properties, large measurement uncertainties have been reported and the development of a suitable standard is a nontrivial task.



Figure 1. LEDs are available as broadband white, or monochromatic from UV to Red.

The LED-1019 transfer standard, a newly developed device for photometric and colorimetric units such as luminous flux [lm], luminous intensity [cd] and dominant wavelength, based on the design by the Physikalisch-Technische Bundesanstalt (PTB), Germany provides a defined measurement geometry for reliable calibration measurements.

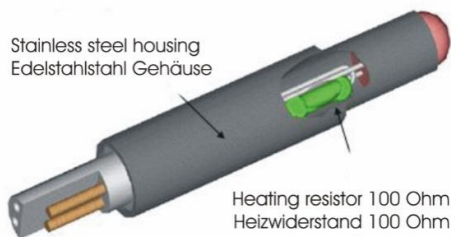


Figure 2. Mechanical construction of J1019 showing its metal housing and the heating resistor.

The LED transfer standard is enclosed in a stainless steel housing with an integrated heating resistor for temperature control as can be seen in Fig. 2. It is available with various different types of LEDs. A LED adaptor is designed to allow a robust and reliable handling of the LED transfer standard. High quality connectors assure a reliable connection of the LED standard to the power supply.

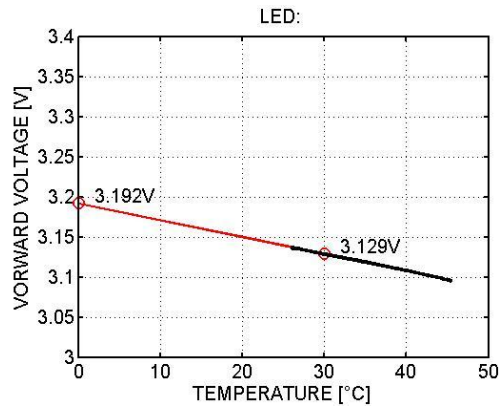


Figure 3. Forward voltage of an LED as a function of its junction temperature.

The standard requires an accurate power supply J1019-POWER which stabilizes an adjustable LED forward current and controls the temperature of the LED chip using the temperature depending LED junction voltage as a sensor (Fig. 3).

References

1. PTB Mitteilungen Heft 4, *Photometrie von Lumineszenzdioden* (2003).
2. T. Gerloff, PTB Mitteilungen 125 Heft 4, *Metrologie für moderne Lichtquellen: LEDs und OLEDs* (2015).

